# Proximity in Hybrid Superconductor/ Ferromagnetic Structures

by

Makram Abd El Qader

A Dissertation Presented in Partial Fulfillment
of the Requirements for the Degree
Doctor of Philosophy

Approved November 2016 by the
Graduate Supervisory Committee:

Nathan Newman, Chair
John Rowell
Nick Rizzo
Hongbin Yu

ARIZONA STATE UNIVERSITY

December 2016

ABSTRACT

The coexistence of superconductivity and ferromagnetic orders has been the subject of study for many years. It well known that these materials possess two competing order parameters; however the two order parameters can coexist under special circumstances inducing interesting physical phenomena. In recent years the demand of ultra-low-power, high density cryogenic memories has brought considerable interest to integrate superconducting and magnetic thin films in one structure to produce novel memory elements. The operation of the device depends on the unusual electronic properties associated with the Superconductor (S) /Ferromagnetic (F) proximity effect.

Niobium (Nb) based Josephson junction devices were fabricated with barriers containing two ferromagnetic layers separated by a normal metal space layer. In device operation, electrons in the superconductor are injected into the ferromagnets, causing the superconductor wavefunction to shift its phase and decay in amplitude. Such devices have two different states that depend on the relative magnetization of their ferromagnetic barrier layers, parallel or antiparallel. In these different states, the junctions have different phase shifts and critical currents. Superconducting circuits containing these devices can be designed to operate as memory cells using either one of these outputs.

To quantify the shift in phase and amplitude decay of the wavefunction through a common ferromagnet, permalloy, a series of Nb/permalloy/Nb Josephson junctions with varying ferromagnetic layer thicknesses were fabricated. Data have shown that the optimal thickness of a fixed layer composed of permalloy is 2.4 nm, as it shifts the wavefunction phase to $\pi/2$, its “pivot point.” If set to precisely this value, the free layer in SFNF'S junctions will switch the junction into either the 0 or $\pi$ state depending on its

magnetic orientation. To minimize the free-layer switching energy dilute Cu-permalloy alloy [$Cu_{0.7}(Ni_{80}Fe_{20})_{0.3}$] with a low magnetic saturation ($M_s$ of ~80 emu/cm$^3$) was used as the free layer. These devices exhibit switching energies at small magnetic fields, demonstrating their potential use for low power non-volatile memory for superconductor circuits.

Lastly, to study the proximity effect using other potentially-useful ferromagnetic layers, measurements were performed on Nb/F bilayers and Nb/F/$AlO_x$/Al tunnel junctions with ferromagnets $Ni_8Fe_{19}$, $Ni_{65}Fe_{15}Co_{20}$, and $Pd_{1-x}Ni_x$. The dependence of the critical temperature of the bilayers and density of states that propagated through the ferromagnetic layer were studied as a function of thickness. From this study, crucial magnetic and electrical parameters like magnetic coherence lengths ($\xi_F$), exchange energy ($E_{ex}$), and the rate of shift in the wavefunction's phase and amplitude as a function of thickness were determined.

DEDICATION

To my parents

ACKNOWLEDGMENTS

First and foremost, I would like to express my deepest gratitude and thanks toward my advisor, Professor Nathan Newman, for his precious leadership, guidance, numerous encouragements and generous support throughout my years at ASU. His presence and state of the art facilities made this work possible, and made me the man who I am today .Special thanks to Professor John Rowell, for his marvelous guidance and valuable support. The days that I spent with them helped me shape my future direction as a great experimentalist in the area of superconductivity. I would like to thank the other committee members, including Dr. Nick Rizzo first for his tremendous support and encouraging being positive at dark times in my journey, and second for his valuable teaching in the area of magnetism and device physics. , and I am thankful to Prof. Hongbin Yu for his support, and scientific contributions to my thesis discussion. I appreciate all their effort for their detailed suggestions and corrections to my dissertation.

I am deeply indebted to all my colleagues in my research group at Arizona State University for their assistance. Professor Rakesh Singh shared his knowledge about vacuum technology and material characterization techniques like RBS. Dr. Lei Yu spent numerous hours of valuable time collaborating on some of my thesis work. Mr. Richard Hanley and Mr. Thomas Chamberlin assisted me to solve numerous facility problems in the lab. I would like also to thank Dr. Mengchu Huang and the late Dr. Brett Strawbridge who gave me extensive advice on device fabrication and systems maintenance to the late nights of my work. I need to thank Mr. Cougar Garcia and Mr. Cameron Kopas for RBS, XRD characterizations and valuable input on my research thesis. I want to thank all the other members of the group for the enlightening discussion and vigorous support. These

members include: Dr. Lingtao Liu, Dr. Mahmoud Vahidi, Mr Aditya Ravi, Miss Sarah Galvin and Mr. Rahul Mitra.

I wish to give my gratitude to all the faculties and staff at the LeRoy Eyring Center for Solid State Science, for informative discussions about research facilities and characterization techniques. I want to thank Professor Ray Carpenter and Dr. John Mardinly for TEM characterization, Dr. Barry Wilkins for RBS measurements, Mr. David Wright for cryogenic temperature measurements, Mr. Kenneth Mossman for AFM measurements, Dr. Emmanuel for his XRD help and Diane for her help in AFM and ellipsometery work. I also wish to thank the faculties and staff at the School of Engineering, for intellectual discussions and selfless help, as well as the staff at Center for Solid State Electronics Research. I would like also thank Professor Van Schilfgaarde. Finally I would like to thank Ms. Stan Goldfarb for his support, and time in the discussion that took place over the phone, emails, and cup of coffee in the area of vacuum technology and thin film growth.

My Ph.D. studies was not an easy journey in any means, that why I will never forget the spiritual and material support from my family. My parents, my mother Samera and father Saleh Abd El Qader, I am grateful to you for everything I have achieved here. Special thanks to my wife to be, Miss Hiba Jbarah, for all the joy she brings to my life. Special thanks to the Sheik Yousef family , Aroura , Adnan, Diana ,Nadia for their continuous support and hospitality .Last but not least, I wish to thank all my close friends, for your support and inspiration, including Charbel and Charles Azzi, Jonathan Burgos, Midhat Qader, Noor Massarweh, and Hikamt Haj Yehia. Finally many thanks for all my beloved family in my town of Taybee.

TABLE OF CONTENTS

Page

CHAPTER Page

CHAPTER Page

LIST OF TABLES

Table Page

LIST OF FIGURES

Figure Page

Figure Page

Figure Page

Figure Page



Figure Page

Figure Page

# CHAPTER 1 MOTIVATION AND INTRODUCTION

## 1.1 Overview

Cooper pair tunneling in superconductor/insulator/superconductor structures (SIS) was first predicted by Brian D. Josephson [1] in 1962. It was subsequently observed by John M. Rowell and Phillip Anderson [2] in 1963. Since then junctions with wide range of geometries and materials were fabricated and used into different application. The most successful and widely used of Josephson junctions is the Nb/Al/$AlO_x$/Nb tunnel junctions, developed by Rowell and his collagenous in the 1980s [3, 4]. One of the most prominent uses is in rapid single flux quantum (RSFQ) [5] logic which is best known for its ultra-high-speed operation. Strong interest has arisen to use this technology in information processors. Individual Josephson junction devices have switched at speeds up to 770 GHz [5] and large circuits have demonstrated above 100 GHz operation [5].

To achieve the full potential of Nb-based logic circuits for direct signal digitization for software-defined radio [6, 7] and router applications [8] will require the realization of a fast, ultra-low power memory technology. The demands for memory are markedly greater if a high-end computer is considered. In the recent Superconducting Technology Assessment (STA) performed by the NSA [9], the lack of a superconducting memory technology was identified as the most critical problem for the high-end computing application. Satisfying this need is the goal of the proposed project. There have been many potential solutions for achieving the needed performance of memories for a superconductor supercomputer, although all of these approaches have fallen short of the density, speed and/or energy requirements. Some of the devices are based on

manipulating magnetic flux quanta [10, 11], but they cannot achieve high density as a result of the large size of the obligatory inductive loop. A hybrid solution has been developed with a combination of CMOS technology logic and Josephson junction state detection; however this memory consumes large amounts of power [12] The STA report also considers magnetoresistive random access memory (MRAM). This approach is appealing given that MRAM is non-volatile, the device speed is comparable to DRAM, and the potential density is greater than SRAM.

Recently new type of superconducting memory based on Superconductor-Ferromagnetic-Superconductor (SFS) Josephson junctions was proposed [13]. The physics of the device combines the spin magnetization used in conventional MRAM cells with Josephson tunneling. The Josephson implementation has all of the advantages typically argued for the conventional MRAM: high speed, non-volatility with high write-erase endurance, and high storage density [14, 15, and 16].

In fact, the Josephson MRAM (JMRAM) operation is similar to conventional MRAM. High and low Josephson critical currents can correspond to the logical states of the cell. JMRAM has superconducting wiring that allows non-dissipative propagation of the signals with speed-of-light access time even in large memory arrays [17].

The first goal of this thesis is to explore and study the magnetic materials to be used in such proposed devise. We have characterized the structural, electrical and magnetic properties of $(Cu_{1-x}(Ni_{80}Fe_{20})_x)$ alloys films. This study intended to help us understand and optimize the magnetic properties needed to achieve the low energy switching for our device. Our second goal was to fabricate Josephson junctions with ferromagnetic barrier materials SFNF'S as memory cells [where S-superconductor-ferromagnet, and N-normal metal] and

characterize them electrically and magnetically and test their functionality for practical cryogenic memory applications. Lastly, we determined the important parameters that characterize the proximity effect in S-F structures for several different ferromagnets. In these S/F bilayers, we determined the critical temperature ($T_c$) as a function of ferromagnetic thickness. In S/F/I/N tunnel junctions, we measured the density of states (DOS) that propagated through the ferromagnet as a function of ferromagnetic thickness. From this study, we were able to infer crucial magnetic and electrical parameters like magnetic coherence lengths ($\xi_F$), exchange energy ($E_{ex}$), and the rate of shift in the wavefunction's phase and amplitude as a function of thickness.

As the introduction of this thesis, some basic concepts, i.e .Superconductivity, ferrimagnetism, Josephson junctions, S/F/S junction theory, and superconducting cryogenic memory are reviewed. At the end of this chapter, the research plan that we followed is presented.

## 1.2 Fundamentals of superconductivity

This section is intended to give an overview of the microscopic picture of superconductivity and to justify the description of superconductivity as macroscopic quantum state, used in the later sections. Chapters from Vanduzer [18] are summarized.

Superconductivity was discovered by H. Kamerlingh Onnes [19] in 1911.He found that in some materials resistance dropped to zero when it is cooled through some critical temperature $T_c$. So far, various types of materials, such as elements, alloys, ceramic materials, and organic compounds, have been found to have superconductivity. So far the critical temperature $T_c$ value where materials super conduct ranges between 0.01 K to

134 K. In 1933, the German physicists Walther Meissner and Robert Ochsenfeld [20] found that magnetic field is expelled from superconducting material during its transition into the superconductive state, as shown in Figure 1. Also this implies that superconductivity can be destroyed when the external magnetic field exceeds a critical value, $H_c$, which depends on temperature.

$$H_c(T) = H_c(0)[1 - (T/T_c)^2] \qquad (1.1)$$

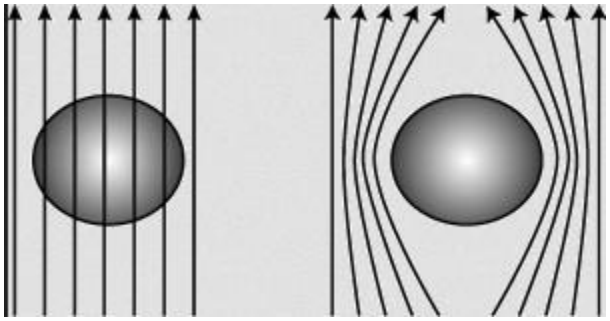

Figure 1. Cartoon of the Meissner effect.where arrows represent the applied magnetic field .and lines are excluded from a superconductor when it is below its critical temperature [21]

Conventional superconductivity is found to be based on an attractive, phonon assisted electron-electron interaction, first described by Bardeen and Frohlich in 1950. its relevance was shown to be true in the early stage of the formulation of this new attractive interaction was the influence of the atom mass in isotopes of superconductors on the critical transition temperature, $T_c$. This can be described in this simple form; an electron polarizes the atom lattice due to its negative charge which can influence the energy of a second electron nearby. Cooper showed in 1956 that through a phonon assisted or mediated process, these two electrons can lower the total energy of the system and condense in a lower energy level, called the ground state. The two electrons form a 'Cooper-pair" and have opposite spin and opposite k-vectors, as shown in Figure 2.

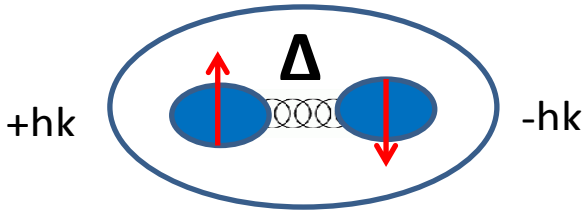


Figure 2. Cooper pair with antiparallel spins alignment and zero net momentum

In a landmark paper [22a], Bardeen, Cooper and Schrieffer (BCS) defined a BCS ground state with a single macroscopic wave function

$$\psi = n_s e^{i\phi} \qquad (1.2)$$

where, $n_s$ is the number of pairs (amplitude) and $\phi$ is the (phase) .The gain in energy resulting from the pairing of electrons is given by $-N(E_F)\Delta^2/2$, where $N(E_F)$ is the density of states (DOS) at the Fermi energy.

As discussed in [22a and 22b] While Cooper pairs are present in the ground state, their excitation is the breaking of a Cooper-pair which results in two independent quasiparticles being present in the excited state. The lowest possible energy of an unpaired electron in SC (also called quasiparticle) is given by the supercondcutor energy gap $\Delta$. This results in an energy gap of size $\pm\Delta$ around the fermi level $E_F$ in the DOS of the quasiparticles Figure 3. The introduction of this gap can be used to explain the zero resistance of superconductors below Tc. The quasi particles are Fermions and follow Fermi statistics. The energy gap $\Delta$ is 1.4 mV for Nb and decreases with increasing temperature, with the energy gap $\Delta$ going to 0 at $T_c$ [22b].

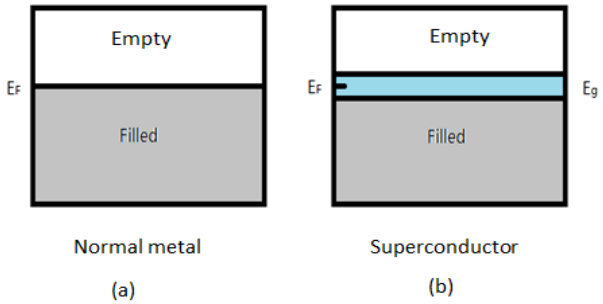


Figure 3. Conduction band in the normal state; (b), Energy gap at the fermi level in the BCS SC ground state [23]

1.3 Fundamentals of ferromagnetism

Some transition metals including iron, nickel, and cobalt are ferromagnetic at room temperature. Some rare earth metals such as gadolinium and other transition metal alloys such as PdNi alloys are ferromagnetic below room temperature. In a magnetized ferromagnetic crystal, the spins in the majority channel are larger in density that the minority channels. This results in a net local moment in the direction of the field [24].

A quantum mechanical electrostatic interaction called exchange is the mechanism by which the unpaired spins in a ferromagnetic material align. In a simple model's band diagram of a ferromagnetic shown in Figure 4**,** the exchange energy $E_{ex}$ is the energy difference between the parallel and antiparallel bands. The dependence of magnetization on temperature can be explained, as displayed in Figure 5. The magnetization $M_s$ at 0 K is the saturation value. If the temperature increases, the thermal energy decreases the population difference between the spin states and thus the magnetization. At the Curie temperature $T_{Curie}$ and higher, the ferromagnetic state is not observed and a paramagnetic state is observed [25].

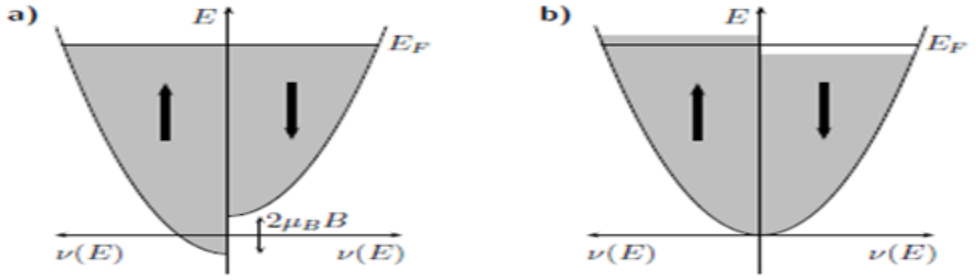


Figure 4. a) Spin split bands for a free electron gas in a magnetic field B. b) Spontaneous splitting of the energy bands in a metal [24]

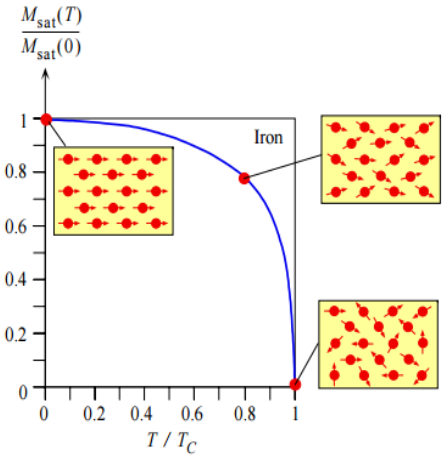


Figure 5. Magnetization temperature dependence of a FM material [24]

Ferromagnetic materials are typically characterized by measuring the hysteretic magnetization that is found as the applied magnetic field is swept in one direction and then the opposite. This is often referred to as the B-H loop. An example hysteresis loop is shown below Figure 6.

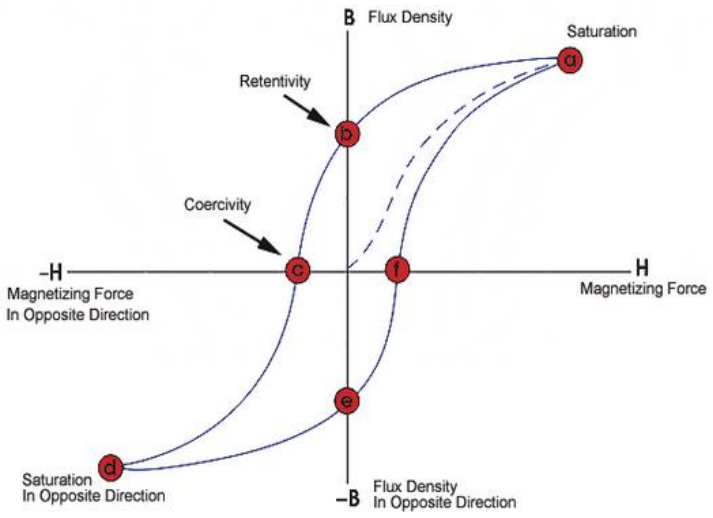


Figure 6. Hysteresis B-H loop of some ferromagnetic material [26]

From the hysteresis loop, a number of primary magnetic properties of a material can be found.

- Retentivity ($M_r$): A measure of the remaining magnetization at zero applied fields corresponding to the saturation induction of a ferromagnetic material. It is a material's capacity to hold a certain amount of residual magnetic field when the applied field force is removed after reaching saturation. (The value of B at point b on the hysteresis curve.) [26]
- Saturation ($M_s$): A measure of the maximum magnetization value that can be reached at a large applied field. (The value of d on the hysteresis curve) [26]

- Coercive Force ($H_c$): The amount of reverse magnetic field which must be applied to a ferromagnetic material to make the magnetic flux return to zero. (The value of $\mathbf{H_c}$ at point c on the hysteresis curve.)[26]
- Squarness ($M_r/M_s$): it's the measure of the B-H loops squareness, it is a reflection of the inhomogeneity of the magnetic material and the corresponding mobility of the domain walls.

  Further information about the measurement and apparatus setup will be discussed in future chapters.

## 1.4 Theoretical overview of proximity effect

### 1.4.1 Superconductor (S)/normal metal (N) (S/N)

When a superconductor (S) is placed in electrical contact with a non-superconducting, the properties of both the metals are modified. The appearance of superconducting correlations in the N metal is called the *proximity effect.*

A superconductor can induce superconducting properties into a normal metal coupled to it due to the proximity effect. At an N-S interface, some electron pairs diffuse into the normal metal while some quasi-particles diffuse into the superconductor, consequently reducing the critical transition temperature of the superconductor material [27].

Transport of electrons with energies less than superconducting energy gap across the interface in such structures is from Andreev reflection [28]. In this process, an incident electron (hole) forms a Cooper pair in the superconductor with the retroflection of a hole (electron) of opposite spin and momentum to incident electron (hole). Since the

pair consists of two electrons with opposite spin, a second electron (hole) forms the pair in superconductor. Both the density of states and the effective electron-electron interaction vary spatially in this S-N structure [29].

The wavefunctions of the two electrons in N-side remain in phase with each other for times on the order of the coherence time, $\hbar/\epsilon$. This translates into the length $\hbar\, v_f/\epsilon$ in the clean limit or $\sqrt{\hbar D/\epsilon}$ in the dirty limit, where $v_f$ is the Fermi velocity, $\epsilon$ is the initial electron with energy (measured with respect to the Fermi energy) and $D$ is the diffusion constant. Based on the theory above, de Gennes [29] found that the metal coherence length, dimension of Cooper pairs, is

$$\xi_{N,S} = \left(\frac{\hbar D_{N,S}}{2\pi k_B T}\right)^{1/2} \tag{1.3}$$

where $D_{N,S} = \frac{1}{3} v_{F_{N,S}} l_{N,S}$ is the diffusion coefficient with the Fermi velocity $\upsilon_F$ and the electron mean free path $l_{N,S}$. In this theory, it is assumed that $l_{N,S} \ll \xi_{N,S}$ (dirty limit) and that the films are relatively thick. In the clean limit $l_{N,S} \gg \xi_{N,S}$ the coherence length is

$$\xi_N = \frac{\hbar\, V_f}{2\,\pi\, K_B\, T} \tag{1.4}$$

The order parameter near the N-S interface is shown in Figure 7.

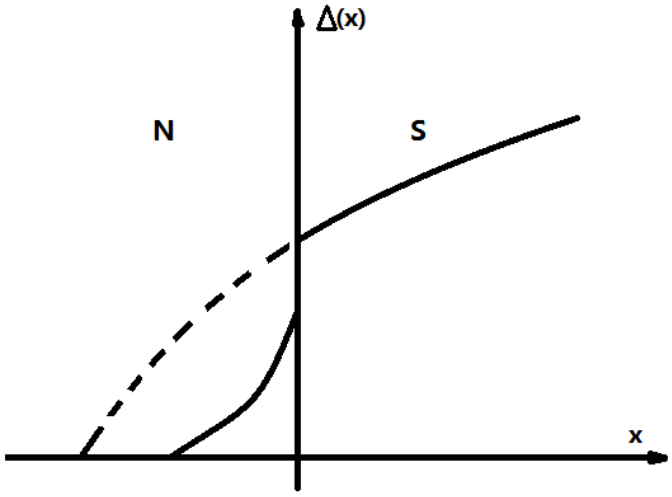


Figure 7. Superconductor order parameter at the N-S interface [30]

1.4.2 Superconductor (S)/ferromagnetic (F) (S/F)

In the previous section we described the proximity effect in N/S system, and now we will describe F/S system. The main difference between the proximity effect in F/S and N/S systems can be shown using the basic model of a ferromagnet shown in Figure 8.

When the two electrons of a cooper pair enter the ferromagnet, they must enter opposite spin bands. The electron with spin parallel to the exchange field will decrease its potential energy, and the electron with spin anti-parallel to the exchange field will increase its energy by the same amount. The total energy conservation from this shift requires:

$$\left|\frac{\hbar^2 k^2}{2m} - \frac{\hbar^2 k^2}{2m}\right| = 2E_{ex} \qquad (1.5)$$

As a consequence of this shift the total momentum of the Cooper pair is not zero anymore but is given as$Q = k_F{}^{\uparrow} - k_F{}^{\downarrow} = 2E_{ex}/v_F$.[31] As a result, the order parameter will gain an additional term proportional to $e^{iQX/\hbar}$. Now, if one considers that the

diffused cooper pairs into F bands are incident with an arbitrary angle θ at the interface, then the net momentum gain of those incident pairs will be $2Q/\cos\theta$ .[31]. If we average over all possible incident angles leads to an oscillation and an algebraic decay of the order parameter, given by $(\sin\frac{x}{\xi_F{}^*})/(\frac{x}{\xi_F{}^*})$ , where $\xi_F{}^* = \hbar v_F/2E_{ex}$. In the case of the dirty limit, where strong scattering mechanism are present (i.e. impurities), the superconducting order parameter will oscillate and decay exponentially as $\sin(\frac{x}{\xi_F{}^*})\exp(\frac{-x}{\xi_F{}^*})$ , where $\xi_F{}^* = \sqrt{\hbar D/E_{ex}}$ .[31] Therefore, in the case of S/F proximity systems, the superconducting order parameter is characterized by a decay and oscillation. In such proximity, the characteristic decay length is called the superconducting coherence length in the ferromagnetic layer and is designated by $\xi_F$ and $\xi_F{}^*$ in the clean and dirty limit respectively [31]. For weak ferromagnetic systems (i.e. PdNi, CuNi, PdFe) [34], this coherence length is reported to be few nm. However in the case of strong ferromagnetic systems (i.e. Ni, Co, Fe) [32], the coherence length is to be around 1 nm or less) because of the larger exchange energy [33]. In S/F systems, the coherence lengths are almost always much shorter than S/N structures. Also, in contrast to the characteristics of S/N structures in S/F structurers, the induced pair amplitude oscillates and the phase shifts with depth in the ferromagnetic metal as shown in Figure 9. Oscillations in the critical temperature, critical current, and density of states were observed experimentally and reported in many papers [34, 35,36,37,38, and 39].

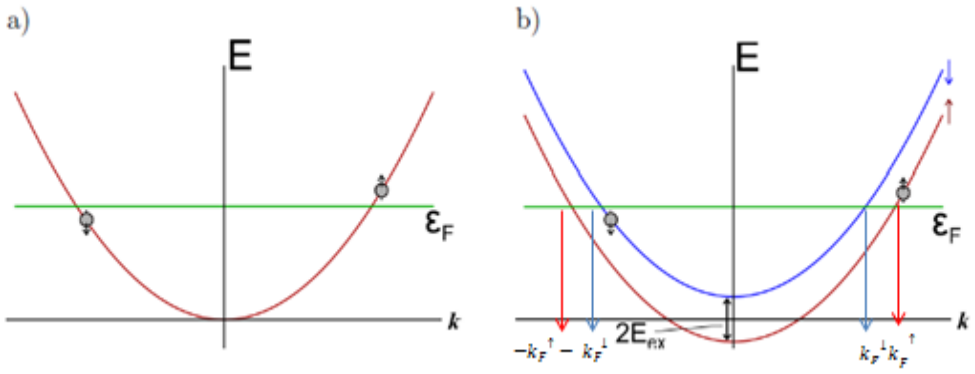


Figure 8. ID free-electron dispersion relation in a normal metal, showing two electrons that have "diffused" into N from S (In the Andreev reflection frame, the electron below the fermi surface would be shown as a hole), (b) In a ferromagnet case there is a shift between the fermi wave vectors of the two electrons due to the exchange energy of the ferromagent [33]

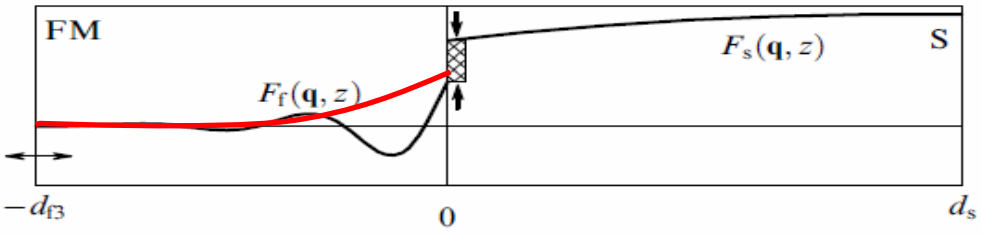


Figure 9. Pair amplitude propagating from S into F – F/S proximity effect

## 1.5 Josephson junctions

### 1.5.1 Overview

In 1962, Brian Josephson made the prediction that a supercurrent can flow through a junction fabricated by two superconducting electrodes separated by a thin insulating tunnel barrier. The supercurrent is given by

$$I_S = I_C \sin(\Delta\theta) \tag{1.6}$$

Where $\Delta\theta$ is the difference in the phase of the superconducting order parameter of both electrodes across the barrier and the critical current $I_c$ is the maximum current that the junction can provide [1].

Josephson prediction was later observed by the experiment of Anderson and Rowell [2]; hence the phenomena described above came to be known as the *Josephson Effect.*

The fundamentals of the Josephson effect can be viewed as following: when two SC electrodes with each its own macroscopic wavefunctions are separated by a thin insulating barrier, the wavefunction can extend though the barrier, as shown in Figure 10. Note that n1(x) and n2(x) are the copper pair density of the two superconducting electrodes, and L is the thickness of the insulating barrier. In such case, the SC order parameter is not constant and a "decaying" exponential is expected in the barrier.

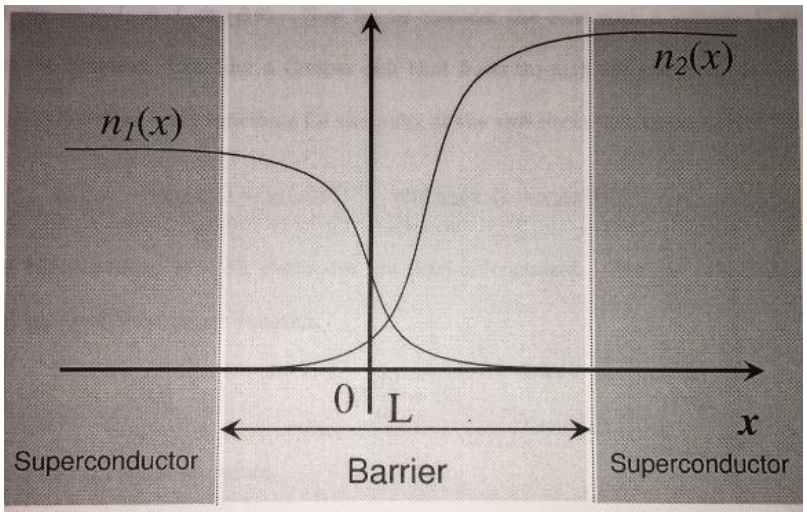


Figure 10. A sufficiently thin layer insulating tunnel barrier causing copper density to overlap [40]

Let us now consider and discuss the different types of the Josephson Junctions that are applicable to the work of this thesis. But before that we will discuss the basic theory of tunneling.

### 1.5.2 Superconductor /insulator/ normal metal (SIN) junctions

Tunneling is the process where electrons can transport from one conducting material to another through a narrow vacuum or a thin insulating barrier. The tunnel current is expressed by the following expression [18]:

$$I = A|T|^2 \int_{-\infty}^{\infty} N_1(E)N_2(E + eV)[f(E) - f(E + eV)]dE \qquad (1.7)$$

where V it the applied voltage, eV is the resulting difference in the chemical potential across the junction, and N(E) is the conductor densities of states on the left and right side in tunnel junction.

Tunneling occurs in many types of junctions with insulating barriers, including with two normal metal electrodes (NIN) a superconductor and a normal metal (SIN) and between two superconductors (SIS). In this thesis we will discuss tunneling in the case of SIN which is relevant to the work discussed in future chapters.

As discussed above, the energy required to break cooper pairs is equal to energy gap ($2\Delta$) in superconductor. Figure 11 (a) shows a SIN junction structure. At 0 K at zero bias, electrons cannot tunnel from the superconductor to normal metal because all density of states are filled, and no electron tunnels from superconductor to normal metal because electron states at the same energy level are either filled or forbidden, as shown in Figure 11(b). As a voltage being applied, the Fermi level of superconductor is raised, and electrons can tunnel through the barrier when the voltage is larger than $\Delta$, as shown in

Figure 11(c). Without thermal excitation (i.e. T=0), the tunnel current is zero when applied voltage is smaller than Δ, and becomes linearly dependent on the applied voltage as voltage increases, as shown in Figure 11(d), and (1.7) becomes

$$I_{ns} = \frac{G_{nn}}{e}\int_{-\infty}^{\infty}\frac{N_{2s}(E)}{N_2(0)}[f(E) - f(E + eV)]dE \qquad (1.8)$$

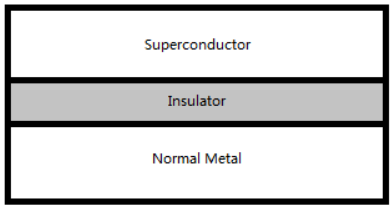


(a)

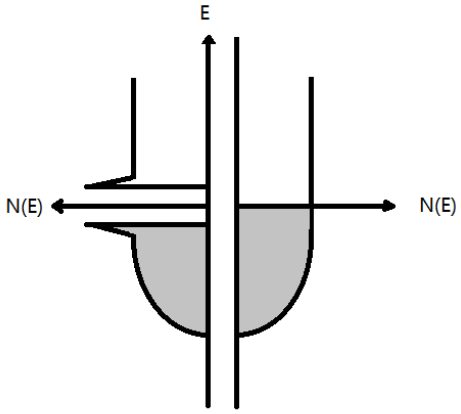


(b)

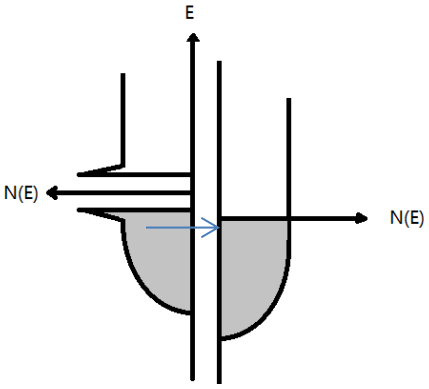


(c)

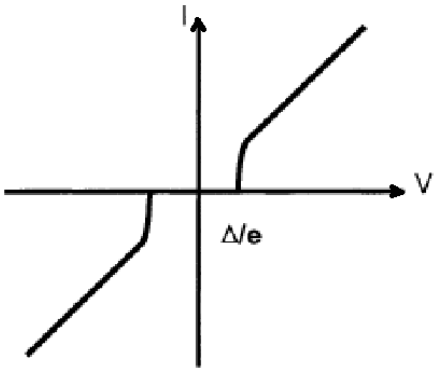


Figure 11. SIN tunneling. (a) SIN junction structure; (b) Energy band diagram with no bias; (c) Energy band diagram with bias; (d) IV characteristic[18]

1.5.3 Superconductor /normal metal/ superconductor (SNS) junctions

Since the focus of this research is on the fabrication and characteristics of Josephson junction with ferromagnetic barrier, it's crucial to discuss the theoretical and electrical characteristics of SNS junctions.

The Josephson effect can occur not just with insulating barrier sandwiched between superconducting electrodes, but also with other barrier materials, including, a metal or a semiconductor. When the barriers are sufficiently conductive, the transport mechanism in these devices is either ballistic or diffusive, instead of tunneling. The details of SNS junction will be discussed next, paving the path in discussing the SFS junction with ferromagnetic barrier.

In the case of SNS junctions, the current voltage (I-V) characteristics show intrinsic non-hysteretic I-V characteristics, as shown in Figure 12. Also the normal barrier layer of the junction can be grown to be few hundreds of nanometers thick. This thickness can be easily controlled while grown, unlike the process that involves growing oxide insulating barrier.

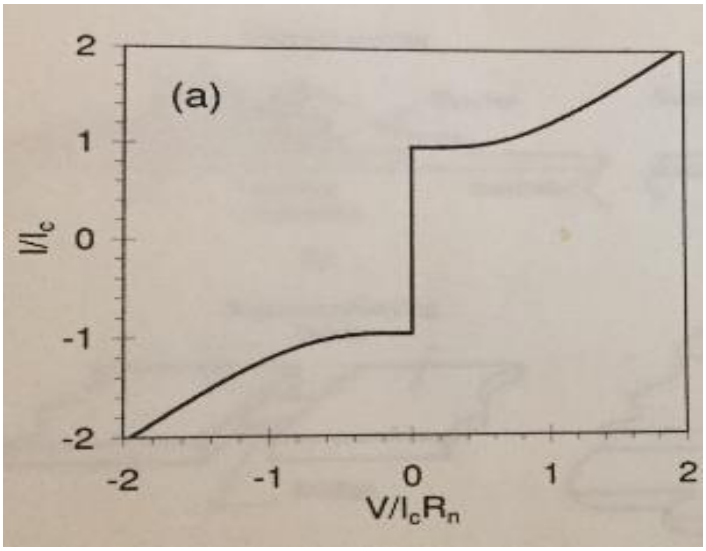


Figure 12. (I-V) characteristics show intrinsic non-hysteretic I-V of SNS junction [40]

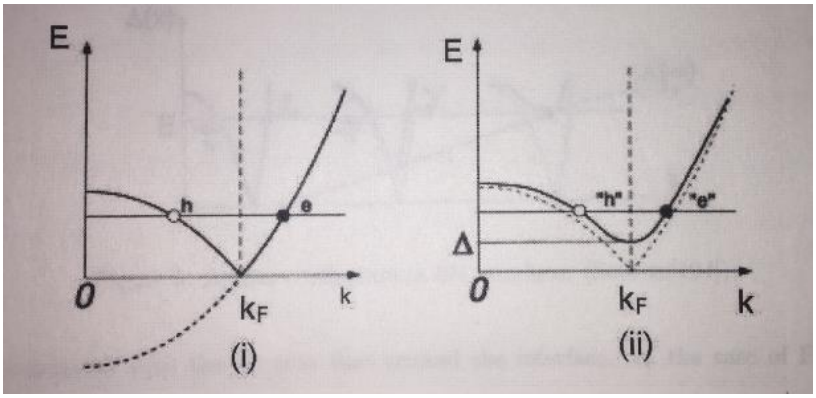


Figure 13. Quasi-particle dispersion relation (i) electrons and holes inside a normal metal (ii) electron like and hole like in a superconductor [40]

In earlier discussion we explained that when a superconductor is grown near a normal conductor, a superconducting correlation can be induced in the normal metal, and the characteristic distance that cooper pairs penetrate into the normal layer is known as the normal metal coherence length $\xi_n$. This remarkable fact that supercurrent can flow through the normal metal interface in SNS junctions is a *result of the Andreev reflection process [28]*.

To understand the Andreev reflection transport mechanism, the quasi-particle dispersion relations for both a normal metal and a superconductor are shown in Figure 13. As depicted in Figure 14, of Andreev reflection at the SN interface, when a quasi-electron of some energy E and velocity v crosses the N/S interface, at the point where E= $\Delta(x) < \Delta(0)$ ( less than the superconductor gap), the quasi-electron changes the branch (from electron like to hole like). The hole that is reflected is correlated to the electron that just crossed the NS interface. In the case of E=0, the reflected hole will follow the path incident electron path. If E>0, then the paths splits as depicted in Figure 14 [40]. Andreev reflection corresponds to an electron below the Fermi level forming a Cooper pair with an electron above the Fermi surface. In the case of the Andreev-reflected hole, it's the hole left by the electron below the Fermi level in this way, dissipative quasi-electron current transforms into a supercurrent when crossing the NS interface. In the reverse direction, Cooper pairs are reflected from the NS interface, where one electron recombines with a hole below the Fermi level and the other electron continues into the normal layer. [41]. Figure 15 illustrates the picture of Andreev-reflection inside the SNS junction.

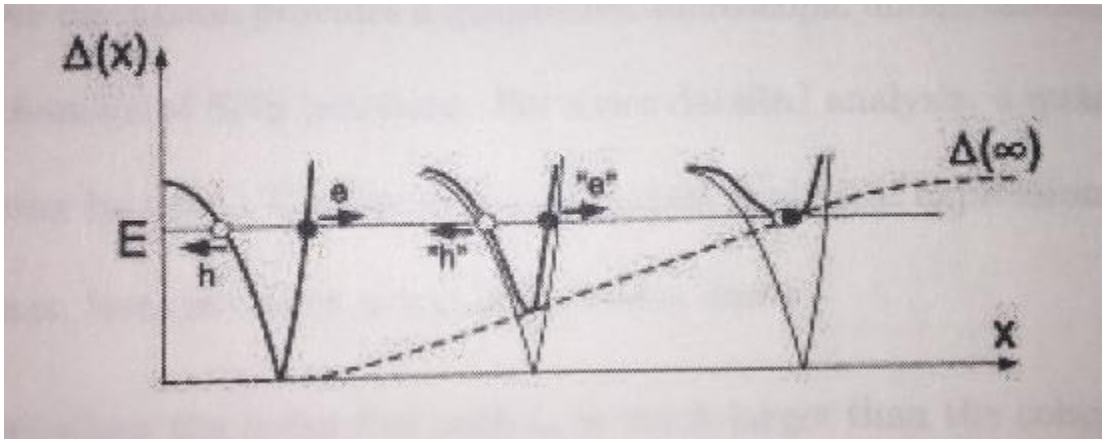


Figure 14. The superconductor order parameter as a function of space to describe the Andreev reflection at the NS interface [41]

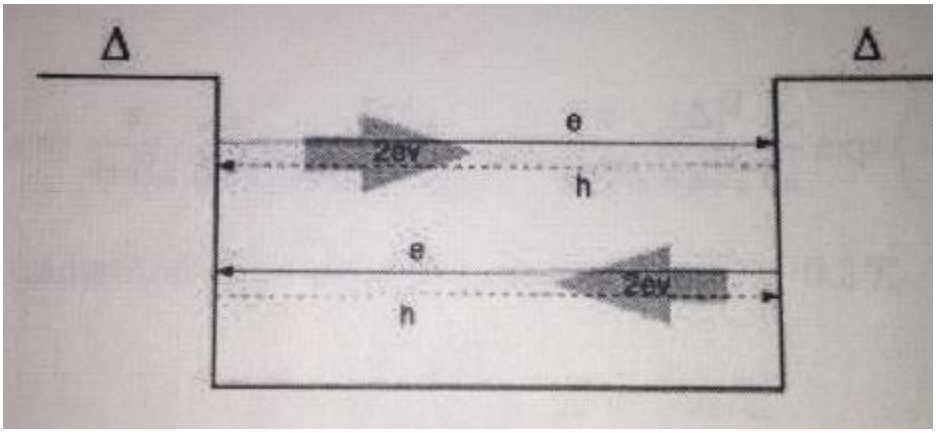


Figure 15. Andreev reflections at the SNS junction [41]

For more detailed analysis, a quantitative microscopic theory must be used. One of these theories was proposed by de-Genes [26] in 1964. Based on the phenomenological Ginzburg-Landau equations, de-Gennes found:

$$I_C = \frac{\pi}{4eR_n}\frac{|\Delta^2|}{K_B T_c}\frac{L/\xi_n}{\sinh(\frac{L}{\xi_n})} \cong \frac{\pi}{4eR_n}\frac{|\Delta^2|}{K_B T_c}\frac{L}{\xi_n}\exp\left(-\frac{L}{\xi_n}\right) \qquad (1.9)$$

for long junctions (where the barrier thickness L is larger than the coherence length $\xi_n$) and under the dirty limit (where the mean free path $l_n$ is much less that the coherence length$\xi_n$), where $\xi_n$ is defined in equation 1.3 and $R_n$ is the normal layer resistance [26] .

1.5.4 Superconductor /ferromagnetic/ superconductor (SFS) junctions

SFS junctions known as ferromagnetic Josephson junctions will be discussed in this section. These junctions will be of importance of our future discussion of the fabrication of a superconducting cryogenic memory.

The current-phase relation in a SIS or SNS Josephson junction is given by, $Is = I_c \sin(\varphi)$, where $\varphi = \theta_1 - \theta_2$ is the phase difference between the macroscopic superconducting wavefunction in each superconductor electrode and $I_c$ is the supercurrent in the device. The Josephson coupling energy is given by $U = -E_j \cos\varphi$ where, $Ej = (I_c\varphi_0)/2\pi$ is the *Josephson energy*. For conventional Josephson junctions the minimum Josephson energy befalls at $\varphi = 0$.

Bulaevskii *et al.* [42] calculated in 1977 the critical current through a Josephson junction with magnetic impurities in the normal barrier (N) and projected a $\pi$ shift in the current phase relation for the certain number of magnetic impurities. The current phase relation of such junction is then given by $I_s(\varphi) = I_c \sin\varphi = I_c \sin(\varphi+\pi)$ and the Josephson will be $U = -E_j \cos(\varphi+\pi) = E_j \cos(\varphi)$, signifying the presence of $\varphi=\pi$ in the ground state . These types of junctions are called the $\pi$ Junction.

The oscillating pair correlation in the F layer of a SFS Josephson Junction leads to oscillation in the critical current as a function of F layer thickness. This was first observed by Ryazanov and his co-workers [43, 44] using a weak ferromagnetic alloy

CuNi. Recently the Blamire group [32] have shown oscillatory Josephson characteristic voltage ($I_cR_n$) as function of ferromagnetic layer thickness using stronger ferromagnets like, Ni, Co, Fe, Py ($Ni_{80}Fe_{20}$). These oscillations of the critical current as a function of F-layer thickness for the case of weak ferromagnet, CuNi [43], and for the case of a strong ferromagnet Ni [32] are shown in Figure 16. The transitions between the "0-state" and "π-state" as the F-layer thickness increases are also shown.

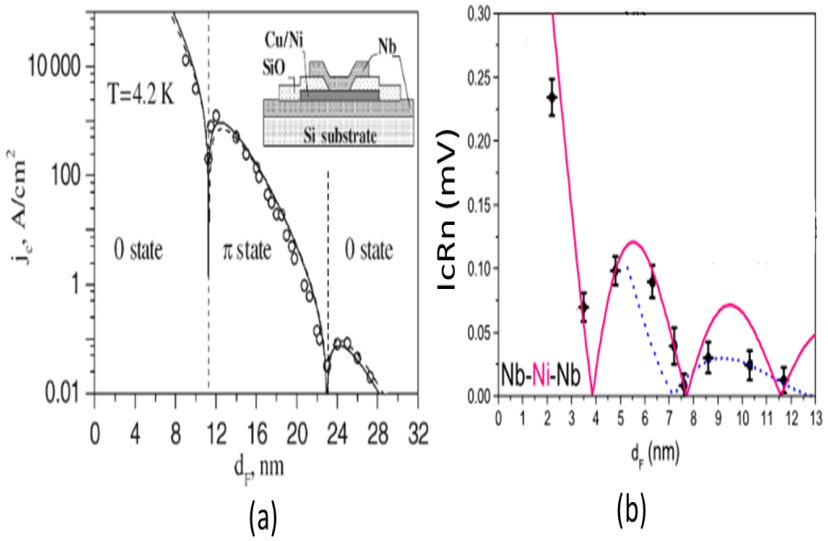


Figure 16 a) Oscillations of the critical current density $J_c$ as a function of the CuNi layer thickness (b) Oscillations of the characteristic voltage $I_cR_n$ as a function of the Ni layer thickness [43, 32]

1.5.5 Magnetic field dependence of the critical current

A magnetic field perpendicular to the junction current can modulate the critical current. As shown in Figure 17(a), a magnetic field H applied in the y direction will cause a magnetic field inside the junction which is equal to [45]

$$\varphi(x) = \frac{2\pi d}{\Phi_0} H_y x + \varphi_0 \qquad (1.10)$$

where $\Phi_0$ is the flux quantum , and $\varphi_0$ is an integration constant. The current density on x direction, as shown in Figure 17(b), can be expressed by

$$J(x) = J_1 \sin\left(\frac{2\pi d}{\Phi_0} H_y x + \varphi_0\right) \tag{1.11}$$

where $J_1$ is the maximum current density. The total current in the junction can be obtained by integration

$$I_1(k) = \left| \int_{-\infty}^{+\infty} dx J(x) e^{jkx} \right| \tag{1.12}$$

where $k = \frac{2\pi d}{\Phi_0} H_y$.

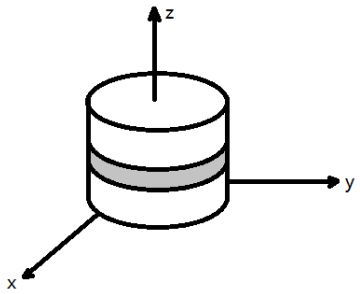


(a)

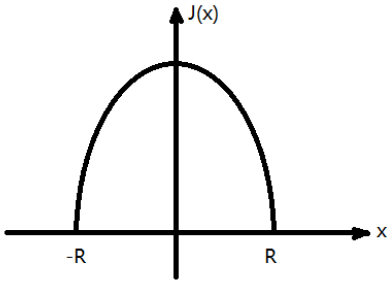


Figure 17.(a) Geometrical structure of circular Josephson junction (b)Current density J(x) distribution of circular Josephson junction [46]

In a circular geometry junction, the current density is given by

$$J(x) = \int_{-\sqrt{R^2-x^2}}^{\sqrt{R^2-x^2}} dy J_1 = 2J_1\sqrt{R^2 - x^2} \tag{1.13}$$

After integration, Matisoo [56] showed the magnetic field dependence of critical current is given by

$$I(k) = I_1 \left| \frac{\text{Bessel } J_1(kR)}{\frac{1}{2}(kR)} \right| \tag{1.14}$$

where $I_1 = \pi R^2 J_1$, and $J_1(x)$ is a Bessel function of the first kind. Figure 18 shows such behavior of $I_c$ as a function of applied magnetic field [46]

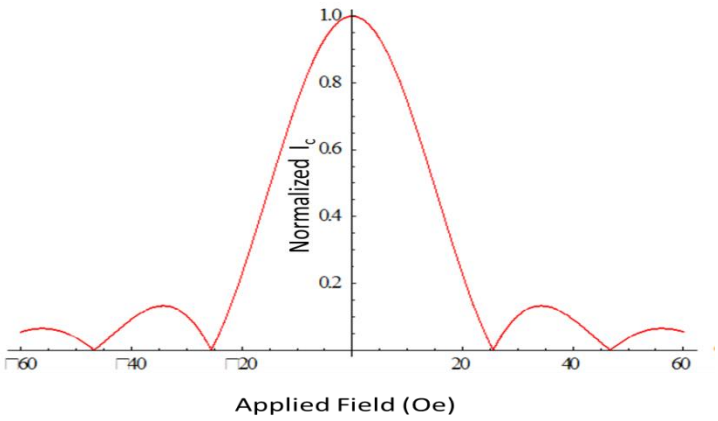


Figure 18. Theoretical magnetic field dependence of Josephson current for a circular junction [46]

Performing this measurement can be used to determine if the critical current is distributed uniformly through the junction or due to one or a number of transparent regions or shorts that are not distributed uniformly across the junction.

1.6 Superconductor/ ferromagnetic cryogenic based memory

The goal of this project is to develop and optimize the performance of a Josephson Magnetic Random Access Memory (JMRAM) cell comprised of SFNF'S (Superconductor- Ferromagnetic -Normal-metal- Ferromagnetic Superconductor)

Josephson junction structures for high-speed high-density cryogenic memory applications. Given success in this project, we anticipate that compact non-volatile memory cells can be produced with sub-ns access times and high write-erase endurance. The development of these devices, in conjunction with SFQ circuit technology, could potentially enable the production of computing systems with higher speed and lower wall-plug power.

JMRAM is a new superconducting memory technology recently invented by Northrop Grumman/Electronic Systems (NGC) [13]; depending on the device structure can also be referred to as spin-toggle, spin torque, tunnel and/or spin valve. In JMRAM the state of a bit is recorded using the magneto-current states of a structure comprising one or more thin film ferromagnetic regions. High and low Josephson critical currents correspond to the logical states of the cell. Our approach encodes and stores information in the parallel or anti-parallel alignment of magnetic layers in the device, and reads out the information by measuring the modulation of the device's Josephson critical current.

Operation of the JMRAM is fully analogous to conventional MRAM. MRAM exhibits high speed, nonvolatility with high write-erase endurance, and high storage density. This implementation has all the advantages of conventional MRAM but with much lower energy read cycles, smaller write currents and non-dissipative interconnects.

If our program is successful, this will enable the development of Josephson-based supercomputers with large and sufficiently fast memory.

There is strong evidence that novel and revolutionary information processors can be built using superconductor logic elements. Individual devices have switched at 770 GHz and large circuits have demonstrated above 100 GHz operations. To achieve the full potential of Nb-based logic circuits for direct signal digitization for software-defined radio [6, 7] and router applications [8] will require the realization of a fast, ultra-low power memory technology. The demands for memory are markedly greater if a high-end computer is considered. In the recent Superconducting Technology Assessment (STA) performed by the NSA [9], the lack of a superconducting memory technology was identified as the most critical problem for the high-end computing application. Satisfying this need is the goal of the proposed project.

There have been many potential solutions for achieving the needed performance of memories for a superconductor supercomputer, although all of these approaches have fallen short of the density, speed and/or energy requirements (Table 1). Some of the devices are based on manipulating magnetic flux quanta [10, 11], but they cannot achieve high density as a result of the large size of the obligatory inductive loop. A hybrid solution has been developed with a combination of CMOS technology logic and Josephson junction state detection; however this memory consumes large amounts of power [12] The STA report also considers magnetoresistive RAM (MRAM). This approach is appealing given that MRAM is non-volatile, the device speed is comparable to DRAM, and the potential density is greater than SRAM. Unfortunately, at room

temperature operation, the write energies are too high in the field-switched Toggle MRAM, and spin torque ST-MRAM has insufficient stability against thermal fluctuations. However, the conventional implementation of MRAM, where the readout is based on the tunneling magnetoresistance effect, is limited in utility because the readout uses significant energies because it uses a resistance measurement. The resistive nature of the memory cells requires that they be connected in parallel for readout. This in turn requires each cell to have an isolation transistor that complicates cryogenic operation and degrades power efficiency. A variation on this theme is the focus of our proposal. Compared to conventional MRAM, our approach offers faster access time due to the superconducting interconnects and three orders of magnitude less power dissipation by allowing readout of series-connected elements (eliminating the need for isolation transistors), and reducing readout power dissipation to a level similar to that of a few SFQ pulses.

Table 1. The status of the various low-latency cryo-RAM approaches published in the NSA's STA report [9]

| Type/Lab | Access Time | Cycle Time | Power Dissipation | Density | Status |
|---|---|---|---|---|---|
| Hybrid JJ-CMOS (UC Berkeley) | 500 ps for 64 kb | 0.1 - 0.5 ns depending on architecture | 12.4 mW read 10.7 mW write (Single cell writing) | 64 kb in < 3x3 mm² | All parts simulated and tested at low speed |
| RSFQ decoder w/ latching drivers (ISTEC/SRL) | ? | 0.1 ns design goal | 107 mW for 16 kb (Estimate) | 16 kb in 2.5 cm² (Estimate*) | 256b project completed (Small margins) |
| RSFQ decoder w/ latching drivers (NG) | ? | 2 ns | ? | 16 kb/cm² * | Partial testing of 1 kb block |
| SFQ RAM (HYPRES) | 400 ps for 16 kb (Estimate) | 100 ps for 16 kb (Estimate) | 2 mW for 16 kb (Estimate) | 16 kb/cm² * | Components of 4 kb block tested at low speed |
| SFQ ballistic RAM (Stony Brook University) | ? | ? | ? | Potentially dense Requires refresh | Memory cell and decoder for 1 kb RAM designed |
| SFQ ballistic RAM (NG) | ? | ? | ? | Potentially dense Requires refresh | SFQ pulse readout simulated |
| MRAM (40K) | Comparable to hybrid CMOS | Comparable to hybrid CMOS | < 5mW at 20GHz (Estimate) | Comparable to DRAM (Estimate) | Room temperature MRAM in preproduction; Low temperature data sparse |

*Densities of JJ memories are given for the technologies in use at the time of the cited work. Greater densities can be expected when a 20 kA/cm² process is used. The symbol ? signifies insufficient data.

The JMRAM memory works in the following manner. The SFNF'S structure contains one hard magnetic layer, such as Co or Ni, or a permalloy (Py), for the fixed layer, while the other magnetic layer, often dilute Permalloy with transition metals like Cu, Nb or Cr, or PdNi alloys, for the free layer. The free layer stores the information and can be switched between two states using a magnetic fields generated locally by orthogonal electrical currents. The direction of magnetization of the free layer of the SFNF'S structure represents the memory state, a 0 or 1, in the JMRAM memory cell.

The rows in each array are traversed by parallel Nb *word-lines*, while the columns are traversed by parallel Nb *bit-lines*. Storage cells are positioned at the intersections of wordlines and bitlines; this allows each cell to be identified and accessed by a row and column address. The storage cell contains a SFNF'S Josephson junction magnetically coupled to Nb wordlines and bitlines. The currents in both of these superconducting lines are used to create magnetic fields at the desired cell location(s) to switch the free layer. Such junctions exhibit different Josephson tunneling critical currents and/or phase shifts when the free layer is parallel or anti-parallel to the fixed layer. The memory state of the bit is read using the Josephson currents. Figure 19 shows a sample structure of the proposed JMRAM cell.

The feasibility of the JMRAM concept is substantiated by an example in the recent progress in manipulating the superconducting critical current as it transverses through thin magnetic layers by their magnetization. Other ways been explored are phase sensitive junction, where detecting the phase of the junction if in the 0 or $\pi$ state .Most importantly, it has been shown that an SFNFS Josephson structure with a proximity barrier has a hysteretic critical current that tracks the hysteresis in the magnetization of the free layer with a large magneto-current ratio [47], This approach warrants consideration because of the potential for ns switching times, switching fields $H_{sw}$ ~order 10's of Oersteds (and corresponding switching currents of 0.1 mA), Josephson magnetocurrent ratios of over 50% between the high/low memory states, high read/write endurance and sufficient stability of the memory state at 4.2 K.

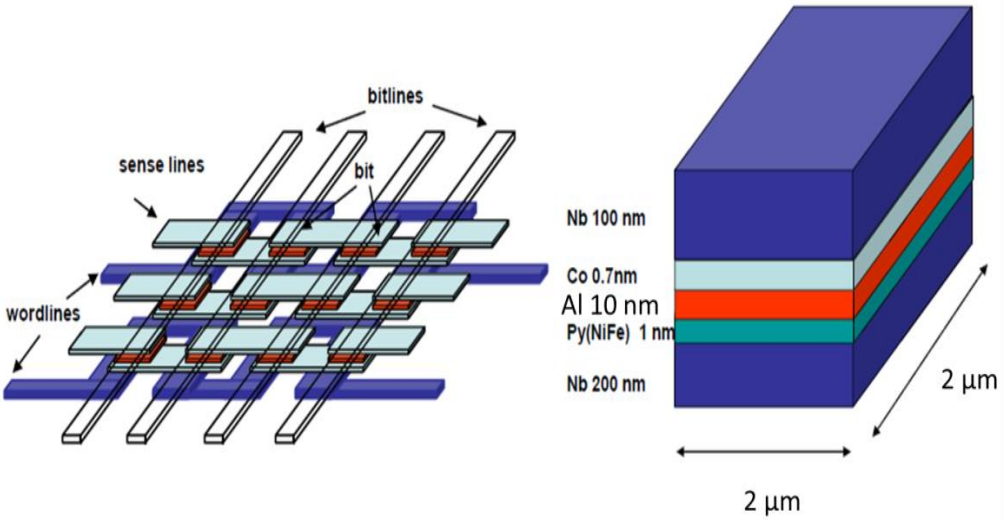


Figure 19. JMRAM: topological sketch (left) and possible memory structure element based on SFS Josephson junction [13]

The major scientific and engineering challenge of the project is to develop a reliable fabrication method of SFIFS structures for high density JMRAM with the following properties:

1. ns switching times
2. switching fields on the order of tens of Oersteds
3. Josephson magnetocurrent ratios of over 50% between high/low memory states
4. high read/write endurance
5. sufficient nonvolatility of the magnetic memory state at 4.2 K
6. Superconducting and magnetic materials compatible with low temperature and fabrication processes.

In this thesis, we will present our approach for materials optimization for the free and hard magnetic layers and recent data on device fabrication and characterization of the proposed JMRAM cell.

## 1.7 Research plan and thesis organization

In Chapter 2, an overview of the thin film sputtering growth technique along with the design and assembly of special load lock ultra-high vacuum (UHV) chamber for sample growth. In the second part of the chapter, we will discuss the analysis and characterization techniques used in this research

In chapter 3, the process of fabricating Josephson junctions is detailed, including both the shadow mask and the lithographic processes are discussed. We also will discuss the various tools that were used in the fabrication process

In chapter 4, we will discuss our approach in investigating low saturation magnetization $M_s$ and Curie temperature $T_{curie}$ for magnetic materials to be used in potentially more energy efficient JMRAM memory cells. In this chapter we will discuss the growth and electrical and magnetic characterization of Cu doped permalloy and the use of $(Cu_{30}(NiFe)_{70})$ as a soft F layer in the SFNF'S JMRAM device.

In chapter 5, we will discuss the growth, fabrication of our proposed JMRAM cell. We will start with investigating the proximity effect induced in S/F/S structure with F being Permalloy ($Ni_{80}Fe_{20}$), and how the critical current behaves as a function of the F layer thickness and does it show the 0-π junction characteristics discussed in chapter 1. Then later, after finding the 0-π cross over for the hard layer ($Ni_{80}Fe_{20}$), we

study the electrical switching properties of the JMRAM cell composted of the two F layers hard ($Ni_{80}Fe_{20}$) and soft ($Cu_{30}(NiFe)_{70}$).

In chapter 6, we will study the proximity effect in Nb/F bi layers in detail. In this work we look on how different magnetic system influences the superconducting order parameter and the decay lengths. We introduce our own simple model to model the non-monotonic critical temperature $T_c$. We also compare our results in the bi-layer systems with those in tunneling junctions.

In chapter 7, the work is concluded and plans are made for future studies for superconducting/ferromagnetic structures in studying the proximity effect and magnetic evolution on those structures.

# CHAPTER 2 THIN FILM GROWTH METHOD AND CHARACTRIZTION TOOLS

Thin film growth using planar magnetron sputtering is one of most common methods used in the growth of superconducting and magnetic films. Hence, in this chapter we will discuss this method and the design and construction of the synthesis method. Several analytical techniques were used to characterize the electrical, structural and topological properties of the Nb and magnetic films and device structures, including Rutherford backscattering spectroscopy (RBS), atomic force microscopy (AFM), Transmission Electron Microscopy (TEM), Vibrating sample magnetometer (VSM) and 4-point electrical I-V measurement.

In this chapter, the scientific background of the growth and analysis techniques is discussed.

## 2.1 Thin film growth requirements

For Josephson junction devices, high-quality and high-purity Nb films with high transition temperature (>9 K) superconducting gap energy of ~ 1.4 mV at 4.2 K are required. The superconductive properties of Nb thin films in Josephson junction electrodes depend on the purity of the material itself. Also Nb electrodes need to be on the order of at least 100 nm to achieve near their full potential superconductive properties, since the Nb coherence length is about 80 nm.

Another requirement for the superconductor (S) electrode is to be .as smooth as possible at such thickness, so any material grown on it will fully cover the Nb (S) electrode. For thin barriers that are on the order of a few nm, the surface RMS (root mean square) roughness of the electrode should be no more than 1 nm or lower if possible. For practical junctions, the Nb electrode thickness is usually kept at 50 – 200 nm. Another

important reason to develop smooth films is that the magnetic material's switching field is increased markedly if deposited on rough films. These reasons promote that need for smooth superconductor electrode.

According to the S/F proximity theory [48, 49], three main regimes of $T_c(d_F)$ can be realized in S/F bilayers depending on the thickness of the superconducting layer :

1) For a large enough thickness $d_S >> \xi_S$ , so that $T_c(d_S) \sim (0.4-0.8)T_{c0}$ , the superconducting $T_c$ oscillates as a function of the ferromagnetic layer thickness $d_F$ ;

2) For a thinner superconducting layer $T_c(d_S) \sim ((0.2 \quad 0.3)T_{c0})$ the regime of re-entrant superconductivity can be realized, i.e. the superconducting transition temperature drops to zero when increasing the ferromagnetic layer thickness $d_F$ , but with a further increase of $d_F$ the superconductivity restores again showing damped oscillations around a certain asymptotic value [50];

3) For the thickness $d_S < ds_{critical}$ , where $ds_{critical}$ is the critical thickness, where the superconducting *Tc* quickly falls down to zero upon increasing $d_F$ [51] .

Clearly, for our experiments to observe the non-monotonic behavior caused in S/F bi layers we need to operate in the above regime 1):$d_S > ds_{critical} > \xi_S$. Because of the large thickness of our Nb films we did not take into account additional mechanisms of $T_c$ depression caused by reduced dimensionality of pairing and enhanced Coulomb repulsion [52,53], which become important in thin superconducting films with $d_S < \xi_S$ .

Growth conditions are also important in the optimization of our materials. It's well known that growth chambers tend to outgas, and when sputtering, the chamber walls will have enhanced outgassing as a result of the presence of the energetic plasma.

Oxygen is the most common impurity in Nb films, as a result of the dominant residual water vapor contamination in our unbaked UHV growth chamber. So to obtain Nb films with the best quality, vacuum pressures better than $10^{-8}$ Torr and growth rates higher than 5 Å/s are desired. It's a fact that 1% of oxygen impurity in the bulk of the film will reduce the Tc by ~1 K [54].

## 2.2 Overview of sputtering

Sputtering is a process whereby atoms are expelled from a solid target material due to bombardment of the target by energetic particles created in plasma [55]. This phenomena was first observed by W.R Grove after he observed that a cathode material transfer onto a polished silver plate during a gaseous discharge experiment [56].

The sputter process, as schematically illustrated in Figure 20, occurs in four steps: (1) ions are produced and directed toward the target material to be deposited, (2) these high energy and heavy ions sputter atoms from the target, causing the release of target atom from their bonds, (3) majority of the ejected atoms are transported to the substrate in the chamber and (4) condense and form a thin film of the target material on top of the substrate [55]. When the target surface of the material to be sputtered is bombarded with atoms, ions or molecules at different energy levels, the following physical process happen: (1) some of the incoming ions energy is transferred to the solid target material as heat or lattice damage, (2) other part of the energy causes some the atoms from the surface of the solid target to be dislodged and ejected into the gas phase [55].

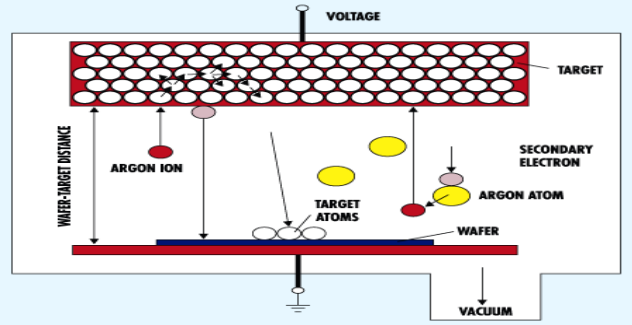


Figure 20. A schematic diagram illustrating of metal deposition process in Argon sputtering [57]

Thin film deposition by sputtering can be performed inside a vacuum chamber with an inert gas, such as argon, injected into the chamber. The inert gas will be the primary source of bombarding ions. A DC or RF power is applied between the anode and the cathode to energize the sputter process. In these systems, the discharge species is the plasma, which consists of positive ions, electrons and neutral species in a quasi-neutral electrical state. Once the plasma is ignited, positively charged gas ions start bombarding the negatively biased target and hence lead to the dislodging of target atoms through the energy transferred from the striking gas ions. Then the target atoms ejected toward the substrate and the ones with sufficient kinetic energy will reach the substrates and be deposited on the substrate as shown in Figure 21 [55].

To make such process more efficient and increase the yield of sputtering, planar magnetron sources place magnets at the back of the target. During the sputter process, this magnetic field caused by the magnets can be used to trap secondary electrons close to the target. The electrons follow helical paths around the magnetic field lines resulting in more ionizing collisions with neutral gaseous near the target than would

otherwise occur. This enhances the ionization of the plasma near the target leading to a higher sputter yield (more sputtered target atoms). It also means that the plasma can be sustained at a lower gas pressure. The sputtered atoms are electrically neutral and so are unaffected by the magnetic trap. Most sources, including the planar magnetron sources used in this study, cool the target directly or indirectly with water during the sputter process. The coolant water will prevent any damage occurring to the magnets behind the target, and the target itself due to heating.

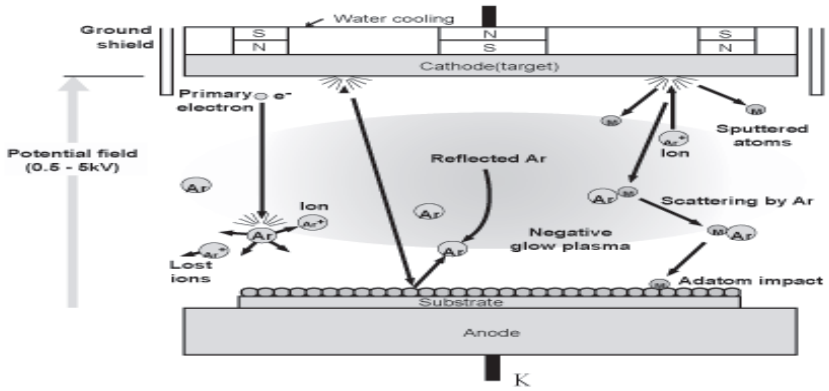


Figure 21. A schematic diagram of vacuum chamber with plasma and the sputter environment inside it [58]

DC and RF sputtering are typically used in the process of depositing conducting materials, whereas RF sputtering is required to sputter non-conducting semiconductor and insulating materials [55]

## 2.3 Sputter chamber design and assembly

The starting point for our growth chamber design was a stainless steel chamber with 4 each 10” OD, Conflat™ flanges to be used as the main chamber and another stainless steel chamber with 4 each 6” OD Conflat™ flange to be used for the turbo-

pumped load lock. We also used a load lock assembly with a 36" stroke magnetic linear translator and a 2" substrate holder with heating capabilities up to 900 $C^{\circ}$.

One of the criteria of our design was to reduce the background contamination before and most importantly, during deposition. So, to achieve a film with less than 1% impurities, it is necessary to use a pure target, pure Argon gas for plasma generation, and to control the impurities emanating from the chamber and the system as a whole to remain below certain level. Typically, we deposit our Nb films at a rate of ~6 Å/sec. If we wish to maintain at least 99% purity in the film, we assume a sticking factor of unity for contaminants; it means we must keep their partial pressure below $7\times10^{-9}$ Torr. Then, if we use 99.9999% pure argon and sputter at 1 millitorr, the sputter gas will contain$10^{-9}$ Torr of impurities. If we can accomplish those goals, less than 1% off impurities can be present in the film.

A second criterion for our design is to prevent cross contamination from one source to another source while sputtering. So we fabricated shutters specifically designed to keep unexposed targets from being in direct line-of-sight to the plasma in the chamber. Since we will be working with superconductors and ferromagnetic systems, any unintentional magnetic impurities in the superconducting film will reduce its critical temperature radically.

The planning started with the design of the chamber in SolidWorks Figure 22, and then moved into the assembly stage. The final chamber assembly called later the SF UHV chamber is shown in Figure 23. The chamber reached an ultimate base pressure in the low $10^{-9}$ Torr.

Another existing UHV chamber was used for the growth of the JMRAM devices. This chamber was equipped with 6 sputter sources housing different sputter targets like Nb for superconducting electrode, Al or Cu for normal metal layer, and different magnetic compound targets including Fe, Co, NiFe (permalloy) , and PdNi (palladium nickel).

The detailed of the growth conditions of each material will be discussed in each chapter separately.

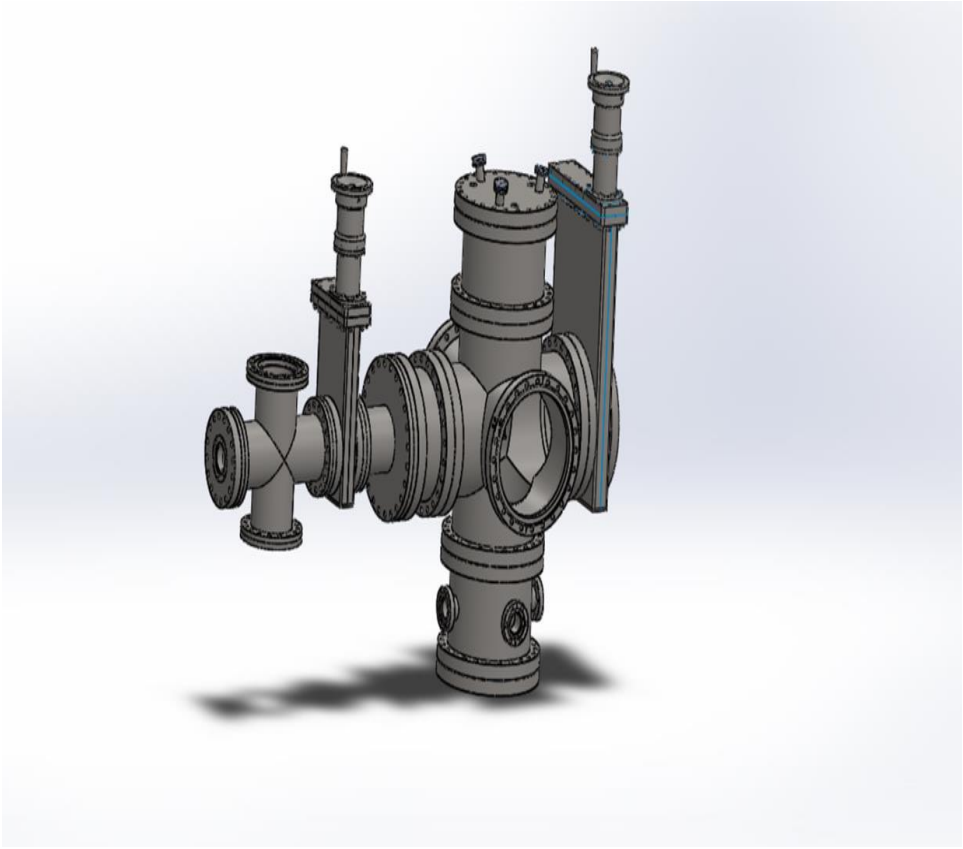

Figure 22. SolidWorks design of the SF UHV chamber

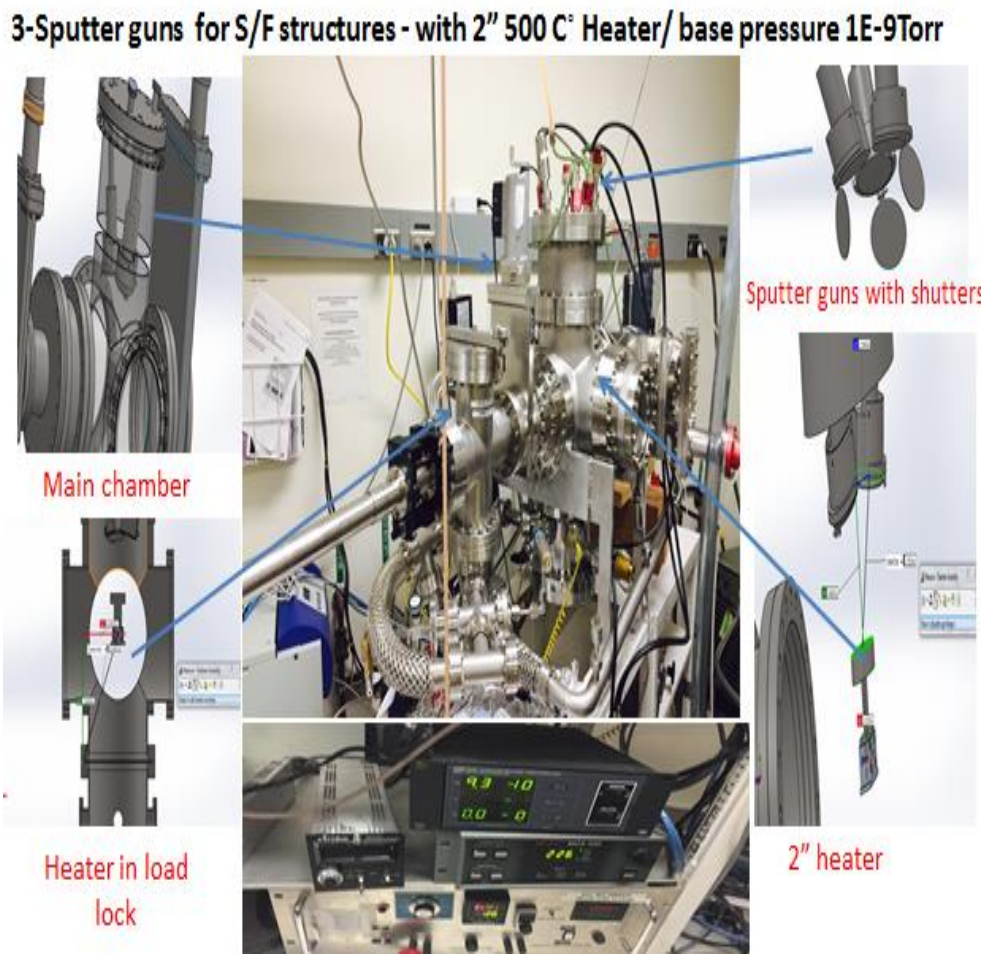


Figure 23. A UHV chamber that was designed and assembled at ASU for this project

2.4 Overview of thin film analysis tools

The films and structures made by vacuum growth mentioned above were characterized for their compositional, topology, electrical, magnetic and structural properties. The characterization methods used for material studies will be discussed in this section.

2.4.1 Rutherford backscattering spectrometery (RBS)

RBS is a technique that used mainly to determine the compositions and thickness of the grown films. This non-destructive method can detect the amount of different elements in films from the surface down to about 2 microns. RBS uses a high-energy α-particle beam to characterize the layer composition of thin films. The α-particles impinge through the sample surface, and are scattered backwards by the coulombic charge of the sample's nuclei. α-particles scattered from each element's nuclei will have a different backscattered energies and can be collected by a detector. The system at ASU is a 1.7 MeV tandem accelerator with a beamline and sample space chamber. The Tandetron accelerator is a Cockroft-Walton, gas-insulated high frequency device which can use either a gas source for ions (H, He, N, O, etc.) or a sputter source for heavy ions (MeV implantation) and has a 3 mm radius beam size. A software program (RUMP) is used to simulate the elemental information and compared with the actual spectrum by its area concentration.

Nuclear resonant scattering $^{16}O(\alpha, \alpha)^{16}O$ was also used to increase the sensitivity for detecting oxygen in the films. RBS channeling can be used to determine the epitaxy of the thin film by comparing the number of reflected particles from a normal crystal structure direction and a random direction.

2.4.2 Atomic force microscopy (AFM)

AFM is a method used to characterize the surface topography of a thin film. A Digital Instruments Nanoscope III AFM was used to characterize the surface roughness of Nb and bi-layer structures. A silicon nitride tip of atomic dimensions is used to scan the film surface.

In tapping mode, the cantilever is deflected by the Van Der Waals force between the tip and the sample atoms when it is a few angstroms from the sample surface. The deflecting movement of the cantilever is measured by a laser beam reflected from the cantilever and then the deflection is interpreted in terms of height of the tip from the sample surface. The resolution in the direction perpendicular to the substrate can be less than an Angstrom and in the lateral direction, less than an Angstrom.

### 2.4.3 Transmission electron microscope (TEM)

In this work we used analytical and imaging TEM on S/F bi layer system with a range of ferromagnetic layer thicknesses. The EDX and EELS analytical work used both line scans and chemical mapping. Selected area diffraction measurements were used throughout the work to assist in the identification of the phases and crystal orientation

. The key goal is to determine how the atomic structure, microstructure, chemical intermixing, strain and topography of the ferromagnetic layer evolves in Nb/ferromagnetic bilayers as it is deposited to thicknesses from 0- 7 nm JEOL ARM200F microscope at LE-CSSS will be used for this study.

### 2.4.4 Cryogenic electrical measurements

In studying the electrical properties of the thin films, a cryogenic dipping probe inserted into a liquid helium Dewar was used. To make resistivity measurements as a function of temperature using a 4-point in-line measurement, the thin film is contacted using four spring loaded contacts, where the outer two contacts source current I and the inner two contacts are used for measuring the voltage V across the two contacts. The

sheet resistance of the film (in Ohm) could be thus calculated by

$$R_s = V/I \qquad (2.1)$$

and given the thickness d (in cm) of the film measured by RBS, the resistivity $\rho$ (in μΩ.cm) of the Nb film could be calculated as (shown in D. K. Schroder's Semiconductor Material and Device Characterization)

$$\rho = 4.532R_s \times 10^6 \times d \qquad (2.2)$$

Residual resistivity ratio (RRR) is defined as the ratio of sheet resistance (or resistivity) of a Nb film at 300 K and at 10 K. For superconductors, this analysis is performed above $T_c$. Phonons and point, line, planar and 3-dimensional defects scatter charge carriers scatter charge carriers. In metals, the phonon scattering contributes a strongly-temperature dependent contribution to resistivity, while defect scattering contributes a temperature independent $\rho_0$ value. Thus, a large RRR is associated with a purer sample with little defect scattering [59]. A good Nb film sputtered at RT will have RRR of 3 to 5. Higher growth temperature will largely improve the RRR, as the epitaxy of the film is improved.

To measure Josephson junctions, we perform the measurements at 4.2 K. Before measurement, the samples were stored in anti-static boxes and transferred into the shielded room for electrical measurement. The wire-bonded chip carrier with the sample was plugged into a home-made dipping probe and inserted in a Liquid Helium Dewar as shown in Figure 24. The measurement was performed inside a shielded Faraday cage to minimize the noise from the external environment. To avoid damage due to electrostatic

discharge, the relative humidity in the shielded room was maintained at around 40% during the experiments and antistatic floor mats were placed under all measurement equipment. Grounding wrist straps were used when the samples were handled. BNC cables were connected through the Faraday cage wall to the measurement system outside the shielded room. RF filters were installed on the feed-through of the cables. The measurement system outside the shielded room consists of a Keithley 220 current source, a HP 34401A multimeter as a voltage meter and a PC recording the data with a C++ program, as shown in Figure 25. Each measurement plot consists of 400 points of current data points that are equally spaced. The IV characteristics are generated by Excel, and the conductance (G) is calculated by fitting the slope of the closest five data points using the LINEST function.

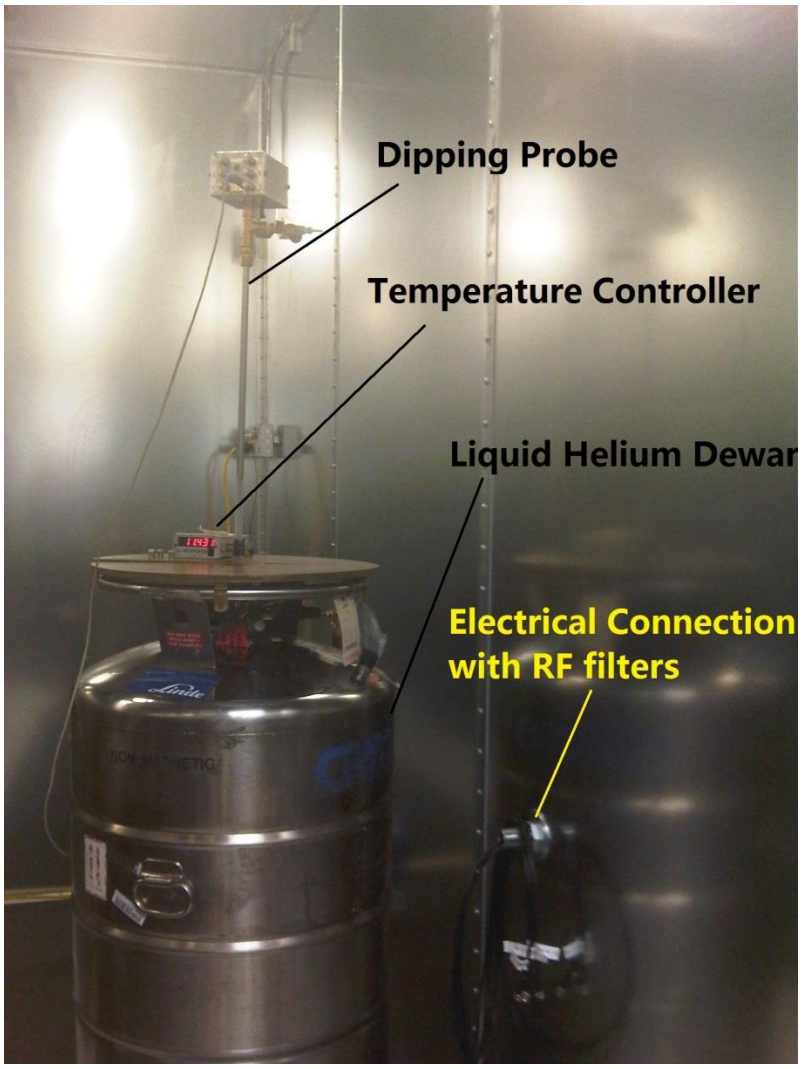


Figure 24. Helium Dewar and dipping probe inside the shielded room during Josephson junction measurement

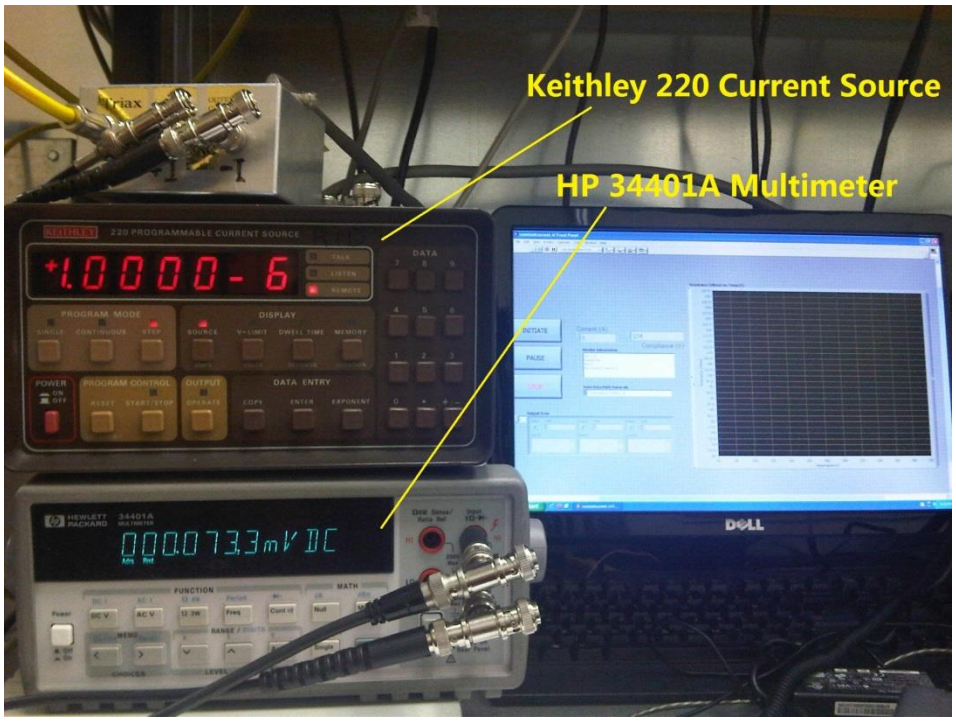


Figure 25. Picture of electronics apparatus used in I-V measurement

A home-made Helmholtz copper coil is placed outside the Dewar to produce magnetic fields so we can modulate the critical current during our measurements. The Helmholtz coil is made up of two parallel coils whose average distance is the same as the inner radius, 0.338 m. The coils both have 1000 turns. The magnetic field is directly proportional to the electric current through the coils. The two coils are connected in parallel. The resistance of each one is about 90.8 ohms. The maximum current can be applied is roughly 1 amp, corresponding to 15 Gauss.

2.4.5 Vibrating sample magnetometer (VSM)

A Vibrating Sample Magnetometer (VSM) [Quantum Design, Model Physical Property Measurement System (PPMS)] is a fast and sensitive DC magnetometer. For

this measurement, a sample of size 4x4x $mm^3$ is inserted into the PPMS Dewar through detection pickup coils, and then an applied field is driven parallel to the sample surface. Then the sample is driven in an osculation mode and then the induced voltage is picked up by the coils. Using relatively large oscillation amplitude (1–3 mm peak) and a frequency of 40 Hz, the system is able to resolve sample magnetization changes of less than $10^{-6}$ emu at a data rate of 1 Hz.

As discussed in [60], the VSM involves mainly of a VSM linear motor transport (head) for vibrating the sample in the sample space of the Dewar, a coilset puck for voltage and magnetic detection, special electronics for driving the linear motor transport and detecting the response from the pickup coils, and a MultiVu software program for measurement automation and control [60]. The system allows the user to vary the temperature from 1000 to 1.8 K along with varying the magnetic field from -9 to 9 Tesla (T). The system is shown in Figure 26.


Figure 26. ASU-QD PPMS system for low temperature magnetic measurements

# CHAPTER 3 FABRICATION PROCESS OF JOSEPHSON JUNCTIONS

## 3.1 Overview of Josephson junction fabrication process

A microfabrication process was used to define junctions with widths of a few microns. This is required to minimize the chances of an electrical short in the junction that is due to a pinhole or other defect that could arise from a dust particle on the surface, non-optimal fabrication lithography, metallic conducting path on the side or other area of the sample. Also the junction resistance should be high enough so the so the voltage drop across the junction can be detected in our system since our current source is limit 100 mA.

A clean Nb film will have a critical current density $J_c$ of $10^6$ to $10^7$ A/cm$^2$ at 4.2 K. Given the wiring layer width of 5 micron and thickness of 100-200 nm, the Nb wiring layer can carry 5-50 mA of critical current.

Since we will be fabricating junction with an insulator barrier using Al, we referred to Miller et al. [61], where it have shown that the critical current of typical Nb/$AlO_x$/Nb junction can be as high as 1000 A/cm$^2$ at 4.2 K (Figure 27). We will use this curve as a guide for our Al tunnel barrier growth and estimate junction resistance.

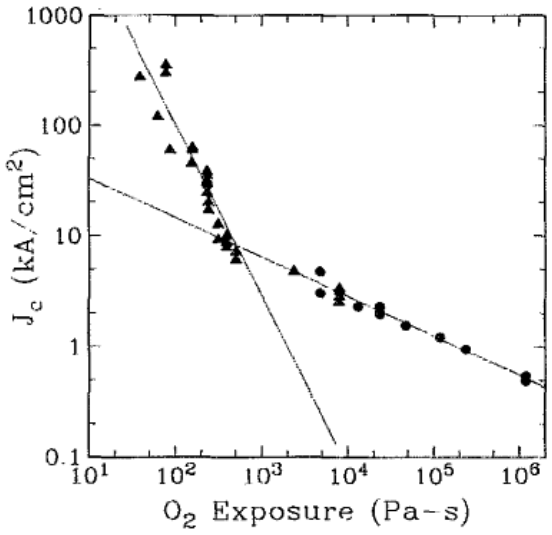


Figure 27. Dependence of $J_c$ on oxygen exposure for oxidation times of 10 min (solid triangles) and 30 min (solid circles) [61]

In our approach in making small size junctions, we had two different methods shadow mask junctions using mechanical masks and micro-fabrication junctions using Cr coated glass masks with lithographic tools. Since the first junction was made in 1963, the junction fabrication process has become more complicated than its initial cross-type junction methods. Currently, a sophisticated multilayer step process using a large number of cleaning, photolithography, deposition and etching steps are used.

. After Nb was chosen as the electrode material, a Selective Nb Anodization Process (SNAP) for fabricating Josephson junctions was first introduced by H. Kroger, et al. in 1981. [62]. In that process, an anodized $Nb_2O_5$ was used for junction area definition. Selective Nb Etching Process (SNEP) was then adopted by M. Gurvitch, et al. in 1982. [63]. In this process, dry etching was used to define the junction area and anodization was also used to form an insulating layer. The anodization process is self-aligned, easy and

convenient. For sidewall protection in our study, materials which are good insulators at low temperature such as $SiO_2$ and Germanium (Ge) were also used. The lift-off of the dielectric was introduced into superconductor device microfabrication by M. Yuda in 1987[64]. In our work, we combined both the Nb anodization and dielectric lift-off methods.

3.2 Shadow mask process

One of the primary reasons for using the shadow mask method is that it is a simple and quick process. Stainless steel shadow masks are used during deposition to define the region of the junctions, and are usually made of stainless steel or tantalum. In our case they were made of stainless steel.

A shadow mask with a 250 μm slit is used to cover the substrate before growth, to define the bottom junction electrode strip. The mask should be in close contact to the substrate using a clip to avoid shadowing. To produce an oxide barrier (i.e. AlOx), the wafer was exposed to oxygen ($O_2$) for a 30 min in the load lock chamber. A top electrode shadow mask with a few parallel slits will be installed at normal angle to the bottom electrode define the top electrode during its deposition. The replacement of masks was done ex-situ in our experiments.

If the barrier oxide is not formed by oxidizing the bottom superconductor electrode itself, and a different normal metal used to act as an oxide, such as Al-$AlO_x$ then the bottom strip's edge needs to be covered with certain insulators (i.e.$SiO_2$, Ge), to prevent the top electrode from shorting through the edge of the bottom electrode. In this case, after the bottom electrode deposition, an additional step of depositing an insulator

for edge-covering will be needed with another wire-shaped mask. This process produces junction in size of 500x300 micron square. The pros and cons of shadow-mask junctions are listed below.

Pros:

1) Fast fabrication of Junctions can be available for measurement after growth.

Cons:

1) Relatively large junction size. It will be difficult to reduce the junction size to less than 50 micron, due to the unavoidable shadow effect..
2) If the mask replacement has to be done ex-situ, then the oxidation of the sample surface will not be controlled. The humidity in air will affect the oxidation, too.
3) When installing/removing shadow masks for growth, the thin film may get scratched or damaged physically by the mask if not done properly.

Schematics of masks used in this process are shown in Figure 28. The final device geometry is shown in Figure 29. This process is used to fabricate S/F/I/N junctions.

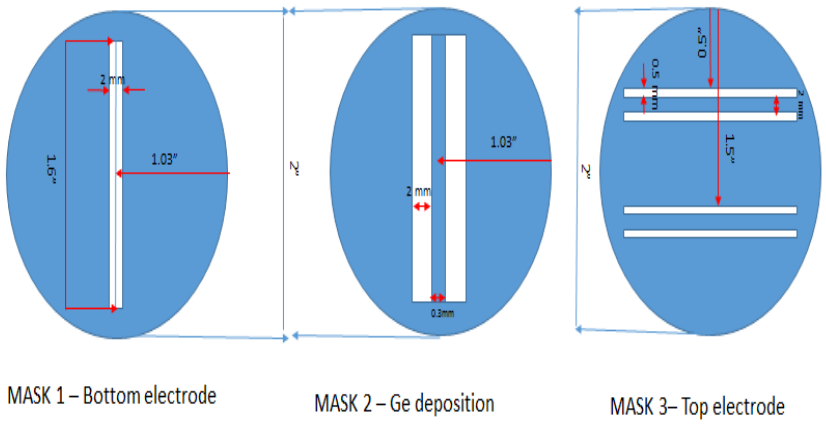


Figure 28. Three mechanical mask set used for the shadow mask process

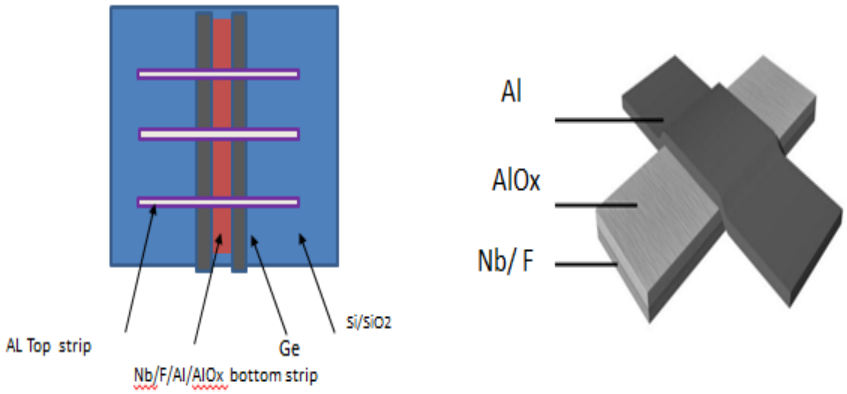


Figure 29. S/F/I/N tunnel junction top view of process device using standard mechanical shadow mask process with Ge for junction definition

3.3 Micro-fabrication method

The micro-fabrication process is comprised of several stages, including photolithography and mask patterning, reactive ion etching, anodization, dielectric and wiring layer sputter deposition, ion milling and wire-bonding. These steps are described below.

### 3.3.1 Photolithography and mask patterning

A photolithographic microfabrication process is used to produce micron size devices. The pattern was transferred from a soda lime mask with opaque chromium pattern to the grown multilayer structures. For microfabrication of Josephson junctions, a 2-step photolithography was developed and used in our group. The mask set used in this process is shown in Figure 30

To perform photolithography, acetone was used to clean the sample surface first and then Hexamethyl disilazane (HMDS) is spin coated on the sample to remove the water vapor and increase the adhesion properties between the multilayer surface and the photo-resist. Then, a 3 micron thick layer of AZ 4330 photoresist is spin coated at 5000 RPM (ramping up from 2000 to 5000 in a few seconds) on the multilayer surface. The sample is subsequently dried on hot plate at 90 °C for 1.5 minutes and then cooled down for 5 min. Then the sample is transferred to a Quintel Q2001 CT mask aligner, where ultraviolet light is used to expose the photoresist. The exposure time is determined previously from test runs. The sample is then rinsed in AZ 300 MIF developer to remove the photoresist on the exposed area which takes around 70-90 seconds then dipped in distilled water (DI) and dried using nitrogen gas.

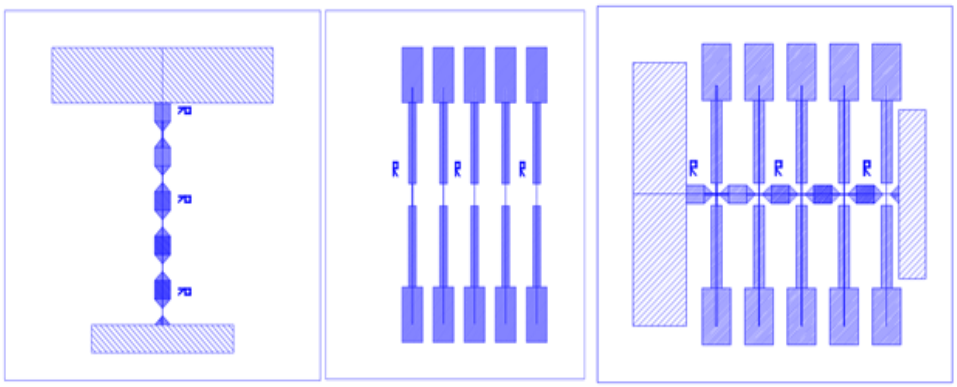


Figure 30. Set of masks used in lithography process

3.3.2 Reactive ion etching (RIE)

Reactive-ion etching (RIE) is used to chemically remove the material deposited in a multilayer structure. A typical parallel plate RIE system consists of a cylindrical vacuum chamber, with a wafer platter situated in the bottom portion of the chamber. The wafer platter is electrically isolated from the rest of the chamber. Plasma is initiated in the system by applying an RF (radio frequency) power to the wafer platter. This oscillating electric field ionizes the gas molecules by stripping them of electrons, creating ion plasma. The ionized etchant gas reacts with the wafer material and forms volatile chemical which are pumped out by a vacuum pump.

In our system, $CF_4$ gas was used in the etcher (PlasmaLab µP, Oxford Instruments) for generating fluorine ion plasma to remove Nb layers by forming volatile $NbF_3$. With 20 sccm $CF_4$ gas, 50 mTorr, 75 W RF power and the etch rate for a clean Nb film is about 10 nm / minute initially and gradually increases to 15-20 nm/minute after extensive etching due to chamber warm up and other physical machismos being active. Since the

photoresist coating is temperature and chemical sensitive, the etch time must be calibrated right with respect to the photoresist lifetime. For AZ 4330 photoresist, the etch time could be as long as 90 minutes with < 100 W etching power. Ar gas is also used to physically etch other barrier material that is not easily etched by the fluorine plasma. Recipes of all etch recipes are presented in table 3.1

Table 3.1 Etch recipes for material used in the multi-layer structures

| Material | Etch gas | Gas Flow(SCCM) | Pressure (mTorr) | Power (Watt) | Etch rate nm/min |
|---|---|---|---|---|---|
| Nb | $CF_4$ | 20 | 50 | 75 | 10 |
| Cu/Al | Ar | 20 | 30 | 100 | 20 |
| NiFe/NiFeCu | Ar | 6 | 20 | 200 | 5 |

3.3.3 Anodization process

The anodization process is used to form an insulation layer to prevent shorting paths between top and bottom electrodes. This method was first introduced by Dr. X. Meng at University of California, Berkeley [65]. The anodized layer is grown by passing a direct current through an electrolytic solution (Boric acid formed with 20% ammonia pentaborate and 80% DI water), with the junction wafer serving as the anode (the positive electrode). The current releases hydrogen at the platinum cathode (the negative electrode) and oxygen at the surface of the anode, creating a build-up of niobium oxide. The niobium surface covered with photoresist will not be anodized. The thickness of the oxide will be determined by the voltage applied by the current source. Our experiments found

that a 20 V bias will produce a ~50 nm thick niobium oxide [65]. The chemical reaction occurring on the two electrodes are indicated below and in Figure 31:

At the anode: $2Nb(s)+5H_2O(l)=Nb_2O_5(s)+10H^++10e^-$

At the cathode: $10H^++10e^- =5H_2(g)$

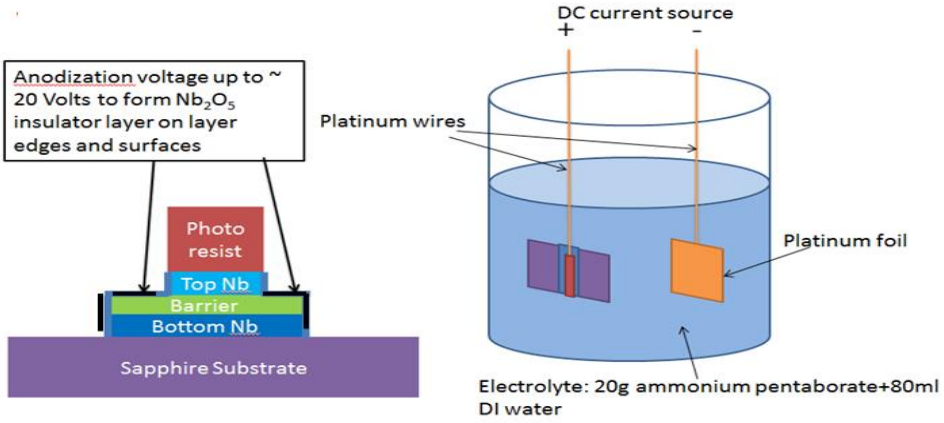


Figure 31. Schematic cartoon of anodization process [66]

3.3.4 SiO2 deposition and lift off process

As shown in Figure 3.6, after anodization is complete, the edge and surface of the barrier are coated with several nanometers thick of oxide. To further improve the insulation between the wiring layers and bottom Nb electrodes, we deposit $SiO_2$ layer by RF sputtering and then used a lift off process to remove it from the desired areas. Without removing photoresist, the sample is loaded into a vacuum chamber where its loaded on a cool substrate holder to prevent from photoresist hardening while sputtering, and inner diffusion between the layers in the device. Due to the slow growth rate (5 nm/ min) of insulating material by RF sputtering, the growth takes 1 to 1.5 hours to for a 200 – 300 nm thick insulation layer. After deposition, the sample was immersed and rinsed in hot

photoresist stripper (around 70 °C) to remove photoresist and thus lift off the $SiO_2$ over the junction area, where it was coated with photoresist during the $SiO_2$ deposition process. Then the sample cleaned with DI water and then loaded back to the vacuum chamber for wiring layer deposition [66]

3.3.5 Ion milling and wiring layer deposition

To remove any resistive oxide on the top niobium electrode surface, we performed an ion mill using a Commonwealth Scientific IBS-600 Argon milling unit with a 4 inch-diameter ion source located 15 cm away from the sample. The milling process is performed in a high-vacuum chamber with a base pressure of less than $2\times10^{-7}$ Torr. The sample is adhered to the water-cooled plate using Kapton tape to minimize heating of the sample. Ar gas is introduced by MFC (mass flow controller) through the back portion of the ion source at a rate of 10 sccm. The Ar gas is ionized and accelerated, bombarding the sample surface and removing atoms from the sample. A small beam current is used (10 to 20 mA) to minimize possible damage to the sample and cross contamination from the stainless steel plate. At these conditions the Nb, milling rate at 10 mA beam current is about 6 nm/ min. After the Ar ion milling, a 300 nm thick Nb wiring layer is sputtered in-situ without breaking vacuum. [66].

3.3.6 Micro-fabrication process flow

To summarize, a $SiO_2$ lift-off process combined with selective Nb anodization is used for cross junction fabrication. Nb/F multi-layer strip structure with size 1 cm × 2 mm Nb-were deposited using a physical shadow mask. This step could also be alternatively done by patterning a strip on the fully deposited wafer and etching to form

the strip. Then the wafer was patterned and etched with $CF_4$ gas using an Oxford Plasmalab 80μP reactive ion etcher, and the thin barrier usually works as an etch stop. After that, without removing the photoresist, a self-aligned anodization was performed on the etched area with 20 V. A Platinum (Pt) plate was as cathode and a Pt wire was used to connect the sample to the anode with silver paint. 200 nm $SiO_2$ was RF sputtered after the anodization process and then lifted off with ultrasonic bath in photoresist stripper (heated on hot plate to 70 °C, AZ 400T Photoresist Stripper). 300nm Nb wiring layer was then deposited by DC sputtering after a brief ion milling surface cleaning. Finally, the Nb wiring layer and the top Nb was patterned and etched to define the top electrode. A series of 50, 20, 10, 5 and 2 μm size of square cross junctions were fabricated as shown in Figure 32 [66].

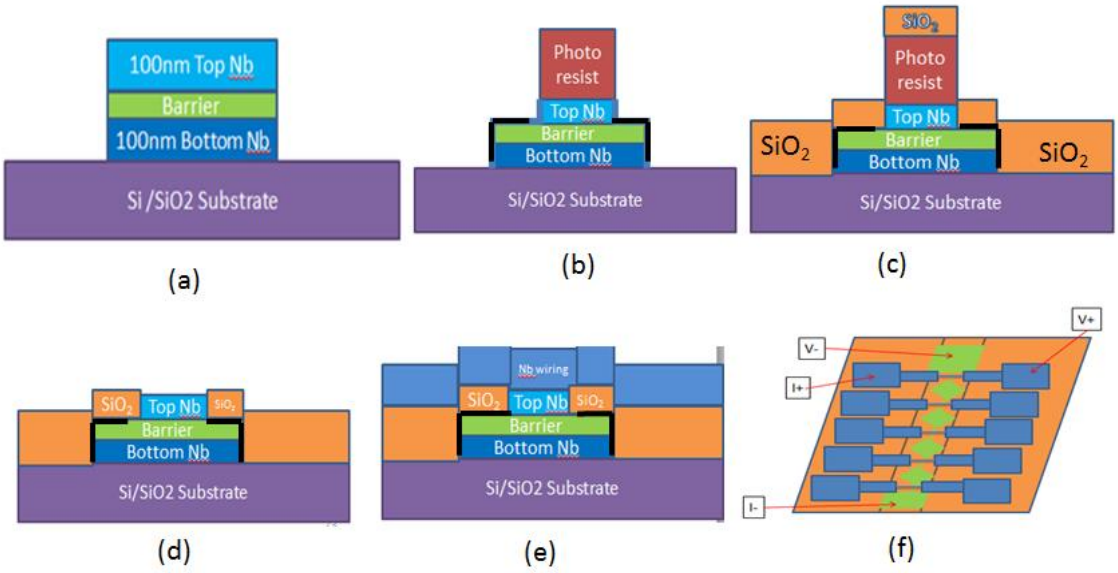


Figure 32. junction fabrication process: (a) Junction tri-layer strip definition; (b) Junction definition etch with anodization ( black lines) (c) SiO2 deposition (d) SiO2 lift off process (e) Ion milling and wiring layer deposition; (f) Second etching to define top electrode and wire bonding

### 3.3.7 Junction wire bonding

Wire bonding is used to connect the fabricated devices to chip carriers after completing the fabrication process. This process is carried out in a controlled humidity environment to avoid any electrostatic discharge damage, and the wire bonding station, chip carrier and the operator are all grounded during this process.

The 1 cm × 1 cm size junction wafer was positioned in a gold-plated ceramic 44-pin chip carrier, designed to be compatible with our electrical cryogenic probe. The wafer was attached to the 44-pin chip carrier with silver paint (SPI, 05001-AB) or photoresist. After the adhesion is cured (5 minutes for silver paint and 30 minutes for photoresist), the

junction contact pads were connected manually to the electrical connection pins of the chip carrier with thin gold wire (31 micron in diameter, California Fine Wire) and silver paint. On the wafer, in order to perform four-point measurement, each junction will require two contacts on the top electrode line and two contacts on the bottom electrode line, and the latter two can be shared with all the other junctions. So for a typical 5-junction wafer, 12 connections will be made. After wire-bonding, the wafers with chip carriers were kept in an anti-static box in the room with ~40% relative humidity awaiting electrical measurements Figure 33.

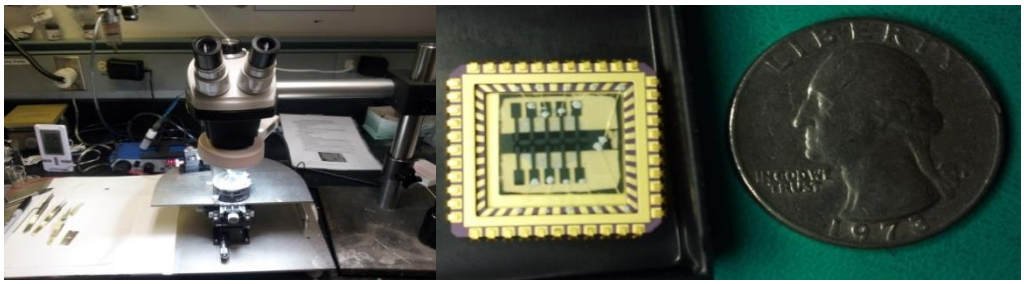

Figure 33. Left -wire bonding station and right- a wire bonded sample mounted on gold platted chip carrier [66]

# CHAPTER 4 STUDY OF $Cu_{1-x}(Ni_{80}Fe_{20})_x$ MAGNETIC SYSTEM

In this chapter we will discuss the motivation behind studying dilute magnetic alloys and the results of our comprehensive investigation of Copper doped NiFe material. We will present our electrical, magnetic and structural data

## 4.1 Introduction and motivation

Copper permalloy alloy films were deposited by co-sputtering and then their chemical, structural and magnetic properties were characterized. By varying the composition, the saturation magnetization ($M_s$) can be tuned from 800 emu/cm$^3$ to 0 and the Curie temperature ($T_c$), can be adjusted from 800 K to 0. $M_s$ and $T_c$ are found to scale linearly between $x = 25\%$ and 100%. These films also have relatively low electrical resisitivity. $Cu_{1-x}(Ni_{80}Fe_{20})_x$ alloys appear to be attractive weak ferromagnetic materials for use in low temperature magnetoelectronic applications. We outline the physical mechanisms that result in the magnetic properties of the materials in the dilute limit.

The use of doping and alloying of magnetic materials is a versatile way to engineer the properties of magnets for practical applications. Beginning in the 1930s many advances were made in systematic studies of a wide range of dopants and alloying agents, led by Elmen, Bozarth and others in the Bell Labs group [67, 68] Their quest led to metallic magnets with high permabilities and low A.C. loss for transformers and loading coils, large remanent magnetizations for permanent magnets, and oxide ferrites and garnets for high frequency applications. In all these cases, the materials are comprised largely of "magnetic" elements, e.g. Co, Ni, Fe, Cr, and Mn, and are classified as "strong" since they exhibit characteristically large saturation magnetization values (or equivalently high permeabilities) at room temperature. The use of magnets at low

temperatures for practical applications is limited to date, and when they are used, strong magnets are also almost always chosen because of their high saturation magnetization ($M_s$).

The exploration of dilute levels of the magnetic elements in non-magnetic hosts has not been extensively explored for practical applications because magnetic ordering is only observed at low temperatures and the magnetism is weak. Most previous work on dilute magnetic systems has been done primarily by the academic community in areas such as spin glasses [69]. General mechanisms for the behavior of dilute magnets often involve percolation theory. [70, 71, 72]

Besides the questions associated with the fundamental issues and properties of dilute magnets, there has been a growing need for weak magnets with low saturation magnetization and possibly reduced Curie temperature for some microelectronic applications. To reduce the switching fields of spin-toggle MRAM, the use of weaker magnets operating at lower temperatures is a viable alternative. Since the thermal stability barrier of a bit scales as $M_s^2 \Delta t^2 \propto k_B T$ [73,74] ($\Delta t$ is the layer thickness, and T is the temperature ), and the minimum write current that generates the switching field scales as $M_s \Delta t$, a reduction from 300 to 4 K would allow a factor of $\sqrt{300/4} \approx 8.6$ in in the write field and current. For spin-torque MRAM devices, the write current ($I_c$) scales roughly proportional to $M_s^2$ [73]. Such a reduction is particularly important as the main obstacle to wide-spread commercialization of these devices is the unreliability of the tunnel barriers when exposed to such large write current densities.

Another microelectronic application of interest is the development of a fast, dense, low-power cryogenic memory using Cooper pair transport though ferromagnetic free and fixed layers clad by superconducting electrodes. [75, 76, 77] To realize energy savings in these devices, it is imperative that the free layer reduce its switching energy. While the read process consumes insignificant energy levels because it involves detecting the zero-voltage superconducting current magnitude, the energy of the write cycle can be reduced using a low $M_s$ free layer since this process is identical to the write cycle of MRAM [75,76, 77].

In the work described in the this manuscript, we show that by diluting magnetic elements with non-magnetic hosts the properties such as the saturation magnetization and Curie temperature can be tuned over a wide range of values, including to desired small values.

We specifically study copper-permalloy ($Cu_{1-x}(Ni_{80}Fe_{20})_x$) alloys in the magnetically dilute limit, where $M_s$ can be tuned from 800 emu/cm$^3$ to 0 and the $T_c$ can be adjusted from 800 K to 0 by varying the alloy composition. From previous work [78] $Cu_{1-x}(Ni_{80}Fe_{20})_x$) alloys can be found in 3 different phases (Iron rich phase, an Iron and Copper rich phase and a Copper rich phase) as shown in Figure 34. These phases are a contributor to the electrical and magnetic properties changes. .Studies of the structural and chemical properties of this alloy system, summarized in the phase diagram, has determined that the Cu- Permalloy system is miscible over a wide range of compositions [79]. Copper-permalloy alloys were explored previously while investigating the magnetization dynamics for ultrafast magnetic information storage [80]. However, to our

knowledge, the magnetic and electronic properties have not been explored extensively, particularly in the dilute limit of permalloy content.

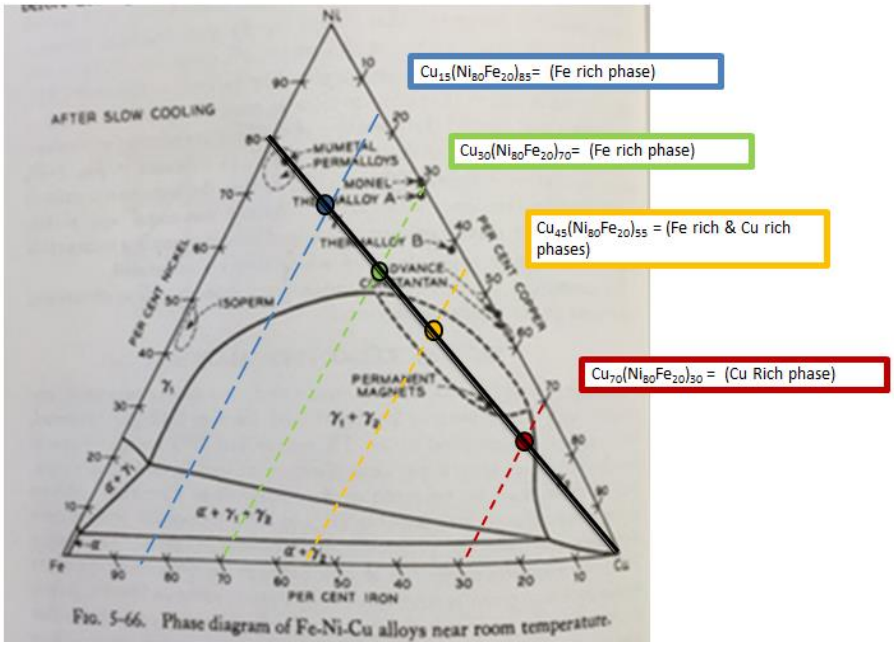


Figure 34. Phase diagram of FeNiCu alloys near room temperature [78]

4.2 Sample preparation and experimental methods

Cu-permalloy films used for this study were deposited on to oxidized Si (100) wafer at room temperature using co-sputtering in an unbaked UHV chamber with a base pressure of ~$2\times10^{-8}$ Torr. A 5 cm US Inc. and a 2.5 cm Kurt Lesker Torus™ magnetron sputter sources were used with 99.95% pure $Ni_{81}Fe_{19}$ (81% Ni, and 19% Fe) and Cu targets respectively. The $Ni_{81}Fe_{19}$ source sputters head-on to the substrate and the Cu source was mounted at ~$45^{o}$ angle. The films were sputtered under an Ar pressure of 10 mT (at 50 sccm). The power of the Cu and $Ni_{81}Fe_{19}$ sources were varied from 2 to 200 W

to controllably adjust the Cu content of the deposited films. These conditions and this target composition are known to produce $Ni_{80}Fe_{20}$ permalloy films. Using this technique, the entire spectrum range of alloy composition $Cu_{1-x}(Ni_{80}Fe_{20})_x$ ( $0 < x \leq 1$) was achieved.. All samples were coated with an Aluminum (Al) top layer to prevent films from oxidation. Sample structure is shown in Figure 35. Rutherford backscattered spectrometry (RBS) was used to infer Cu content and the thickness of the thin films. Since the involved elements (Cu, Ni, and Fe) have similar atomic weights, reducing the accuracy of the RBS analysis, the composition was further verified by particle induced X-ray emission spectroscopy (PIXE) for a number of films. We found the composition uncertainly, $\Delta x$, across a 1 cm × 1cm area is <5%.

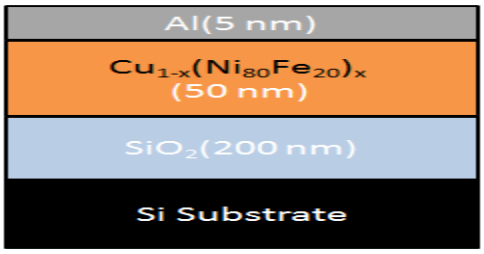


Figure 35. Sample structure of grown 50 nm $Cu_{1-x}(Ni_{80}Fe_{20})_x$) alloys with different compositions

The magnetic properties, temperature dependent magnetization and magnetization-applied field (M-H) isotherm curves, of the films were characterized using a vibrating sample magnetometer (VSM) from 2-1000 K (Quantum Design, Model PPMS with oven option). X-ray diffraction (PANalytical X'Pert PRO) was used for structural analysis. (We are not showing any of these results). The temperature dependent electrical resistivities of the films were measured using an inline 4-point dipping probe inserted into a liquid He Dewar. The surface quality and roughness of the thin films were obtained

from topography measurements using a commercial atomic force microscope (AFM) (Veeco, Model Dimension 300).

Table 4.1 RMS roughness of few $Cu_{1-x}(Ni_{80}Fe_{20})_x$ films as measured by AFM

| **Permalloy content (%)** | **Thickness (nm)** | **RMS roughness (nm)** |
|---|---|---|
| 60 | 72 | 1.4 |
| 30 | 83 | 1 |
| 12 | 115 | 1.8 |

Electronic structure simulations were performed using the Coherent Potential Approximation (CPA) with Linear Muffin Tin Orbital (LMTO) density function methods made available through the LM Suite (http://www.lmsuite.org). These codes use the method of linear muffin-tin orbitals (LMTOs) formulated by O. K. Andersen using the full-potential implementation in this package. The envelope functions (basis) are convolutions of Gaussian and Hankel functions.

## 4.3Results and discussion

### 4.3.1 Structural results

RMS roughness and thickness of few $Cu_{1-x}(Ni_{80}Fe_{20})_x$ compositions are summarized in Table I. The 1-2 nm rms surface roughness values indicate that the topography of the film does not vary much with composition and it should be adequate for thin-film magnetoelectronic applications. Figure 36 shows RBS data for $Cu_{70}(Ni_{80}Fe_{20})_{30}$

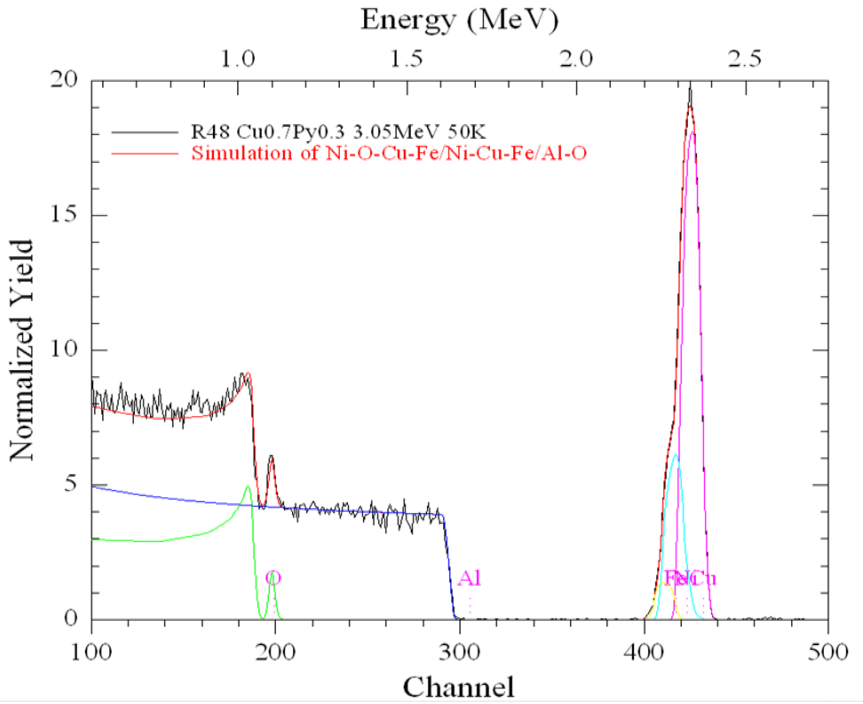


Figure 36. RBS scan for $Cu_{70}(Ni_{80}Fe_{20})_{30}$

4.3.2 Magnetic characterization

Figure 37 shows the typical M-H behavior of co-sputtered $Cu_{1-x}(Ni_{80}Fe_{20})_x$ alloy films at room temperature (RT) and 4.2 K. This particular sample has 50% permalloy content and measured Curie temperature of 380 K. Compared with RT data, $Cu_{1-x}(Ni_{80}Fe_{20})_x$ at 4.2 K has much higher $M_s$, and Coercive field, $H_c$, for all compositions of film studied. The "rounded-off" transition of magnetization form $M_s$ to $-M_s$ indicate that the transition is dominated by domain-wall motion in the samples.

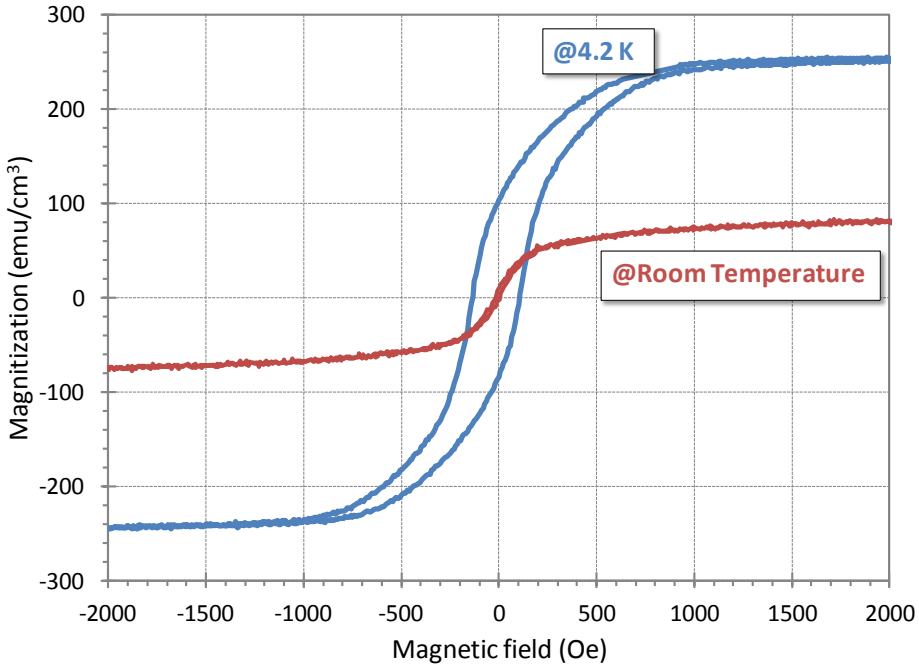


Figure 37. Typical M-H behavior of co-sputtered Cu-permaloy alloy. This particular sample has 50% permalloy content and a Curie temperature of 380 K

Temperature-dependent saturation magnetizations of few $Cu_{1-x}(Ni_{80}Fe_{20})_x$ alloys are shown in Figure 38. The data was measured under an applied field of 2500 Oe, large enough to reach saturation at all temperatures for all samples in this study. For $x = 0.75$, the temperature-dependent saturation magnetization can be fit to a Brillouin function [81], which is typical of strong ferromagnetic materials like permalloy. In this case, it is possible to extract the Curie temperature values from fitting the $M_s$-T curves. However it is not the case for $x = 0.35$ and $x = 0.25$, as the $M_s$-T dependence deviates from the Brillouin function, likely due to the influence of the relatively large applied magnetic

field compared to the relatively weak internal field of the material. Other materials with similarly small exchange energies and saturation magnetic fields behave similarly.

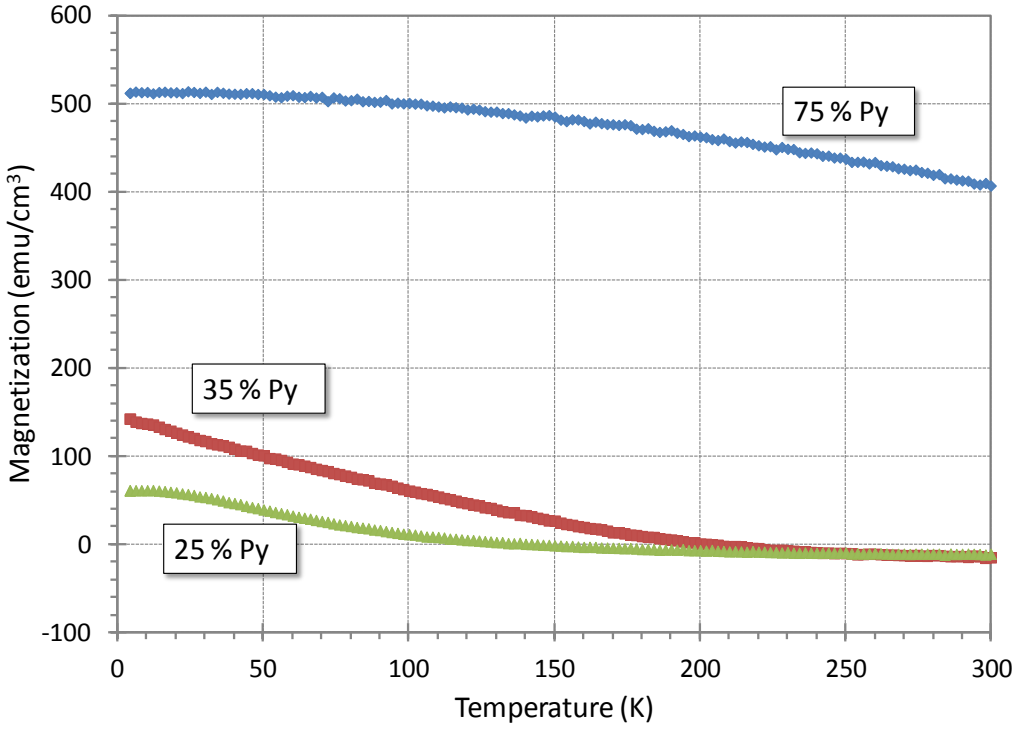


Figure 38. Temperature-dependent magnetization of Cu-permalloy alloy measured at 2500 Oe.

In order to avoid the large inaccuracies in such an analysis for weak magnets, we used Arrott analysis [82] to determine the Curie temperatures in this study. As illustrated in Figure 39, low field $M^3$ (where M is the magnetization) vs H curves at various temperature was plotted. For temperature above $T_c$, the shape of $M^3$ vs. H is concave down, and for temperatures below $T_c$, the shape of $M^3$ vs. H is concave up. At $T_c$, $M^3$ vs. H is linear. As shown in Figure 3, using this method we can determine the $T_c$ within a few degrees.

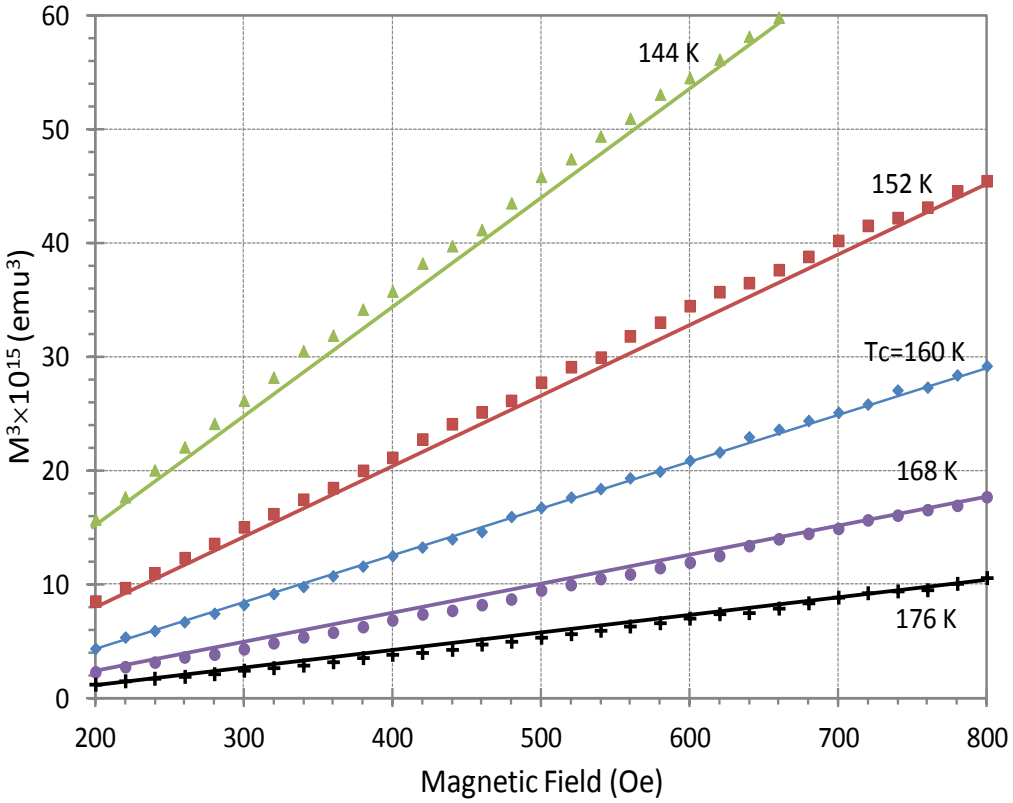


Figure 39. Arrott analysis [82] was used to determine the Curie temperature ($T_c$) of $Cu_{1-x}(Ni_{80}Fe_{20})_x$) alloys. For temperatures above $T_c$, the shape of $M^3$ vs. H is concave down, and for temperatures below $T_c$, the shape of $M^3$ vs. H is concave up. At $T_c$, $M^3$ vs. H is linear. The data plotted here came from a sample that contains 35 % permalloy

Figure 40 summarizes the Curie temperature, saturation magnetization at 4.2 K, and coercive field ($H_c$) as function of permalloy content of co-sputtered $Cu_{1-x}(Ni_{80}Fe_{20})_x$ films. For the films studied, $H_c$ is in the range of 120-150 Oe. In these types of alloys $H_c$ is largely determined by domain wall motion and pinning which is extrinsic and influenced primarily by defects, such as grain boundary, dislocation, structural relaxation effects,

chemical clustering, thickness variation/surface irregularities, as well as exchange interaction or local anisotropy fluctuations[83].

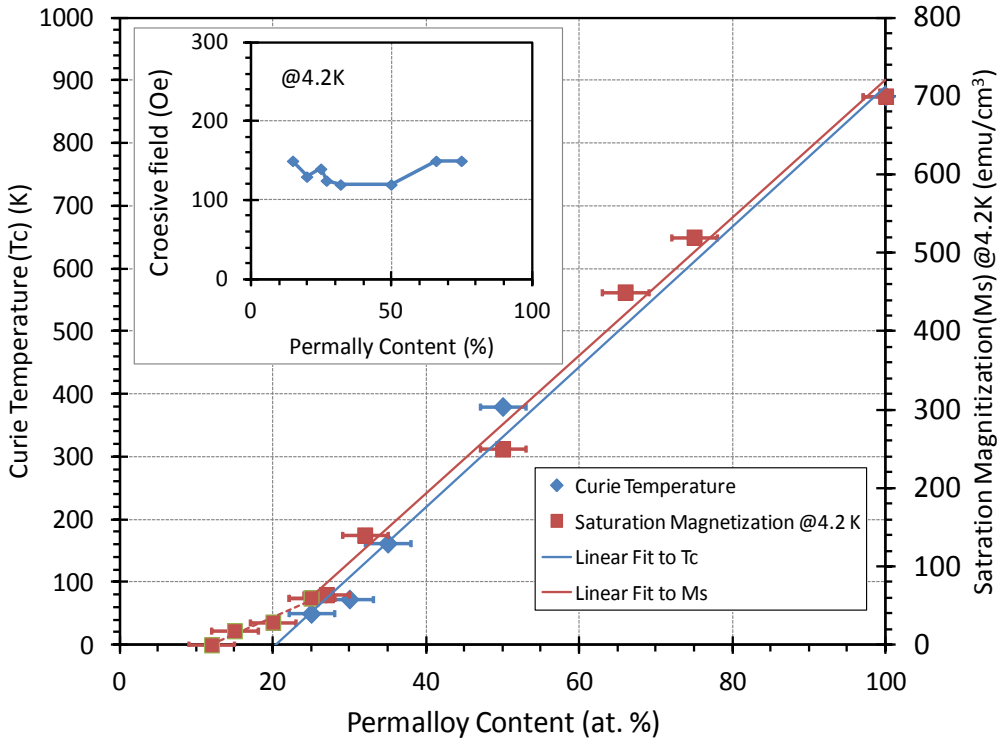


Figure 40. Curie temperature ($T_c$), saturation magnetization ($M_s$) at 4.2 K, and coercive field ($H_c$) dependencies on permalloy content of co-sputtered $Cu_{1-x}(Ni_{80}Fe_{20})_x$ films

For permalloy content greater than 25%, $T_c$ and $M_s$ scales rather linearly (Figure 40). For permalloy content below 25%, we were no longer able to extract reliable $T_c$ values form Arrott analysis due to the small magnetization and significant noise. Between 12% and 25% permalloy content, $M_s$ values scale with a reduced slope as shown in Figure 39

Figure 41 (top) shows the magnetization measured in 5 kOe applied filed as a function of temperature for two dilute permalloy alloys $Cu_{70}(Ni_{80}Fe_{20})_{30}$ and $Cu_{85}(Ni_{80}Fe_{20})_{15}$. Figure 41 (bottom) shows the magnetization versus applied field graphs

(M-H loops) measured on the same thin films. Measurements of the $Cu_{70}(Ni_{80}Fe_{20})_{30}$ sample show the characteristics of a ferromagnet with open hysteretic loops and the corresponding large squareness ($M_{sauration}/M_{remanence}$), remanent magnetization, and coercivety. The 100 K M-H loop shows evidence for the presence of a small amount of a superparamagnetic component due to the lower squareness and higher field required for saturation. Even a field of 5 kOe does not saturate the magnetization.

In contrast, the M-H loops for the $Cu_{85}(Ni_{80}Fe_{20})_{15}$ exhibit "slanted S" shape, essentially closed hysteretic loops and small squareness ($M_{sauration}/M_{remanence}$), remanent magnetization, and coercivety indicate that the film with this composition is predominantly superparamagnetic. These s-shaped loops that were observed in this region are generally consistent with the Langevin function used to describe the magnetization of superparamagnetic clusters [84]. The finite coercive field ($H_c$) at 2 K for the $Cu_{85}(Ni_{80}Fe_{20})_{15}$ film indicates that there is evidence of some ferromagnetic exchange coupling present in this inhomogeneous film.

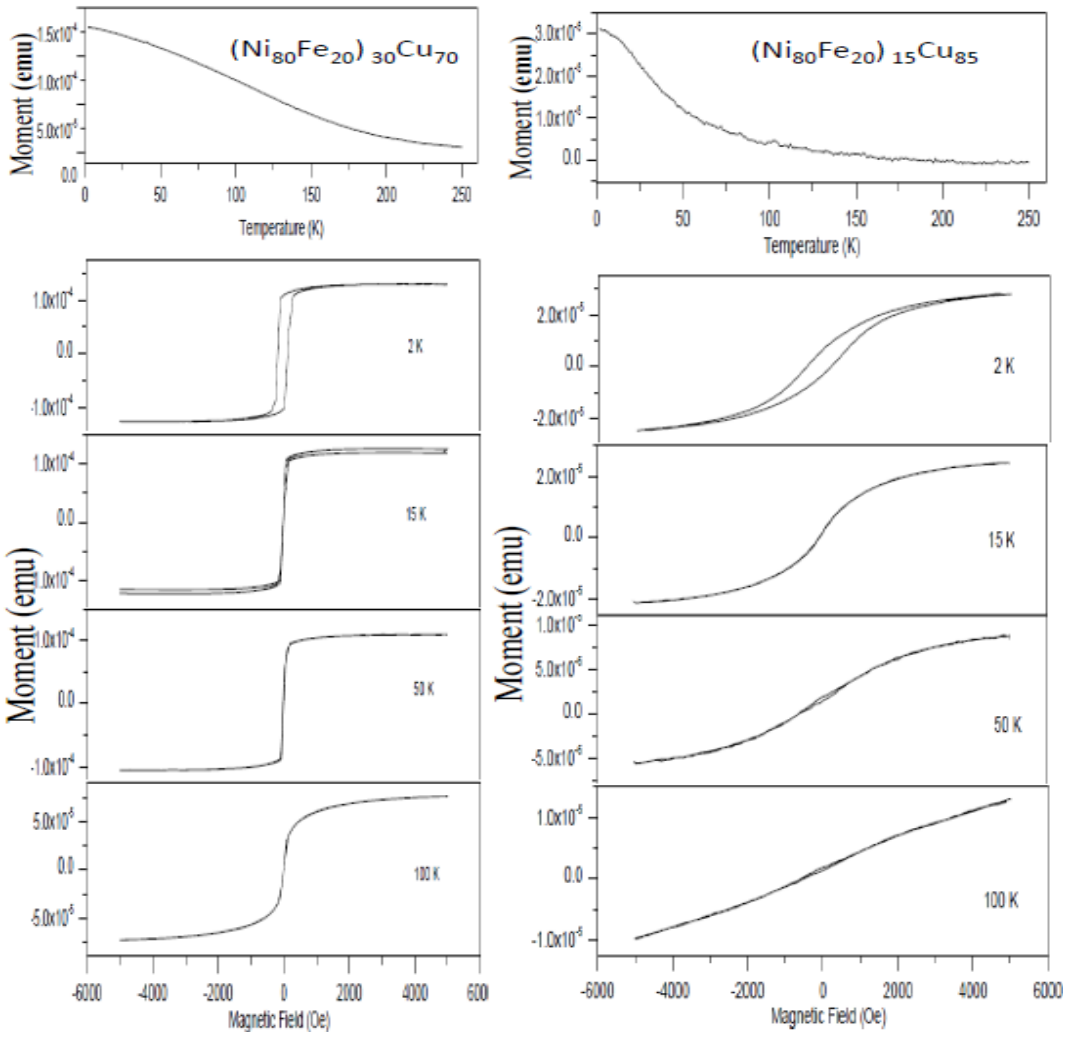


Figure 41. Top) Magnetization versus temperatures for 50 nm-thick $Cu_{70}(Ni_{80}Fe_{20})_{30}$ (left) and $Cu_{85}(Ni_{80}Fe_{20})_{15}$ (right) Thin-films measured at a constant applied field of 5 kOe. (Bottom) The correspondence magnetization versus applied field for the same for 50 nm-thick $Cu_{70}(Ni_{80}Fe_{20})_{30}$ (left) and $Cu_{85}(Ni_{80}Fe_{20})_{15}$ (right) thin-films.

This linear dependence of $T_c$ and $M_s$ on permalloy content is similar to the behavior found by models with nearest-neighbor interactions as a function of dilution [71]. Specifically, in the Ising model, binary (+/-) spins are randomly placed on a crystalline lattice. When only the exchange interaction among nearest neighbors is considered, a

linear scaling of $M_s$ and $T_c$ is observed. Furthermore, this diluted Ising model predicts that ferromagnetic order disappears below a critical concentration of two magnetic nearest-neighbors per magnetic site, corresponding to a permalloy concentration of ~17% for the FCC lattice, in quantitative agreement with the critical concentration shown in Figure 40. Although the agreement may be somewhat fortuitous, especially given dynamical effects and the shape of the curvature as the critical concentration is approached, we believe that it gives insight into the physical nature of ferromagnetism in diluted magnetic materials. A more-realistic model would include changes in the nearest-neighbor interactions when the number of neighbors is reduced, and the influence of next-nearest-neighbor interactions. Thus, it is desirable that electronic structure band structure calculations be performed on this system, although we realize the computational expense in addressing dilute and disordered alloy configurations.

Simple models with fixed nearest-neighbor interactions are expected to be a reasonable approximation when the number of unpaired electron at each Ni and Fe atom remains relatively constant as Cu content increases. Chien et al show that this is found for the case for Cu-Fe system [85], although it would be surprising for the Cu-Fe-Ni systems. Strong hybridization and shifts in the *d*-electron levels for such system, as is well known for the color changes when Au is alloyed with Ga, Ni and many other elements. Some of these compositions are labeled “white gold”.

The observed linear relationship between Cu content, $T_{curie}$ and $M_s$ is not found for other diluted permalloy systems. For example, we found in Mo doped permalloy made with similar method, at 14% Mo (86% $Ni_{80}Fe_{20}$) content, $M_s$ dropped by ~25%, from

~800 to 600 emu/cm$^3$, while $T_{curie}$ has already dropped by almost a factor of 270% from ~870 to 325 K.

4.3.3 Electrical characterization

The $Cu_{1-x}(Ni_{80}Fe_{20})_x$ resistivity at room temperature and 4.2 K are summarized in Figure 42 (Top) along with the RRR ratios summarized in Figure 42 (Bottom). The resistivity reaches a peak near $x = 50\%$ in our data, a signature for alloy scattering. This is very distinct from Cu-Ni alloys. In the Cu-Ni system it has been well established both theoretically and experimentally that the resistivity peaks at the content for ferromagnetic transition, 45% Cu [86, 87, and 88]. The Kondo effect, a signature of magnetic scattering, has been observed both below and above the ferromagnetic transition. We have not observed clear evidence of a Kondo minimum in the temperature dependent resistivity of any $Cu_{1-x}(Ni_{80}Fe_{20})_x$ films that were measured. Also in the $Cu_{1-x}(Ni_{80}Fe_{20})_x$ system, the resistivity reaches a maximum value at around $x = 50\%$ and the ferromagnetic transition occurred between 12% and 25%. This, along with the relatively low resistivity compared to other metal-permalloy system, suggests that magnetic scattering is not the dominating transport mechanism in our film.

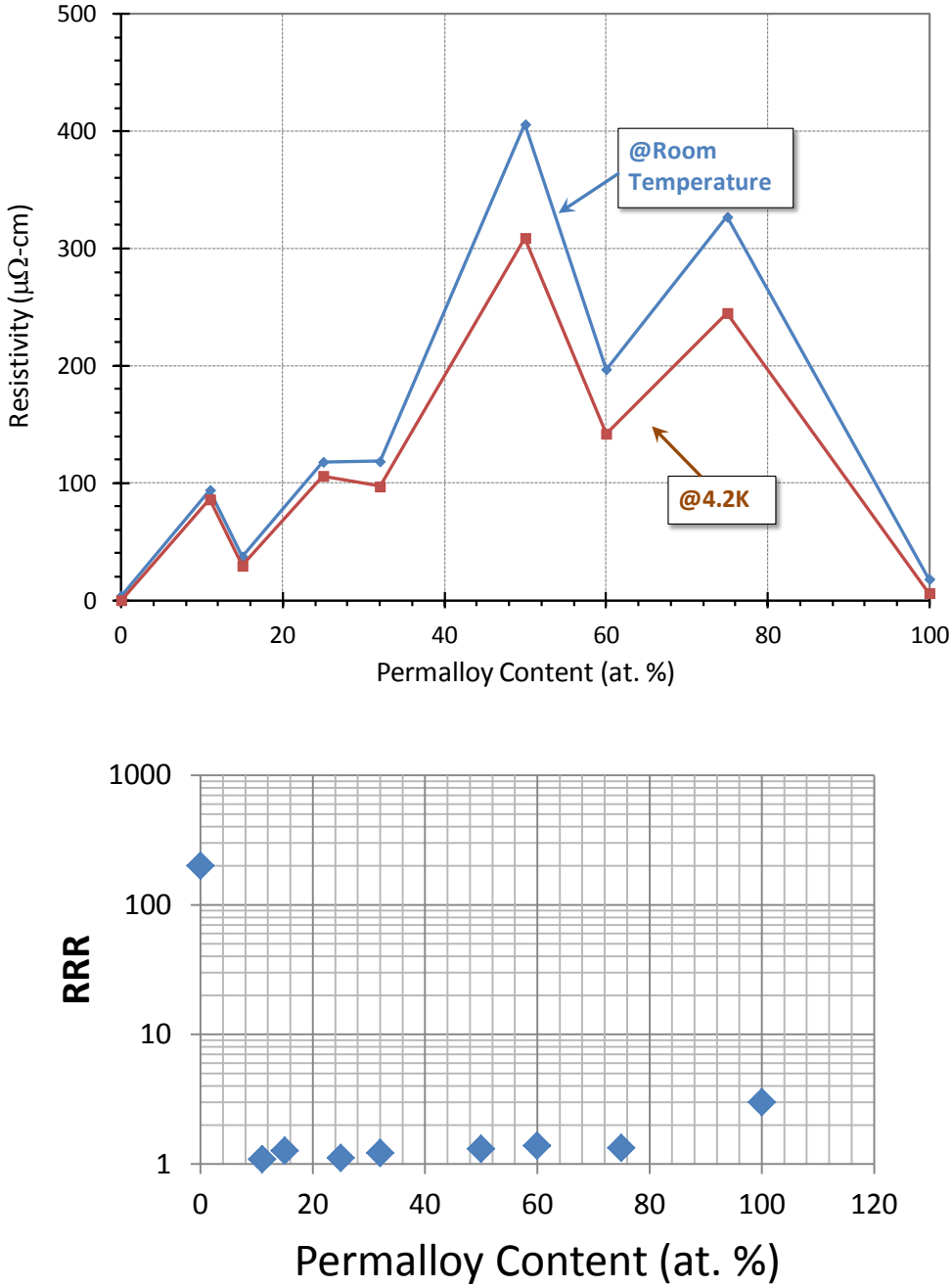


Figure 42. (Top) Room temperature and 4.2 K resistivity of Cu-permaloy films as permalloy content vary (Bottom) RRR of Cu-permaloy films as permalloy content vary

4.3.4 Electronic band structure calculation

Electronic band structure calculations were done by our colleague Prof.Van Schlifgaarde at Kings college, London, using the coherent potential approximation indicate that alloying with copper does not significant change the general shape of the bands (Figure 43). In pure permalloy, the width of the bands at the Fermi, indicative of strong alloy scattering, is found to be very small for the majority carriers, but much larger for the minority channel. The very small amount of scattering of the majority carriers explains the small resistivity of permalloy material. It does indicate that the minority carriers at the Fermi level are much more strongly scattered, which has important implications for spintronic devices, as well as the recently realized Josepshon-MRAM devices [75, 76, 77]. Alloying permalloy with copper results in very large increases in the alloy scattering for both the minority and majority carriers, particularly for large copper content. This can explain the much higher resistivity of Cu-permalloy alloys than pure permalloy because of the significantly larger scattering of the majority spin channel. We do, however, observe that copper permalloy alloys are still lower than the rest of other metal-permalloy alloys. The mean field energy for different NiFeCu alloys is summarized in Table 4.2 .The energy describes the energy at the atomic sites and gives that coupling strength between that site and all its neighbors.

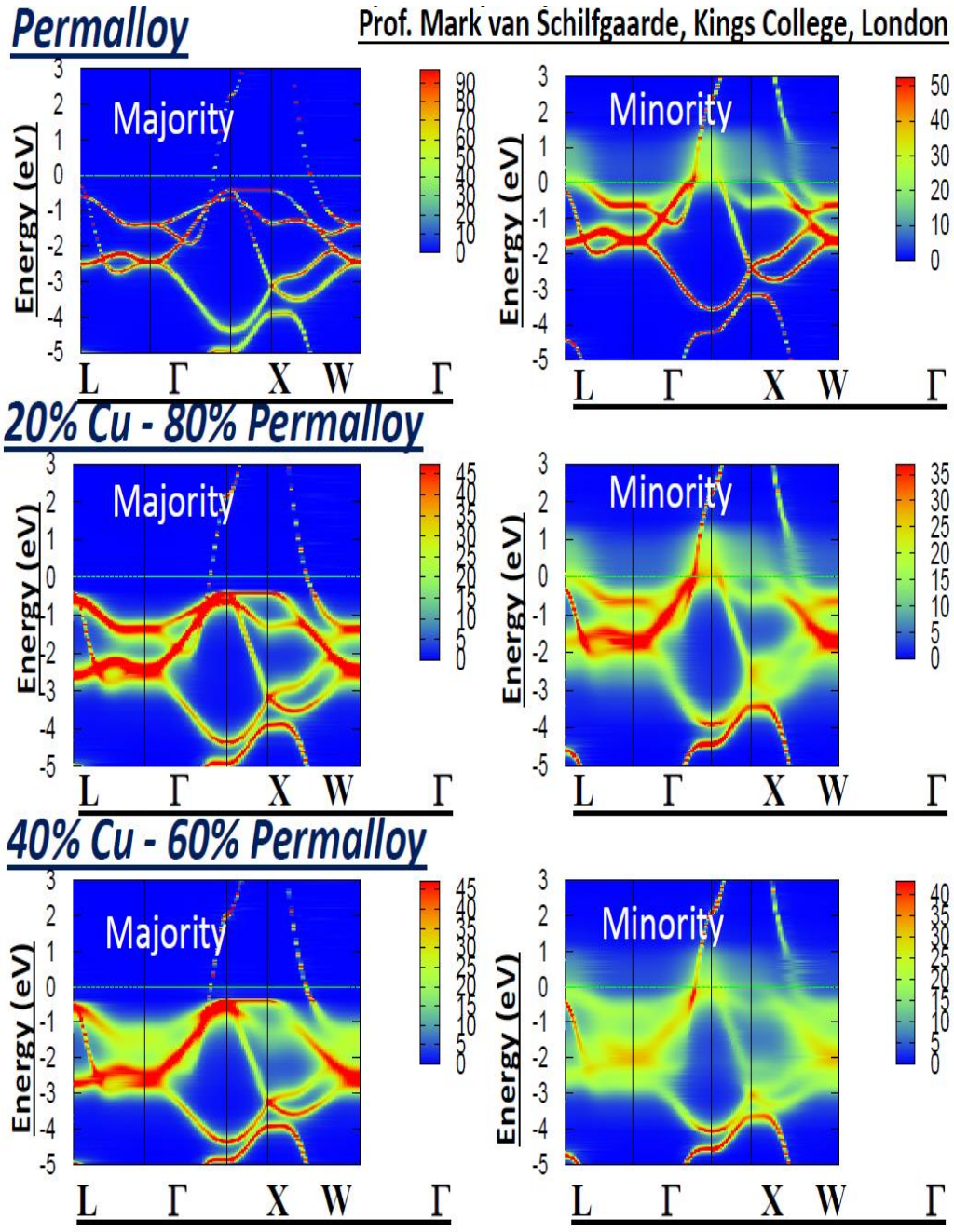


Figure 43 Electronic band structure calculations using the coherent potential approximation for various NiFeCu alloys

Table 4.2 Jo is effective (mean field) exchange field on the atomic sites and give the coupling strength between that site and all its neighbors

| Alloy | M (exp) | M (CPA local moment) | $J_o$ (Fe) mean field | $J_o$ (Ni) mean field | $J_o$ (Cu) mean field |
|---|---|---|---|---|---|
| $Ni_{99}Fe_1$ | - | 0.62 | 12.40 | 3.41 | - |
| $Ni_{80}Fe_{20}$ | 0.85 | 1.00 | 11.30 | 3.94 | - |
| $(Ni_{80}Fe_{20})_{80}Cu_{20}$ | 0.63 | 0.76 | 8.69 | 2.68 | 0.17 |
| $(Ni_{80}Fe_{20})_{60}Cu_{40}$ | 0.44 | 0.55 | 7.01 | 2.01 | 0.10 |

4.4 Summary

To summarize, the magnetic, chemical and electrical properties of $Cu_{1-x}(Ni_{80}Fe_{20})_x$ thin films were measured. $Cu_{1-x}(Ni_{80}Fe_{20})_x$ alloys with x greater than 25 % are found to be ferromagnetic. $M_s$ and $T_c$ of these materials are found to scale linearly with permalloy content. Alloys with x between 12% and 25% are found to exhibit superparamagnetic behavior. Copper-permalloy alloys are found to have a much higher resistivity than permalloy because of the significantly larger scattering of the majority spin channel. From these observations, we can conclude that $Cu_{1-x}(Ni_{80}Fe_{20})_x$ alloys appear to be attractive weak ferromagnetic materials for use in low temperature magnetoelectronic applications. We will use one of the proposed compositions as the soft layer (low energy switching) in our development of the JMRAM memory cell to be fabricated and studies in the next chapter.

# CHAPTER 5 CHARACTERISTICS OF JOSEPHSON JUNCTIONS WITH FERROMAGNETIC BARRIER MATERIALS

## 5.1 Introduction

In this chapter we will discuss the development of the Josephson magnetic random access memory (JMRAM) cell. As discussed in section 1.6 we will outline the physics behind the integration of magnetic barrier materials in Josephson junctions and how through proximity effect discussed in 1.4.2 and 1.5.3 the state of the junction can be manipulated to induce a logic state.

In recent year's incremental progress were made in the development of memory elements that are based on the manipulation of the spin orientation of a stack composed of magnetic materials sandwiched in spin valve geometries. These memories are called magnetic random access memory (MRAM) [89]. These successful developments with the long studied superconductor based devices and superconductor ferromagnetic proximity have promoted intensive attention to the development of a cryogenic superconducting memory based on the existing mature MRAM technology.

Combining the superconducting Josephson junctions and spintronic effects like in MRAM, into low-power devices that are switchable between different logic states could give a chance for high-performance computing and elevate superconducting digital technology [90] as a serious alternative to existing power-consumers computers based on silicon (Si) technology.

Utilizing a Josephson junction (JJ) to store information by altering its state is a possible approach to fabricating a cryogenic memory that is both scalable and practical. Integrating magnetic layers within the barrier of a JJ so that the magnetic state of the

material alters the superconducting critical current that separates zero and nonzero voltage states is an approach that was developed early on [91,92]. Clinton *et al*.[93] demonstrated a micro-bridge device that switches between two different states of the critical current in the junction using the stray field of the inserted ferromagnetic layer. Later, by incorporating a single ferromagnetic layer into a junction barrier [10], the critical current was switched. In both junctions the difference in the critical current of the two states, or the signal contrast, originated from the magnitude and direction of the remnant magnetic field within the junction barrier. These materials had significant ferromagnetic moment and required high switching energies at submicron junction dimensions, which limit them only low density application.

In a different approach, a junction was made that is similar to the MRAM device using a pseudo-spin-valve (PSV) with two different ferromagnetic layers separated by a nonmagnetic normal metal. In MRAM devices, the device resistance is changed using the giant magnetoresistance (GMR) effect by altering the orientation of the magnetization of one layer with respect to the other layer [94]. Writing information to the cell [i.e., switching the barrier multilayer (PSV) state between the parallel (P) and anti-parallel (AP) magnetizations] can be done either by applying a magnetic field or a bias current to switch the magnetization of the free layer [95, 96]

Several groups have reported the use of superconductor/ferromagnetic Josephson junction structures with magnetically-controlled electrical properties. Bell et al. showed that in SFNF'S structures [where S-superconductor, F-ferromagnet, N-normal metal], the current can be controlled by changing the relative orientation of the ferromagnetic

$Ni_{80}Fe_{20}$ and Co layers.[97] This relative orientation of the ferromagnetic devices effectively uses the ferromagnetic layers to shift the superconductor phase through the junction, allowing control of the critical current depending on whether they shift it in the same or opposing directions Their results are shown in Figure 44. Larkin et al. fabricated SISFS structures that use a circuit current to break the symmetry of the single ferromagnetic PdFe layer to produce a memory device that depends on the magnetic orientation of this layer [10]. Lastly, Baek et al. recently fabricated SFNF'S structures which were engineered to shift the superconductor phase across the junction to either a 0 or π state, depending on the relative orientation of the magnetic fields. Relatively large magnetic fields of over 30 Oe were needed to switch the junctions.[76] Such junctions can be used with a conventional Josephson junction in a SQUID loop to produce a large/small critical current when in the 0/π state. Other circuit renditions are possible that can serve as memories, as described in the JMRAM (junction magnetic random access memory) patent of Herr et al. [13]. In JMRAM the state of a bit is recorded using the magneto-current states of a structure comprising a switchable free ferromagnetic layer and a fixed ferromagnetic layer. This approach encodes and stores information in the parallel or anti-parallel alignment of magnetic layers in the device, and reads out the information by measuring the modulation of the device's Josephson critical current. This implementation has all the advantages of conventional MRAM but with much lower energy read cycles, smaller write currents and non-dissipative interconnects.

Here, our goal is to produce SFNF'S devices which could be used to produce a memory with minimal power requirements. The write process dominates the energy

usage and is optimized by reducing the switching field. To minimize the switching energy while still maintaining adequate thermal bit stability at 4.2 K, we will use a dilute Cu-permalloy alloy [$Cu_{0.7}(Ni_{80}Fe_{20})_{0.3}$] with low saturation magnetizations ($M_s$~80 emu/$cm^3$), for the free layer as discussed in chapter 4. We also fabricated a series of Nb/permalloy/Nb junctions that show the optimal thickness of the ferromagnetic permalloy fixed layer is 2.4 nm, as it shifts the wavefunction to the $\pi/2$ pivot point. The working of these devices S/F/N/F'/S will be based on the description of S/F proximity described above. In these structures S/F/N/F'/S, where F and F' may be different ferromagnetic materials.

The pair order parameter function describing Cooper pairs from the left-hand S accumulates a phase $\phi_1=Q_1d_F$ while traversing through F, where $d_F$ is the thickness of the first F layer. If the magnetization of F' is parallel to that of F, then the pair correlation function will accumulate an additional phase $\phi_2=Q_2d_{F'}$ when it transverses through F'. If the role of majority and minority bands is reversed, the pair correlation function will acquire a change in phase of the opposite sign, i.e. $-\phi_2$. As shown schematically in Figure 45 , if we choose $\phi_1$ to be close to $\pi/2$ and_$\phi_2\leq\pi/2$, then when the layers are parallel $\phi=\phi_p=\phi_{1+}\phi_2$, putting the junction into the $\pi$-state, and when the layers are antiparallel $\phi=\phi_{AP}=\phi_{1-}\phi_2$ , putting the junction into the 0-state [98].

In the next section we will show the work of fabricating and characterizing Josephson junctions with first F layer (F= $Ni_{80}Fe_{20}$). This work was carried out to experimentally determine at what thickness permalloy can rotate the superconductor order parameter by

$\pi/2$. This F layer will be used to serve as the fixed layer since it requires higher switching fields to switch it from the (P) to (AP) state.

The section follows we show the first results of a JMRAM cell composed of a PSV (ferromagnetic barrier) where F will $Ni_{80}Fe_{20}$ and F' will be $Cu_{0.7}(Ni_{80}Fe_{20})_{0.3.}$ The F' layer will play the role of the free soft layer which it's easy to switch with small magnetic fields.

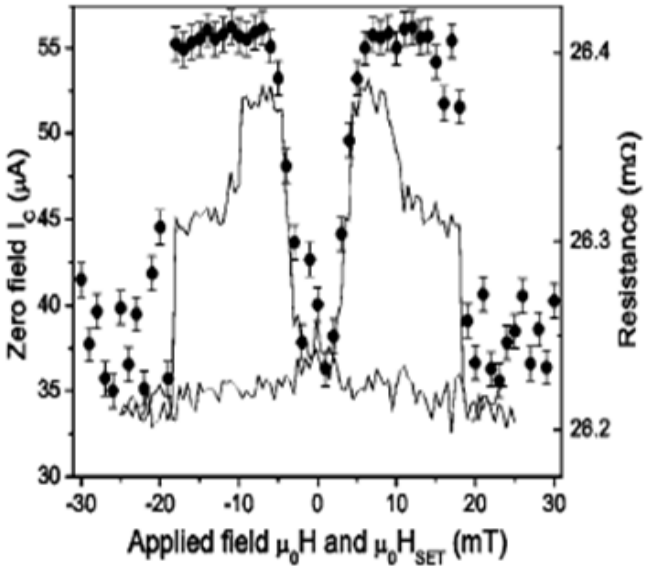


Figure 44. The state of critical current of a JJ with a PSV barrier switched between two states the P and AP states [97]

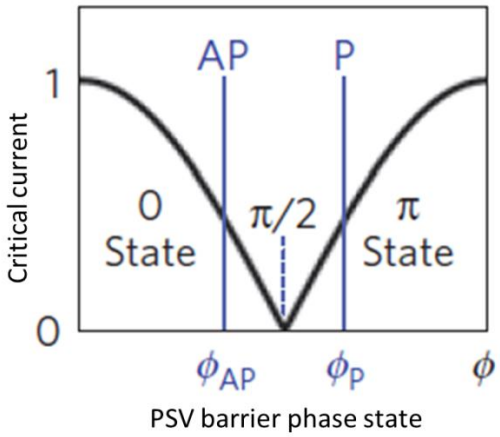


Figure 45. Cartoon showing the critical current and phase state of an S/F/N/F'/S Josephson junction as a function of the total phase shift acquired by a Cooper pair traversing the entire structure

5.2 Growth and fabrication

An unbaked UHV growth chamber with a base pressure of ~$2\times10^{-8}$ Torr was used in this (1) Nb(100 nm)/permalloy/Nb(100 nm) SFS structures and (2) Nb(100 nm)/permalloy(2.4 nm)/Al (9 nm)/$Cu_{0.7}(Ni_{80}Fe_{20})_{0.3}$/Nb(100 nm) SFNF'S structures. Permalloy thicknesses ranging from 0.6 to 6.2 nm were used in the SFS structures. For the third type of structure (SFNF'S), copper-permalloy alloy layer thicknesses of 2.4 nm and 5.0 nm were used. An Al spacer thickness of 9 nm was used to avoid significant magnetostatic coupling between the F layers.

The thin-film layers were deposited on unheated sapphire (100) and oxidized Si (100) substrates. The films were sputtered with magnetron sources under an Ar pressure of 4 mTorr at 70 sccm. The copper-permalloy alloy films were co-deposited with permalloy and Cu planar magnetron sputter sources. To controllably adjust the Cu content, the

power of the permalloy source was maintained at 25 W while the power of the Cu source was varied from 5 to 30 W. Rutherford backscattered spectroscopy (RBS) and particle induced X-ray emission spectroscopy (PIXE) was used to measure the chemical content and the thickness of the thin films.

The films were patterned into micron size crossbar geometry tunnel junctions using three level photo masks. Conventional microfabrication methods were used to define the junction following the anodization isolation methodology described in chapter 3 of this thesis.

The current-voltage characteristics of the SFS and SFNF'S devices were characterized using 4-point measurements with a liquid He dipping probe inserted in the Quantum Design PPMS cryostat at zero-magnetic-field. A Keithley Model 220 current source and Agilent model 34420A nanovoltmeter were used in the electrical measurements described in chapter 2 of this thesis.

## 5.3 S/F/S 0-π junctions

### 5.3.1 Overview

As discussed above, initially we have grown and fabricated different S/F/S structures where S-Nb with thickness of 100 nm and F= $Ni_{80}Fe_{20}$ with varying thickness. The aim of this study is to characterize the electrical measurements of these devices and figure out from the results at what F layer thickness does the junction transition into the π state. Figure 46 shows a cartoon of the fabricated S/F/S structures. Figure 47 shows a cross sectional TEM of the fabricated S/F/S JJ.


Figure 46. Cartoon showing grown S/F/S structures with S =Nb and F = $Ni_{80}Fe_{20}$

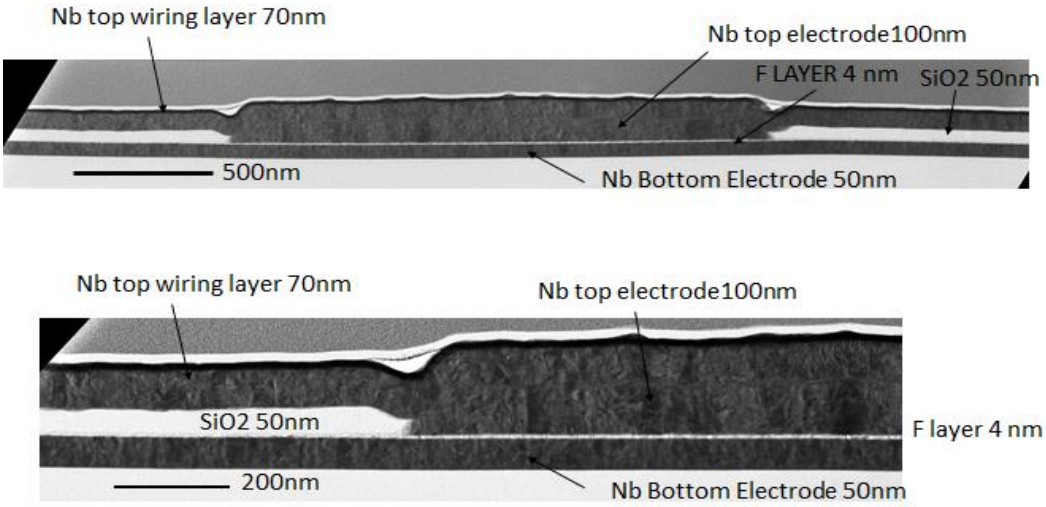


Figure 47. Cross-sectional TEM of an S/F/S junction with 4 nm $Ni_{80}Fe_{20}$

5.3.2 I-V characteristics

Figure 48 shows the measured $I_cR_n$ of Nb/permalloy (1.2 nm)/Nb Josephson square junctions as a function of permalloy thickness. The junction sizes are 5x5 $\mu m^2$, 10x10 $\mu m^2$, and 20x20 $\mu m^2$ on each chip. The critical current of those junctions scaled with area and were strongly modulated with applied field and temperature as shown in Figure 49 and Figure 50 respectively. Other I-Vs from different junctions are shown in

Figure 51 and Figure 52 for 1.3 nm and 2.4 nm F layer thickness Figure. 5.5 shows hysteretic behavior, even though the device's McCumber parameter is small. This is found because of the significant parasitic capacitance in our dipping probe wiring and rf filtering.

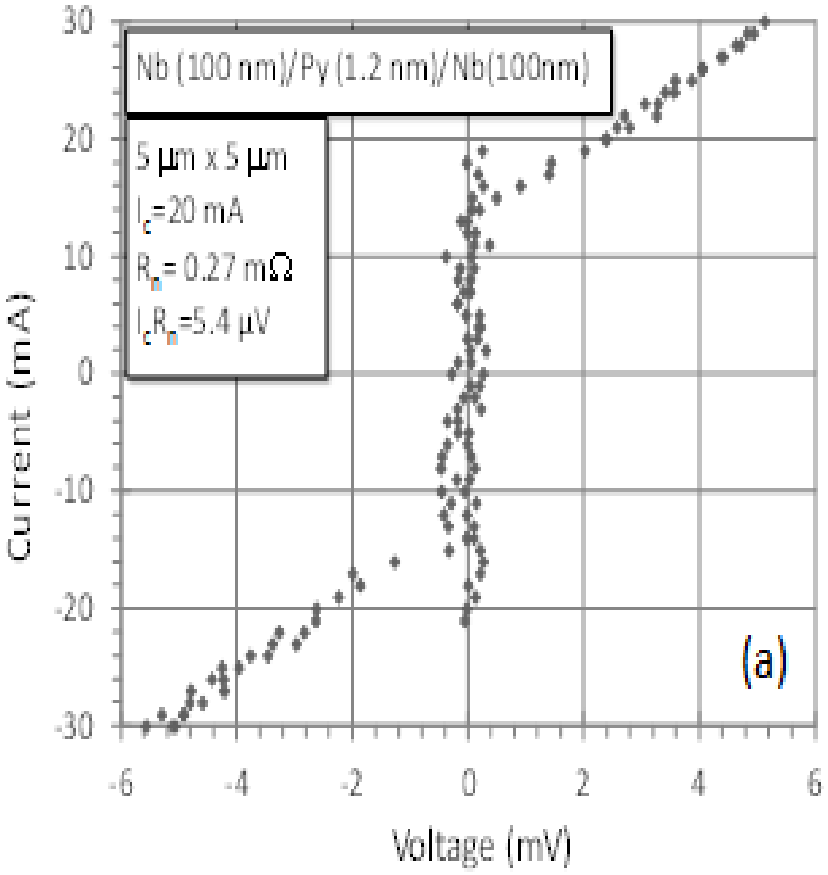


Figure 48. I-V characteristic of S/F/S junction with a 1.2 nm permalloy $Ni_{80}Fe_{20}$ thickness [75]

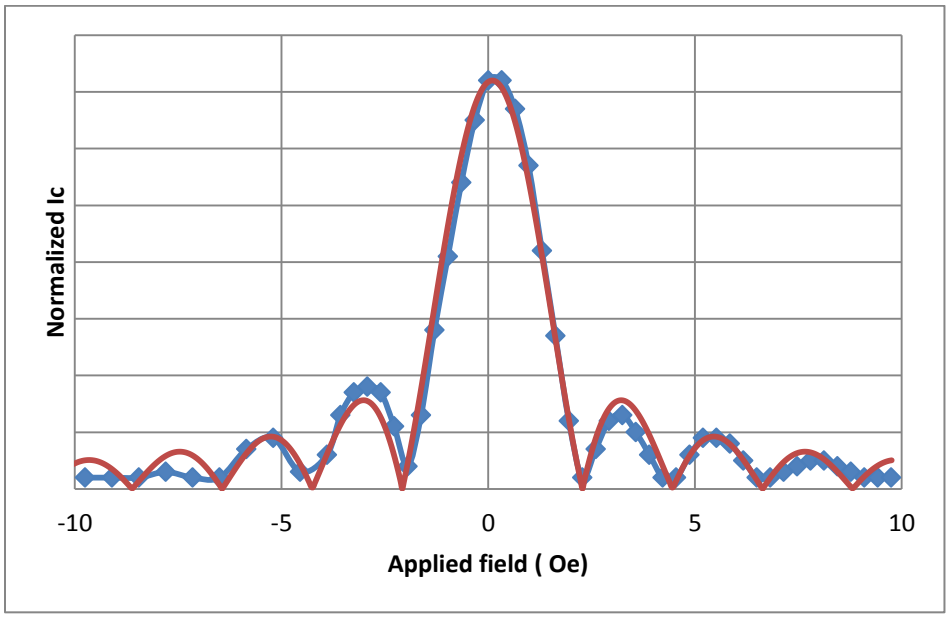


Figure 49. Magnetic field dependence of critical current for S/F/S junction and its theoretical fitting (Penetration depth λ=95 nm was used for fitting)

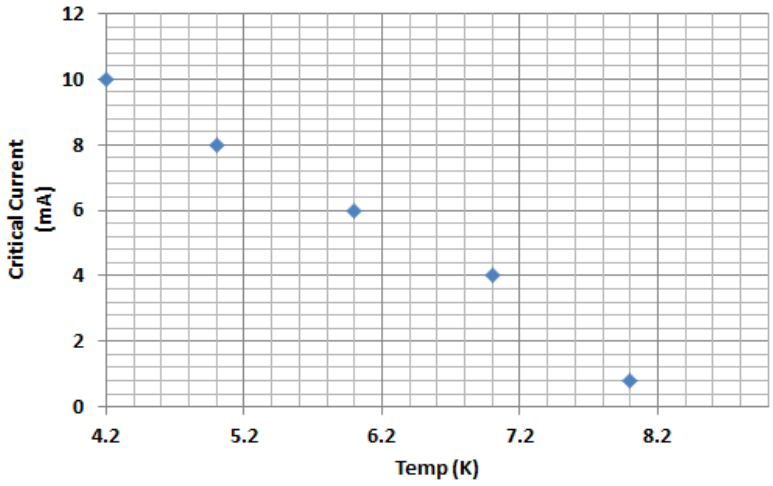


Figure 50. Temperature dependence of the critical current for S/F/S junction with a 1.3 nm permalloy $Ni_{80}Fe_{20}$ thickness

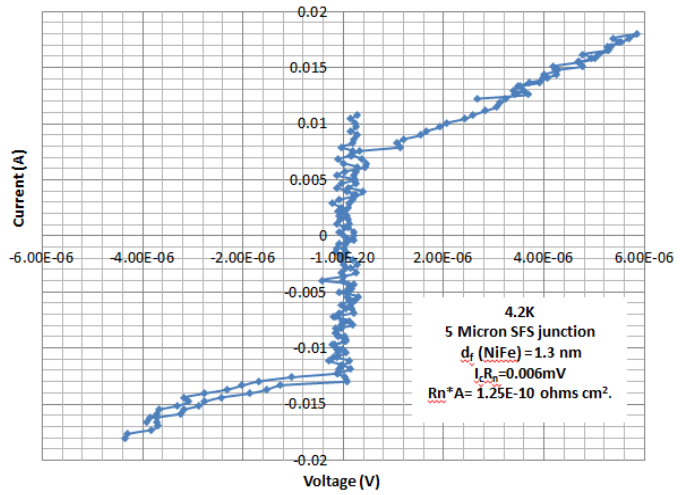


Figure 51. I-V characteristic of S/F/S junction with a permalloy $Ni_{80}Fe_{20}$ thickness of 1.3 nm

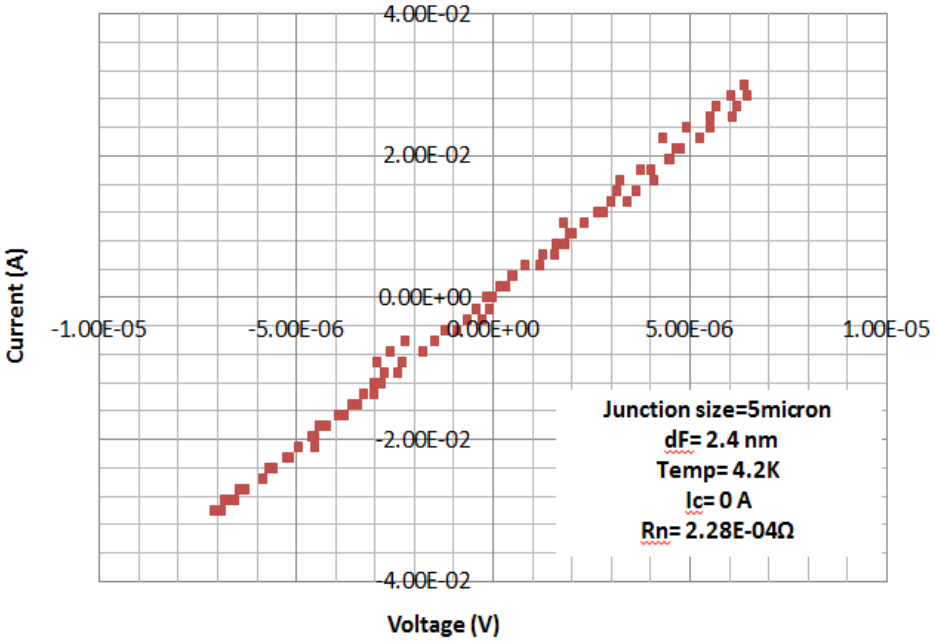


Figure 52. I-V characteristic of S/F/S junction with a permalloy $Ni_{80}Fe_{20}$ thickness of 2.4 nm (Thickness of 0-π cross over)

5.3.3 0-π cross over

Figure 53 shows change in $I_cR_n$ of the junction as a function of permalloy thickness. The first local minimum, characteristic of a π/2 phase-shift, is observed at 2.4 nm. This transition separates the 0 and π state of the junction. Two similar studies by Blamire's group have been reported, although they reported different values for the first minimum at 1.2 nm in one report and 2.4 nm in the other [32, 99].

In summary, we chose to use 2.4 nm of permalloy to set the phase-shift through the fixed ferromagnetic permalloy layer to π/2 in our SFNF'S devices. If this is done, the free layer would then shift the phase into either the 0 or π state, depending on if it is in the anti-parallel or parallel magnetic orientation to the fixed layer. The accuracy to which the permalloy layer thickness and uniformity can be set at the π/2 "pivot point" will determine the minimum amount of phase-shift that the free layer will need to make to provide reliable switching to either the 0 or π state.

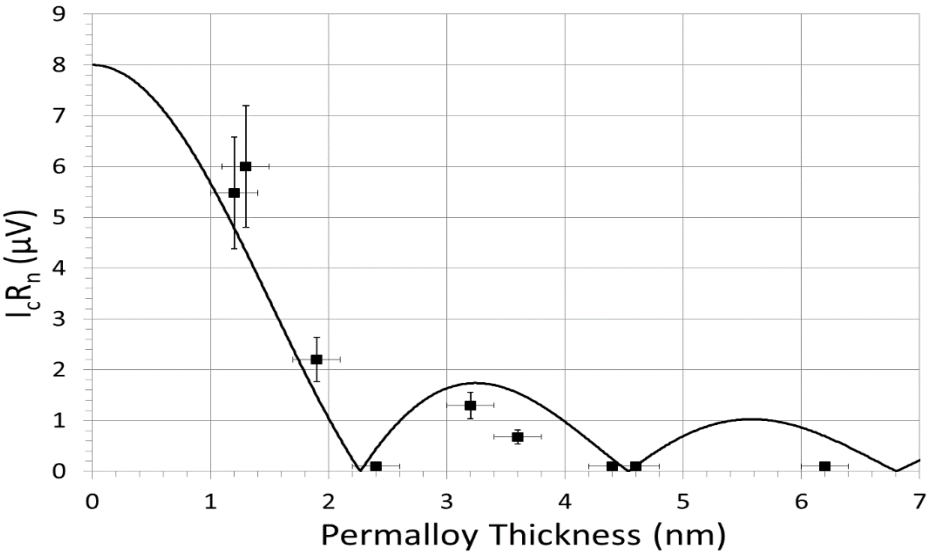


Figure 53. Measured IcRn of Nb/Py/Nb Josephson junctions as a function of permalloy thickness. The vertical error bars represent the standard deviation in the measured $I_cR_n$ obtained from several 5 to 10 lm square junctions on the same substrate. The error in the layer thickness in the RBS measurements is expected to be <_0.2 nm. The solid line is the fit with the data [75]

## 5.4 S/F/N/F'/S junctions for JMRAM application

### 5.4.1 Overview

The devices were grown and fabricated as discussed in earlier chapters and sections. Figure 54 shows the UHV chamber that was used to grow the S/F/N/F'/S structures. .The device geometries are shown in Figure 55. Figure 55a shows the P state whereas Figure 55 b shows the AP state. The devices as shown are composed of two top and bottom Nb electrodes with a PSV (F and F' soft – low energy switching and hard-high energy switching layers). Our devices with materials used are shown in Figure 56.

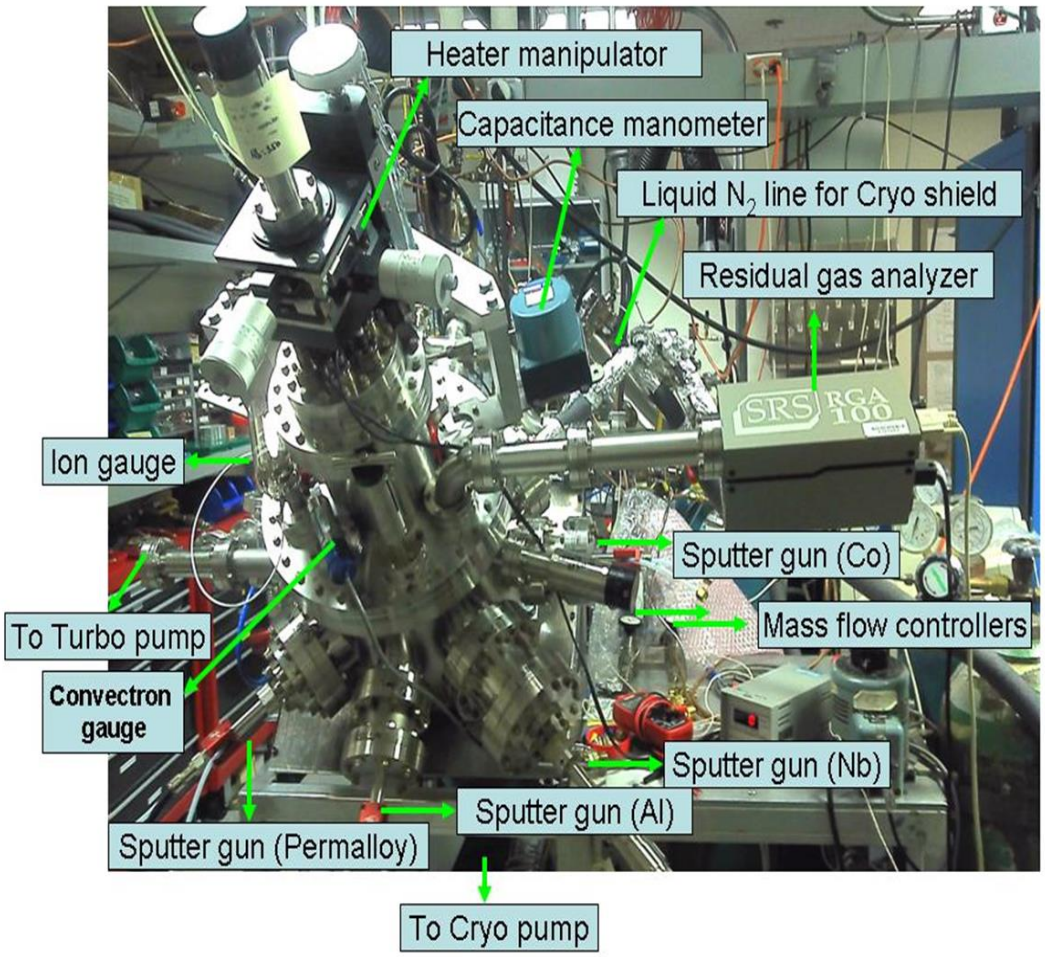


Figure 54. UHV growth chamber for S/F/N/F'/S structures

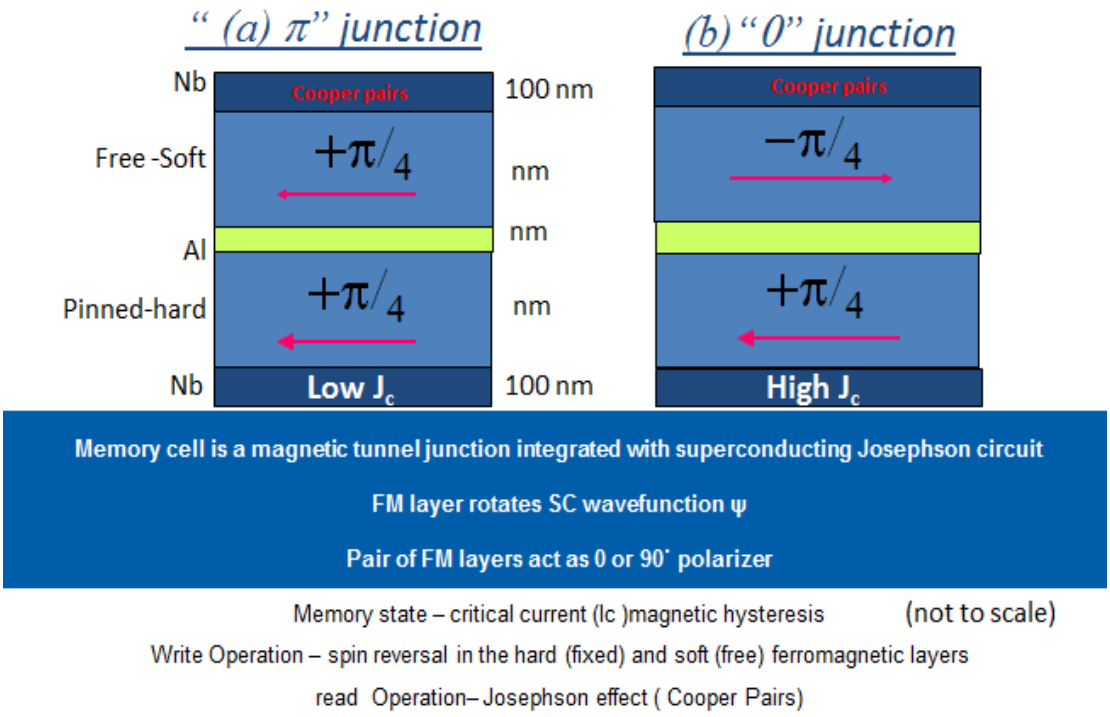


Figure 55. One rendition of S/F/N/F'/S JMRAM cells fabricated and characterized in this thesis. (a) The JMRAM cell in the (P) state where the two ferromagnetic layers magnetization is pinned in same directions and produces the maximum critical current. (b) The JMRAM cell in the (AP) state where the two ferromagnetic layers magnetization is pinned in opposite directions and produces a minimum critical current ($I_c$ =0).

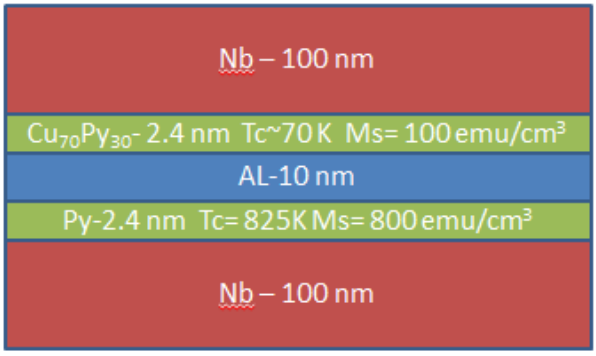


Figure 56. ASU JMRAM- S/F/N/F'/S cell

Electrical characterization of the SFNF'S structures was carried out in the following sequence. The magnetic states of these structures were initially aligned by applying a saturation field of 1 T in the plane of the magnetic layers at 4.2 K. The sample was then warmed to 15 K, and then returned to 4.2 K to minimize the influence of trapped flux in the junction's Nb-electrodes. To modify the magnetization direction of the layers, an external field, labeled $H_{set}$, or a current-driven field (via the top-electrode Nb wiring), labeled $I_{set}$, was applied to the device. The externally applied ($H_{set}$) or current-driven ($I_{set}$) magnetic field was subsequently removed and the I-V characteristics were measured at zero applied field [75].

5.4.2 IV characteristics

Figure 57 shows a typical IV behavior of our measured S/F/N/F'/S devices. The junctions were measured at 2 K to get the maximum critical current and to be in the lowest noise regime.

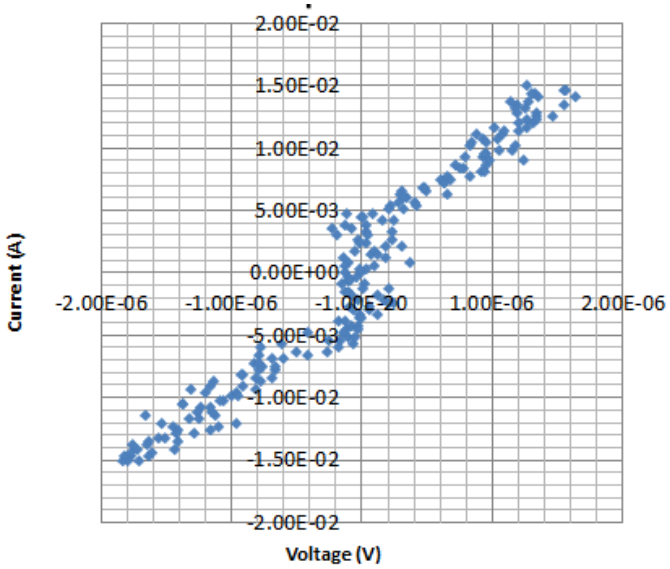


Figure 57. IV characteristics of 2 micron square S/F/N/F'/S devices measured at 2 K

Figure 58 shows the temperature dependence of the measured junctions and Figure 59 shows the field modulation of the junction critical current. The random pattern arises due to the intrinsic magnetic flux of the complex domain structure of the F layers.

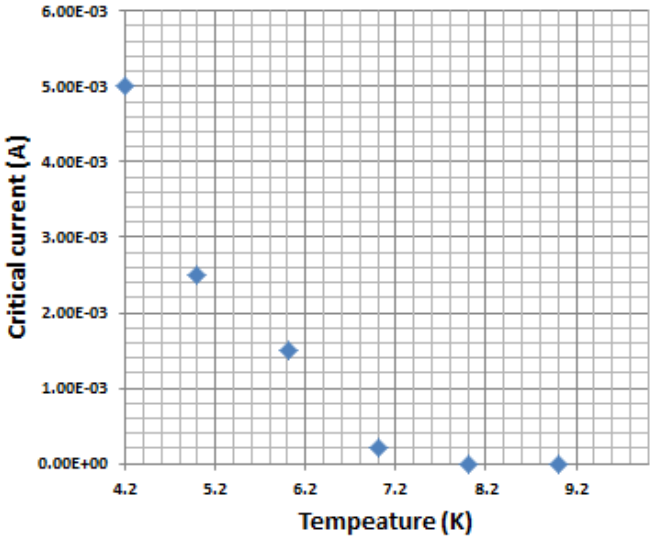


Figure 58. Temperature depended of the critical current of the measured S/F/N/F'/S device

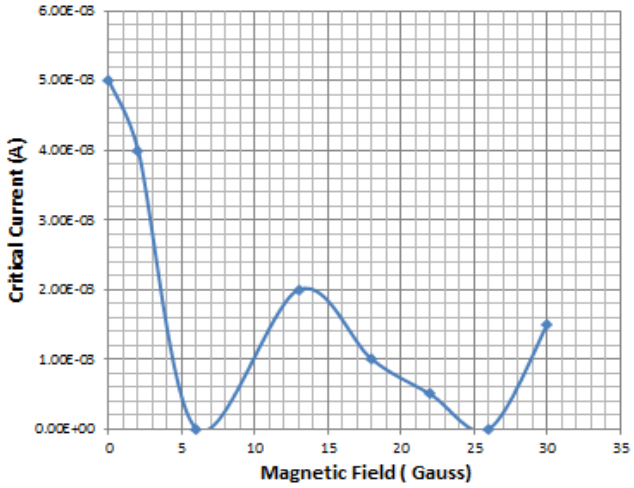


Figure 59. Magnetic field dependence of the critical current of the measured S/F/N/F'/S device

5.4.3 External field induced JMRAM cell switching

Figure 60 (a) demonstrates the magnetic switching of the critical current, Ic, of a 2 μm x 2 μm square junction fabricated with a 2.4 nm permalloy ($Ni_{80}Fe_{20}$) fixed layer and a 2.4 nm copper-permalloy alloy [$Cu_{0.7}(Ni_{80}Fe_{20})_{0.3}$] layer. The well-known "butterfly" curve shows well defined switching (Figure 60). When the device is swept from positive to negative fields (solid squares), the critical current starts to increase to near 12 Oe and then saturates at 0.12 mA for fields between 40 and 65 Oe. This is indicative of switching of the copper-permalloy free layer. The gradual increase in critical current when it is switching is indicative of incomplete switching resulting from the presence of multiple domains in the ferromagnetic layers. This is anticipated given that the device is larger than the 1.2 μm dimensions needed to make single domain structures for permalloy [100] As the field is increased beyond 65 Oe, the critical current decreases as a result of

switching of the permalloy fixed layer, aligning both layers again. Sweeping in the opposite direction gives analogous results and gives the characteristic “butterfly” pattern of switching. The observed resistance changes illustrated in Figure 60 (b) are associated with the spin-valve effect resulting from interface scattering.[101] Rn appears to change on the order of 25 %–35 % between states, although the accuracy in determining this parameter is low due to the small voltage range in which it is measured.

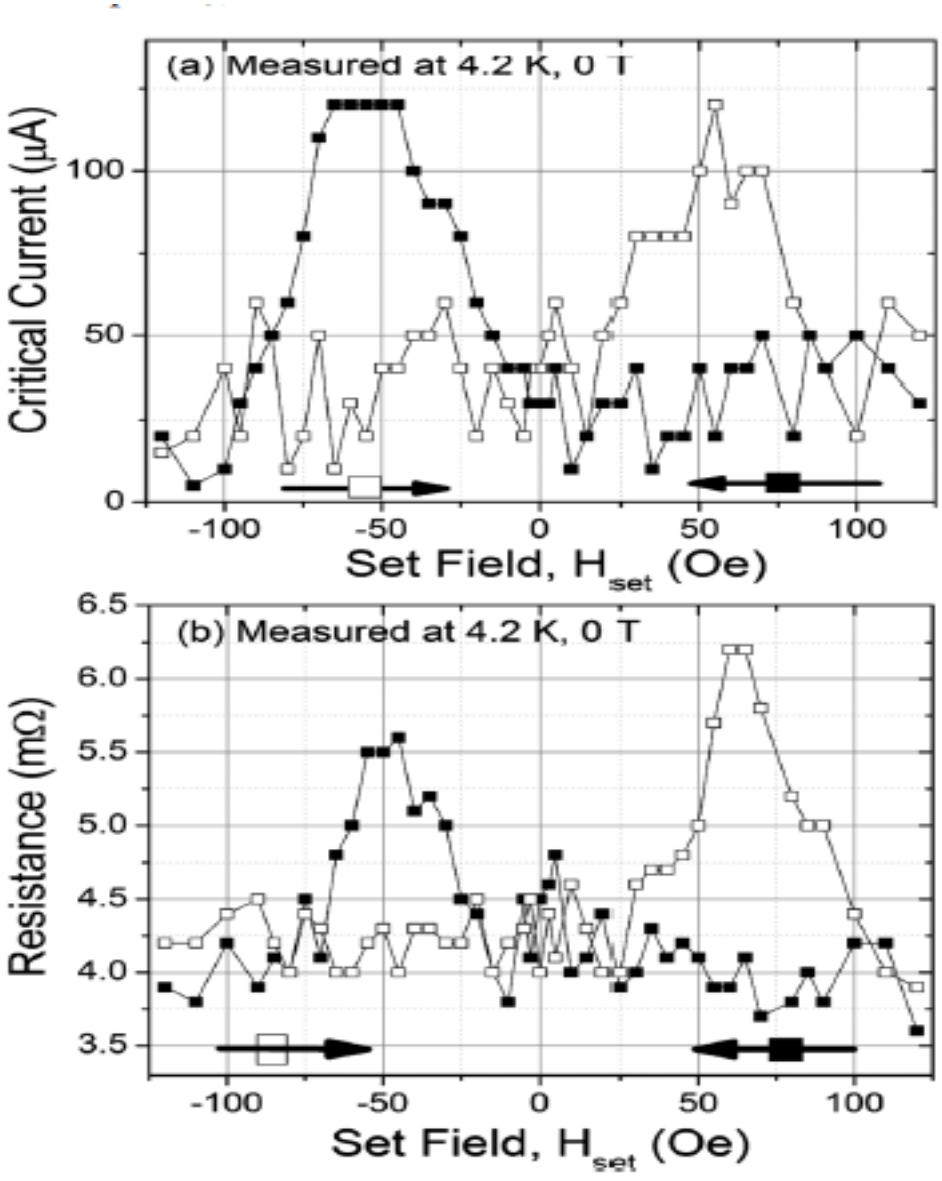


Figure 60. Magnetic switching of (a) critical current $I_c$ and (b) resistance $R_n$ of a $Nb/Cu_{0.7}(Ni_{80}Fe_{20})_{0.3}/Al/Ni_{80}Fe_{20}/Nb$ 2 μm square junction fabricated with a 2.4 nm permalloy fixed layer and a 2.4 nm copper-alloyed permalloy layer. In these measurements, the magnetic field, the "Set Field," was applied to alter the state of the ferromagnetic layers and then the I-V measurements were made at zero-field.[75]

Figure 61 shows similar switching behavior in a rectangular 2 μm x 5 μm junction with a 5.0 nm copper-alloy permalloy, in which switching fields were applied along the long axis of the junction. As the field is swept either from the right or left and goes just past zero, a very sudden jump in the $I_c$ can be observed in Figure 61. This significant increase occurs at very small applied field magnitudes, on the order of 5 Oe. This does indicate that the copper-permalloy free layers can be manipulated at very small applied magnetic fields, although the switching is not complete as a result of multi-domain structure. Reliable switching of this device was also observed when 20 mA of current was sourced through the top electrode. The use of smaller and engineered shapes of the memory elements is planned for developing future memory elements. We do note that this device with a 5.0 nm thick free layer can be switched at smaller magnetic fields than the one fabricated with a 2.4 nm thick free layer, even though it has both a larger volume and shape anisotropy. The thicker copper-permalloy alloy appears to have improved magnetic switching properties, presumably as a result of fewer defects. Interfacial and bulk defects can cause strain and the resulting anisotropy in the layers as well as domain pinning sites.

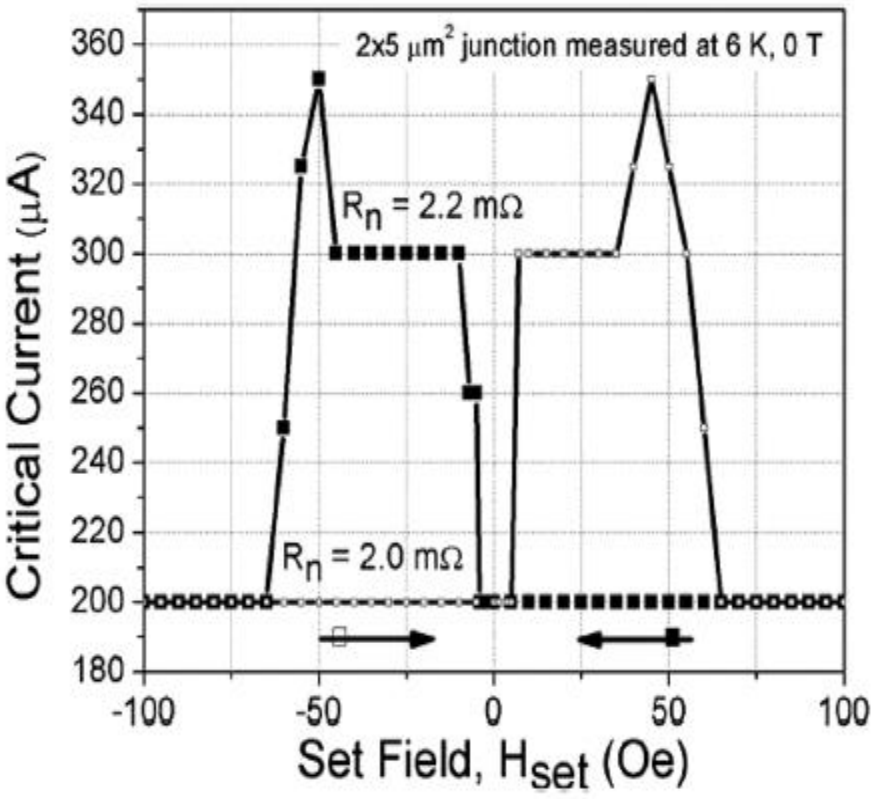


Figure 61. Magnetic switching of the critical current Ic of a 2x5 μm $Nb/Cu_{0.7}(Ni_{80}Fe_{20})_{0.3}/Al/Ni_{80}Fe_{20}/Nb$ square junction fabricated with a 2.4 nm permalloy fixed layer and a 5 nm copper-alloyed permalloy layer [75]

5.4.4 Current induced JMRAM cell switching

We were also able to switch the SFNF'S junction using a magnetic field applied by the top Nb electrode wiring. Figure 62 shows that the devices can be consistently switched with set current magnitudes of 30 mA, but could not be reliably switched at 5 mA. The differences in observed high state and low-state critical currents for switching at +30 mA and +5 mA are again associated with the multi-domain structure of the ferromagnetic layers in the devices. The use of the top electrode to switch the fields is

clearly not ideal for a number of reasons, including exposing the multi-domain ferromagnetic layers to highly non-uniform fields. In future work, we will use separate write lines with smaller, single domain, devices; Figure 63 shows the corresponding IV scans before after the 30 mA current induced switching.

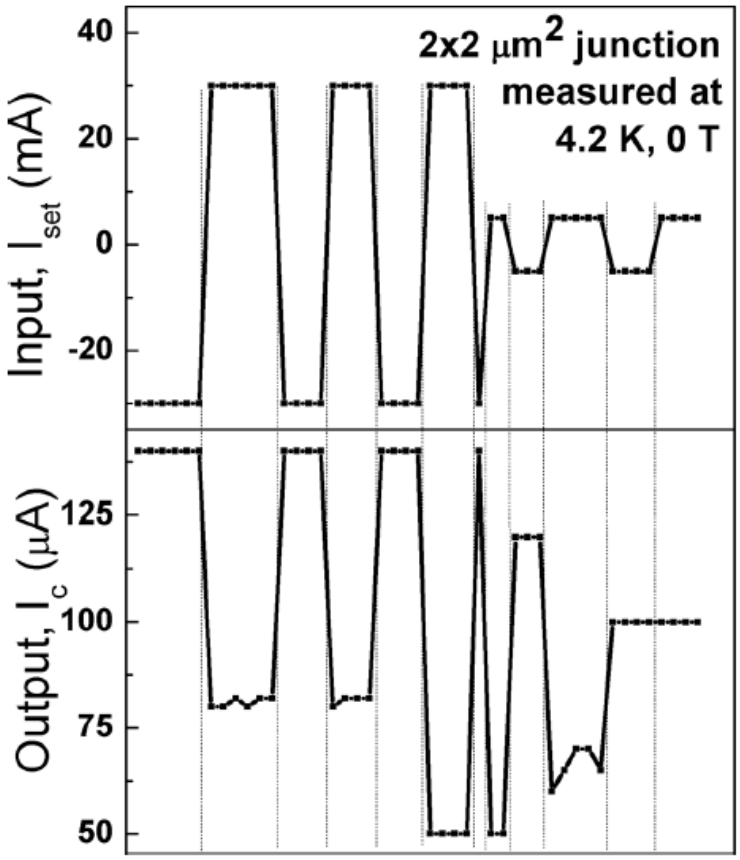


Figure 62. Use of an input top electrode current, $I_{set}$, to generate a field to switch the free-layer magnetic layer orientation, and resulting changes in the output critical current $I_c$ of a 2 μm square $Nb/Cu_{0.7}(Ni_{80}Fe_{20})_{0.3}/Al/Ni_{80}Fe_{20}/Nb$ junction fabricated with a 2.4 nm permalloy fixed layer and a 2.4 nm Copper-alloyed permalloy free layer. In these measurements, the Set Current, $I_{set}$, was initially applied to alter the state of the ferromagnets and then the I-V measurements were made at zero-field [75]

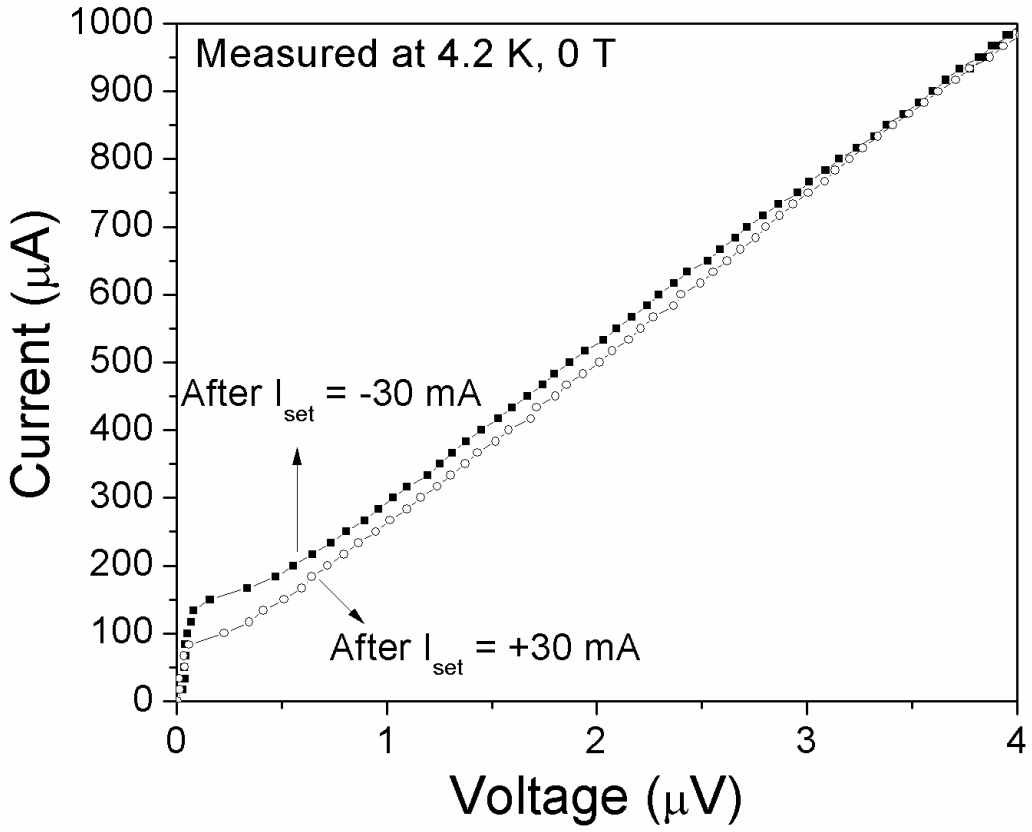


Figure 63. IV scan shows the critical current is switched between two states upon the induced current switching

5.4.5 Discussion

The measured $I_cR_n$ of the SFNF'S devices are on the order of 1 μV. Higher values are desired for fast switching, as the $I_cR_n$ product serves as a figure of merit for the maximum operating speed of devices in SQUID loops or other circuitry The junction switching speed needs to be slower than its natural frequency, $f \approx I_cR_n/\Phi_o$, so that the superconductor phase can reach its equilibrium under those conditions [1] [$\Phi_o$ is the flux quantum of ~2 mV ps]. Since our ferromagnetic alloys are in the dirty limit, $I_cR_n$ is expected to scale roughly as $\exp(-x/\xi)|\sin(x/\xi+\phi)|$,where $\xi=\hbar v_f l_{mfp}/3E_x$ is the decay

constant, , $\phi$ is an angle that depends on the spin-flip and spin-orbit scattering process, $\hbar$ is the reduced Planck constant, and $l_{mfp}$ is the mean free path.[102] Thus, for the pinned layer to rotate by, $\pi/2$ the critical current density must decay by a value on the order of $e^{-\pi/2}$~4 from a typical Nb superconductor Jc of say. $2x10^7$ A/cm$^2$. Since the free layer needs to move the wavefunction to say $^{\pi}/_4$ to get a large $I_c$, within a factor of 2, the critical current density will decay by another ~$e^{-\pi/4}$~½.

The resistance of our structure based on 4.2 K bulk resistivity values [20 μΩ cm for permalloy and 100 μΩ cm for $Cu_{0.7}(Ni_{80}Fe_{20})_{0.3}$,] and the known interface specific resistances [6.5 mΩ μm$^2$ for Nb-permalloy,1 mΩ μm$^2$ for permalloy- copper[103] the $R_n$ would be expected to be 2 mΩ for the structure shown in Figs. 5.17. This is relatively close to the measured value, given that the values for the interface specific resistances of the two interfaces to Cu-alloyed permalloy are not available in the literature and thus were not included in this estimate. However, we do note that the measured $I_cR_n$ values are orders of magnitude lower that the resulting $I_cR_n$ estimate of 800 μV, suggesting that optimization of the SFNF'S superconducting properties is possible. Earlier reports in the literature of SFS and SFNF'S have reported $I_cR_n$ values in the one to tens of microvolt range [10, 31, 76 and 97].

### 5.4.6 Conclusion

In conclusion, by using a dilute Cu-permalloy alloy with low saturation magnetizations (~80 emu/cm$^3$) as a free layers and permalloy with a high saturation magnetic field (~800 emu/cm$^3$) into Nb-based Josephson junctions, we have

demonstrated that a JMRAM device structure can be fabricated with a small onset switching field. A 2.4 nm thick permalloy fixed layer was used to shift the phase of the wavefunction to the $\pi/2$ pivot point. The accuracy with which the permalloy layer thickness and uniformity can be controlled will determine the minimum phase-shift required from the free layer to provide reliable switching. The memory devices reported here demonstrate nonvolatile, low energy switching characteristics.

# CHAPTER 6 PROXIMITY EFFECT IN SUPERCONDCUTOR/ MAGENTIC SYSTEMS

## 6.1Abstract

The superconducting critical temperature, $T_c$, of several Nb/magnetic alloy bilayer structures were measured for a range of ferromagnetic thicknesses ($d_F$). The results for $Nb/Ni_{80}F_{20}$, $Nb/Ni_{65}Fe_{15}Co_{20}$ bi-layers and Nb/ferromagnetic $Pd_{1-x}Ni_x$ (i.e. $x\geq3$) exhibit a minimum in $T_c$ at very near the ferromagnetic's deadlayer thickness and not near the thickness which causes a $\pi/2$ shift in the superconductor wavefunction. In contrast to the results using ferromagnetic layers, the $T_c$'s of the bilayers with paramagnetic $Pd_{1-x}Ni_x$ (i.e. $x<3$) layers do not exhibit a $T_c$ minimum with increasing thickness. To better understand how the superconductor wavefunction evolves, we measured the density of state (DOS) spectra using $Nb/Pd_{87}Ni_{13}$ /Al/$AlO_x$/Al tunneling structures for a number of different ferromagnetic layer thicknesses. Remarkably, we find that as $d_F$ increases, DOS exhibits a scaling behavior with a universal shape, which decreases exponentially with a characteristic decay length, $\xi_{F1}$, $_{of}$ 0.88 nm. We use these results to evaluate the proposed proximity models in the literature.

## 6.2 Introduction and motivation

The Proximity effect between a superconductor (S) and a normal-metal (N) has been observed experimentally and accurately modeled in many previously published papers [27, 29]. The theoretical predictions are based on superconductor Copper pairs diffusing into the normal metal side and normal metal electrons diffusing into the superconductor, causing a drop of the order parameter (OP) starting at about a coherence length within the superconductor and then throughout the normal metal layer. The

characteristic decay length, named the coherence length $\xi_N$, is on the order of the mean free path.

On the other hand, the co-existence of both superconductor and a ferromagnetic (F) material is rare in bulk materials [104,105]. However, it may be easily achieved in artificially grown layered structures. Such hybrid systems can be used in many applications, including new evolving spintronic technologies [75]. Due to the large exchange field energy in the magnetic layer, this proximity in such systems has a very short exchange decay length $\xi_F$, typically of only a few nm. Interestingly enough, the phase of the superconducting order parameter was predicted theoretically [106] to oscillate as a function of distance into the superconductor [107]. A number of different experimental results verified this conjecture, including observation of oscillations in the critical temperatures of S/F bi-layers as a function of the ferromagnetic layer thickness ($d_F$) [108], variation in the critical temperature of F/S/F tri-layers as a function of the relative magnetization ($M_s$) direction of the two ferromagnetic layer –layers [109], oscillations of the critical current ($I_c$) in fabricated S/F/S Josephson junctions[110], and as oscillations between "normal "and "inverted" proximity features in the tunneling density of states (DOS) of S/F/I/N tunnel junctions [111], where I is an insulator.

The oscillatory behavior of the OP is explained as following. The spin and crystal momentum of electrons in Cooper pairs are coupled parameters in a superconductor (i.e. $+k\uparrow$ and $-k\downarrow$). When they are injected into a ferromagnet, each electron experiences the exchange field, causing the electrons with spins oriented in the direction of the field to increase in velocity, while those opposed slow down. This causes the net crystal

momentum to increase to a finite value, $\Delta k=2E_{ex}/(\hbar v_{F)}$, where $E_{ex}$, is the exchange energy, $v_F$ is the Fermi velocity, causing the superconductor wavefunction, $\Psi_o e^{-i\Delta kx} = \Psi_o e^{-x/\xi_{F1}} e^{-ix/\xi_{F2}}$, to decay and shift its phase [112]. In the clean limit, the spatial period of the oscillations is dictated by the exchange length, $\xi_{F1=} \hbar v_F/2E_{ex}$. In the dirty limit, the amplitude's decay rate and the phase's spatial period are equal, $\xi_{F1=} \xi_{F2=}$ Sqrt[$\hbar D/E_{ex}$], where $D= v_{F*} l_{mfp}/3$ is the diffusion constant and ( $l_{mfp}$) is the mean free path. In the dirty limit, the characteristic length $\xi_F$, of this oscillation is very small, on the order of nm in the conventional well-known strong magnets, such as Co, Fe, or Ni. In order to increase this characteristic length $\xi_F$, conventional magnetic materials have been alloyed with normal metals, to produce weaker magnets, such as Cu-peramlloy / PdNi and CuNi alloys [102,113].

The $T_c$ behavior of S/F bi layer has been reported by many groups and, surprising to the authors, the results are found to often vary significantly. In the case of Nb/Fe systems, Mughue et al. [114-118] observed a non-monotonic behavior of Tc and he suggested that the thickness of the Tc minimum to occur at the onset of ferromagnetism in the thin layers, On the other hand, Verbanck et al. [119] observed a step-like decrease of $T_c(d\text{Fe})$ in their MBE grown samples at the same nominal thickness of Fe layer $\sim 14$ A˚ , for which an oscillation of the critical temperature was detected by Mughge et al. The observations of Verbanck et al. are not consistent with the conjecture of Mughue et al. For the case of Nb/$Pd_{86}Ni_{14}$ bilayers, K I Matsuda et al [120]. and C.Cirillo et al [121] observed a non-monotonic behavior between $T_c$ and ferromagnetic thickness. They interpreted the results in the framework of the model proposed by Fominov [121b].

However, this interpretation is not unique in that there are large error bars in the few data points measured, and $T_c$ was measured over small sampling range. Multiple groups have chosen to study the weak magnets, such as $Cu_{1-X}Ni_x$ alloys, in order that the Tc minimum is expected to be thicker than both the ferromagnet dead layer thickness and when the layer coalesces into a continuous layer. However, the results again were found to differ significantly from other's findings. V.V.Ryazanov et al [122] shown a non-monotonic behavior of $T_c$ with a weak minima at $d_F$= 5 nm , and A.Angrisani et al. [123] shown monotonic thickness dependence of $T_c$ with no clear minima. On the other hand, V. Zdravkov et al. [124] observed reentrant superconductivity at low temperatures (is this correct) and large-amplitude oscillations in the superconducting $T_c$ with increasing $Cu_{41}Ni_{59}$ alloy layer thickness and with a constant Nb layer thickness. ($d_{Nb}$ ≈7.3 nm and $d_{Nb}$ ≈8.3 nm). That report interpreted the results with the Fulde- Ferrell and Larkin-Ovchinnikov (FFLO) model [125]. These samples were capped with a protective layer on the ferromagnet to prevent oxidation. Strunk *et al.* found that the $T_c$ of Nb/Gd/Nb tri-layers [126] exhibited a step-like behavior at the thickness of the Gd when it first shows ferromagnetism. However, the $T_c$ of Nb/Gd multilayers were found to oscillate with thickness in the study by Jiang et al. and they ascribed the oscillation to -phase coupling [127]. Recently, A.S.Sidorenko et al. [128] that the $T_c$ dependence of Nb/Ni bilayers oscillated with increasing thickness. Sidorenko fit the results to the amplitude decay of phase shift predicted by the FFLO model.

From the above analysis of recent experimental results we may draw the following conclusions:

1) S/F bilayer samples grown with sputtering are found to exhibit a minimum in Tc with thickness, while those growth with MBE do not. For the Nb/Fe system this important difference in the $T_c$(dFe) behavior for MBE and sputtered samples was noted in Refs. [114-118] and attributed to a subtle change in the interaction of Cooper pairs with a magnetically "dead" interdiffused layer at the S/F interface.

(2) To avoid island growth due to non-wetting of the upper layers, the S/F couples should not consist of immiscible metals. Rather, materials with limited solubility and fine composition ranges of intermetallic compound formation should be used.

(3) The interface roughness of F-layers should be small compared to the F-layer thickness

(4) The use of a capping layer important to prevent the loss of part of the ferromagnetic layer and any influence of a surface oxide layer.

(5) Growing samples in wedge from with constant Nb thickness and varying ferromagnetic layer thickness without breaking vacuum is beneficial to prevent run to run variations, particularly in the thickness and properties of the Nb superconductor layer.

(6) The Nb thickness should be small compared to its coherence length

Our study will be carried out with the preferred methods summarized in 1 to 6 above. To this end, we have deposited S/F bi-layers (S=Nb F=$Ni_{65}Fe_{15}Co_{20}$, $Ni_{81}Fe_{19}$ and $Pd_{1-x}Ni_x$) by DC sputtering in a UHV chamber. Rutherford Backscattering Spectrometry was used to measure the thickness of the Nb and ferromagnetic layer layers. The dependence of the critical temperature on the ferromagnetic layer thickness along with magnetic and structural characterization was investigated for different bi-layer systems.

Transmission electron microscopy and magnetometer measurements are used to study the initial stages of ferromagnetic film deposition. We will discuss how the chemical, topographical and magnetic properties of the initial over-layers affect the transition temperature of the bilayer system. The primary goals of this paper are the following:

1) While such oscillations are readily interpreted in S/F/S structures, the non-monotonic dependence of the superconducting transition temperature, $T_c(d_F)$, in S/F bi-layer systems has been proven to be more difficult to understand We will investigate the $T_c$ behavior in the strong magnets $Ni_{81}Fe_{19}$ and $Ni_{65}Fe_{15}Co_{20}$.and the weak magnet PdNi.

   By varying the Ni concentration in $Pd_{1-x}Ni_x$ alloys, we are able measure the $T_c$ behavior for bi-layers as the magnetic material transition from paramagnetic state to a very weak ferromagnet to a stronger ferromagnet.

2) With large experimental efforts in S/F/S Josephson junctions, the oscillation in critical current with F layer thickness has been experiential seen by many experimental groups [129,130]. What is startling is that, unlike in the Josephson junctions, the oscillatory behavior of the DOS in S/F/I/N structures has been observed only rarely, as a single normal-inverted transition in strcutres with a low $M_s$ and $T_{curie}$-ferromagnetic alloy for ferromagnetic layer [131]. In experiments using strong ferromagnets high $M_s$ and $T_{curie}$, the results have been less clear.[132,133].To probe the order parameter as a function of depth into the ferromagnet, we will fabricate S/F/I/N junctions with F=

$Pd_{87}Ni_{13}$ a relatively weak ferromagnetic system and study the DOS for a range of thicknesses. The results will be compared with Nb/ $Pd_{87}Ni_{13}$ bilayers of earlier section.

6.3 Experimental work

All S/F and S/F/I/N structures were deposited with a multi-source DC magnetron sputtering system at room temperature using a 300 nm oxide-buffered 1cm x 1 cm $Si/SiO_2$ substrate. After the chamber was pumped to base pressure of low $10^{-9}$ Torr, Nb films were deposited using 99.999 % pure argon gas at 1 mTorr. A solid Nb (99.95 % pure) target was used as a source and the deposition rate was 8 Å/sec. The uniformity of the Tc of each Nb sample was measured separately and found to be within 20 mK, and the uniformity of the $T_c$ of each Nb/F bi-layer sample were found to be within 50 mK. Then, ferromagnetic layers were grown in-situ directly after Nb deposition, to avoid likely contamination of the Nb film surface.

To achieve a systematic variation in the thickness of the ferromagnetic layers, we used the gradient of the sputtering rate caused when the sputter gun is placed at a ~80 degree angle from the substrate holder surface normal. 99.9 % pure $Ni_{81}Fe_{19}$, $Ni_{65}Fe_{15}Co_{20}$ and $Pd_{87}Ni_{13}$ solid targets were used as sources. To deposit the $Pd_{1-x}Ni_x$ alloys, a solid 99.9% Pd target with Ni slugs held magnetically on top was used. The deposition rates of each ferromagnetic layer were maintained at 0.1 Å//Sec. All the samples were capped with 3 nm of Al to prevent oxidation after removal from the

deposition chamber. The thickness, chemical composition and degree of intermixing of the structures were measured using Rutherford Backscattering spectrometry (RBS)

A standard mechanical shadow mask process was used to fabricate the S/F/I/N tunnel junctions. We first deposited the Nb/F/Al layers in-situ into a 2 mm x 10 mm strip using shadow mask 1. The samples were subsequently moved into the load lock chamber then we immediately backfilled the chamber with 500 Torr of 99% pure $O_2$. This exposed the freshly deposited Al to the $O_2$ for 10 minutes, initially while the Al is still hot about 60 ˚C. Next, we change masks and evaporate a thick layer (200 nm) of germanium Ge to define the junction geometry. The Ge is used to eliminate edge shorting and other forms of leakage current. The resulting junction size is 500 x 300 micron square. Finally, we sputter aluminum (N) as a top electrode and wiring lead using another mask. The 1 cm × 1 cm size wafers were placed in a gold-plated ceramic 44-pin chip carrier and the contacts were connected to the pads using gold wire and silver paint. Contacts were wire bonded using silver paint.

The magnetic properties, and temperature dependent magnetization of the bi-layer films were characterized using a vibrating sample magnetometer (VSM) from 2-1000 K (Quantum Design, Model Physical Properties Measurement, PPMS, System with oven option).

The resistance measurements of the bi-layer samples were performed using a conventional four probe method in the temperature range of 4.2-300 K. in a liquid Helium Dewar. The current-voltage characteristics of the S/F/I/N devices were characterized using 4-point measurements using Keithley Model 220 current source,

Agilent model 34420A nanovoltmete, and an automated software were used in the electrical measurements

A probe aberration-corrected JEOL ARM 200F was used for the high resolution structural and chemical characterization of the multilayer specimens. It is equipped with a JEOL energy dispersive X-ray spectrometer (EDS) and an electron energy loss spectrometer (EELS), and it is located in a low-vibration and quiet electromagnetic environment at Arizona State University (ASU).Cross-sectional specimens were prepared from the junctions using a focused Ga ion beam with SEM imaging. The initial cutting was done using a 30 keV accelerator voltage. The final thinning was done with the beam's energy at 5 keV at a small incidence angle. Higher beam energies cause noticeable specimen amorphization.

## 6.4 Results

### 6.4.1 Magnetic characterization

The magnetic state of all samples including single layer and bi-layer samples presented in this work studied using a vibrating sample magnetometer. Magnetization measurements of 100 nm thick $Ni_{65}Fe_{15}Co_{20,}$ $Ni_{81}Fe_{19}$, and $Pd_{87}Ni_{13}$ samples at a field of 1000 Oe measured the Curie temperatures to be 1000 k, 800 K, and 170 K respectively, consistent with earlier reported work [135, 136 and 137].

To correlate our Tc bilayers data to the magnetic state of the bi-layer as a function of the ferromagnet layer thickness, we measured the M-H loops for Nb/ $Ni_{65}Fe_{15}Co_{20,}$ bi-layers at 10 K, above the critical temperature of the bottom Nb electrode. The surface of the samples was parallel to the applied magnetic field .A magnetic transition from being superparamagnetic/ non-ferromagnetic to being ferromagnetic is observed in the bi-layers

at a well-defined thickness. Figure 64 shows clear change in the hysteresis loop transitioning from S like shape to more of a square shape M-H loops. To quantify this transition, we plotted the squareness ($M_r/ M_s$) and anisotropy field, $H_k$, of the loops as a function of ferromagnetic layer thickness. Figure 65 show that bellow 1.8 nm, $H_k$ increases markedly and squareness (Sq) decreases. Earlier reports observed that islands form during the initial stages of ferromagnetic layer growth, along with the anticipated poor magnetic properties [138, 139]

Figure 66 shows the magnetic moment per unit surface area of the, $Ni_{81}Fe_{19}$, and $Pd_{87}Ni_{13}$ as a function of film thickness By extrapolating the least-squares fit of the saturation magnetization to the x-axis, a magnetic dead layer thickness is inferred to be ~1.1 nm for $Ni_{65}Fe_{15}Co_{20}$ , ~ 0.85 nm for $Ni_{81}Fe_{19}$ and ~0.7 nm for $Pd_{87}Ni_{13}$. Magnetic Dead layers can arise from a number of physical factors, including a large lattice mismatch and the resulting elastic deformation, the formation of amorphous and highly defective regions during the initial stages of ferromagnetic layer growth and chemical intermixing. All of these factors can potentially reduce or eliminate the $T_{Curie}$ and $E_{ex}$ [140]

Figure 67 (Top) shows the measured magnetic moment versus applied field for $Nb/Pd_{1-x}Ni_x$ alloys (where x=0, 0.8 and 3 %) and Figure 67 (Bottom) shows a zoomed in hysteresis loop for the 3% Ni sample. For the pure Pd (X=0 %) the magnetic signal was dominated by the thick $Si/SiO_2$ diamagnetic substrate. The same occurred for Pd with (x=0.8 %). Thus, it can be inferred that the magnetic layer in the grown bi-layers are not strongly ferromagnetic and are presumably paramagnetic. These Ni dopants correspond

to the paramagnetic regime according to earlier work by Beillee [141] and Kontos [142]. The moment we increase the Ni dopant to (x=3%) the sample developed small hysteresis but no saturation even at high applied fields. This sample then can infer to be in the superparamagnetic regime (or onset of ferromagnetism). This was also confirmed in Kantos' earlier work [142]

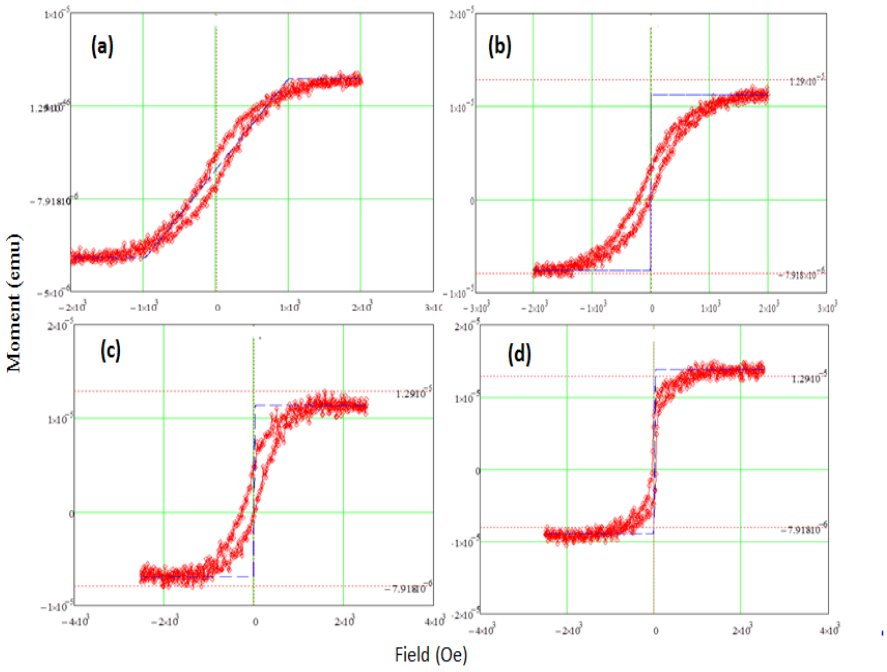


Figure 64. M-H hysteresis loops for Nb/, $Ni_{65}Fe_{15}Co_{20}$ bilayers measured at 10 K in a VSM. The thickness of the Nb for all samples is 40 nm while the, $Ni_{65}Fe_{15}Co_{20}$ F-layer thickness varies from (a) 0.6 nm (b) 1.5 nm (c) 1.8 nm and (d) 2.2 nm

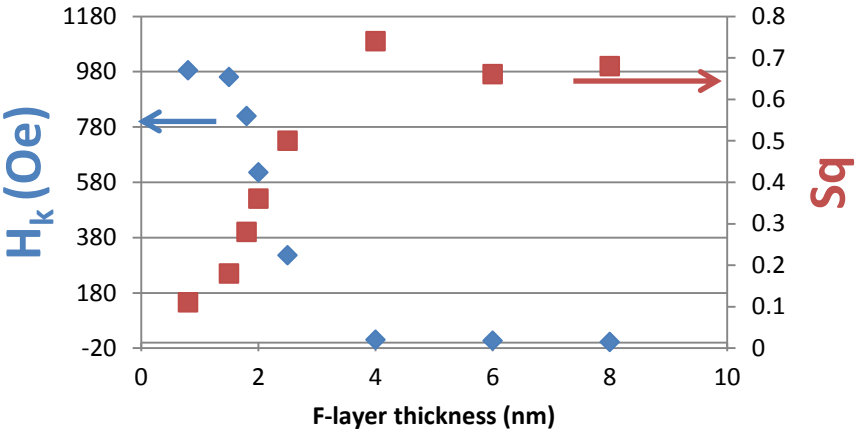


Figure 65. Anistropy ( $H_k$) and squarness (Sq) for Nb/, $Ni_{65}Fe_{15}Co_{20}$ bilayers measured at 10 K plotted as a function of the ferromagnetic layer thickness. There is clear transition around 2 nm where the film becomes more ferromagnetic since $H_k$ decreases and sq increase sharply.

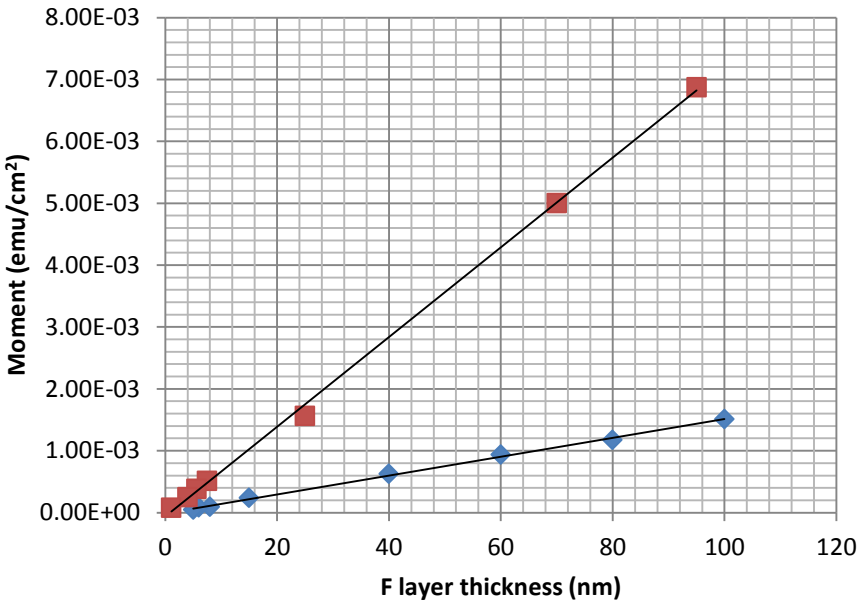


Figure 66. Magnetic moment per unit surface area versus the ferromagnetic layer thickness for Nb/$Ni_{81}Fe_{19}$, and Nb/ $Pd_{87}Ni_{13}$ bi layer structures

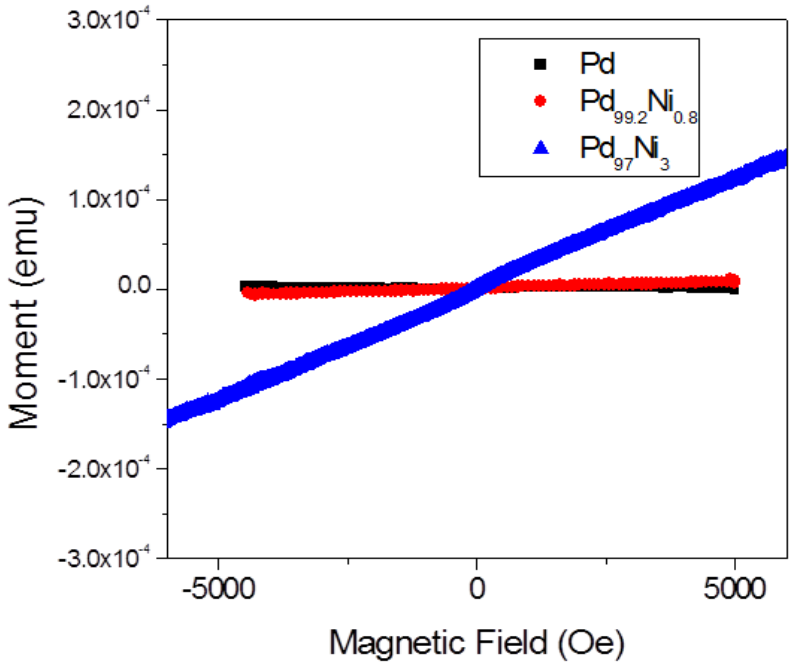

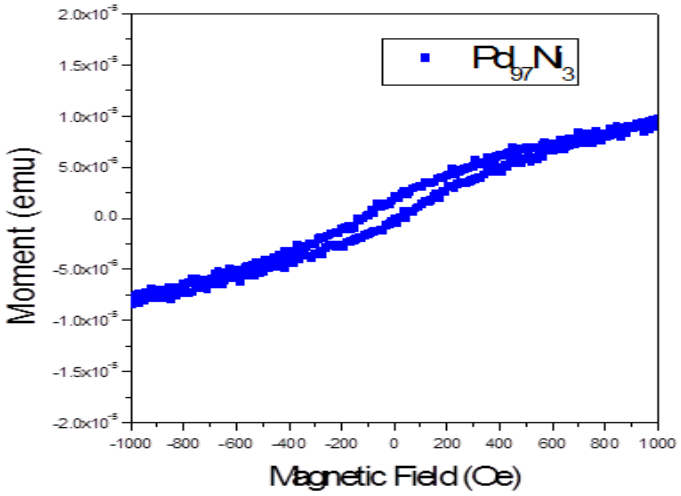


Figure 67. (Top) Magnetic moment versus applied filed for $Nb/Pd_{1-x}Ni_x$ bilayers where (x= 0, 0.8 ans 3 %) (Bottom) Magnetic moment versus applied filed for $Nb/Pd_{97}Ni_3$ bilayers

6.4.2 S/F bi-layers with F= $Ni_{65}Fe_{15}Co_{20}$, $Ni_{81}Fe_{19}$, and $Pd_{87}Ni_{13}$

Resistive transitions for $Nb/Pd_{87}Ni_{13}$ bi layer samples are presented in Figure 68. The transition width, as defined by the 10-90% of $R_n$ at just above the transition temperature, for all investigated samples discussed in this paper was not more than 0.05 K. The residual resistivity ratio ($RRR=\rho_{300\ K}/\ \rho_{10\ K}$) was in the range of 2-2.3, varying within each series no more than 3 %.

Figure 69 displays the $T_c$ behavior for $Nb/Ni_{65}Fe_{15}Co_{20,}$ $Nb/Ni_{81}Fe_{19}$, and $Nb/Pd_{87}Ni_{13}$ bilayers as a function of thickness $d_F$ with fixed thickness of Nb, 40 nm. As the data shows, the $T_c$ of the bilayers decreases non-monotonically from critical temperature $T_{cs}$ of a single Nb layer with increasing thickness until it reaches about 1.5, 2.2 and 2.8 nm for the three bilayer systems for $Nb/Ni_{65}Fe_{15}Co_{20,}$ $Nb/Ni_{81}Fe_{19}$, and $Nb/Pd_{87}Ni_{13}$ respectively, and then increases slightly to approach a restrictive value,

resulting in a shallow dip feature of about 0.3-0.4 K, well above our measurement system resolution.

The minimum in $T_c$ with layer thickness scales with magnetic strength of the ferromagnetic layer in each of the bilayer systems .It's clear that the stronger the magnetic properties (high $M_s$, high $T_{Curie}$) the earlier the dip appears (at small thicknesses $d_F$) [143]. This is expected, given that the $T_{Curie}$ and thus resulting $E_{ex}$for $Ni_{65}Fe_{15}Co_{20,}$>$Ni_{81}Fe_{19}$, > and $Pd_{87}Ni_{13}$. To estimate the exchange energy from the $T_c$ bi-layers we used a modified diffusive formula $\xi_F = d_{Fmin} = \pi/2$ sqrt($\hbar D_F/E_{ex}$)[121b]. Using this formulism we estimate the exchange energy for three bi -layer systems to be 135 meV, 110 meV, and 27 meV for $Ni_{65}Fe_{15}Co_{20,}$ $Ni_{81}Fe_{19}$, and $Pd_{87}Ni_{13}$ respectively, similar in their values to earlier reported results for $Ni_{81}Fe_{19}$ [99] and $Pd_{87}Ni_{13}$ [102]. The exchange energies determined from our values are close to the ones calculated using the mean field theory approximation $E_{ex}= K_BT_{Curie}$ .We attempted to analyze this data using the method described by Fominov in [121b] based on the Usadel formalism. In that model, only the influence of exchange field was included, while spin-flip scattering was not considered.

To fit our the data of our bi layer structures as a function of $Ni_{81}Fe_{19}$ thickness, we first determined the resistivity values for each layer $\rho_{Nb}$= 18μΩ-cm, $\rho_{Ni81Fe19}$= 20 μΩ-cm, and the superconducting critical temperature for single 40 nm thick Nb was $T_{cs}$=8.4 K from distinct single experiments. By setting these parameters constant, we obtained the following parameters from the fitting of the dirty limit coherence length of superconductor and ferromagnetic metal $\xi_s$ =sqrt($\hbar D_s/2\pi\kappa_B T_{cs}$) and $\xi_F$ =sqrt($\hbar D_F/2\pi\kappa_B T_{cs}$).

The parameters which characterize the interface resistance between the S and F layer metals $\gamma_b=R_bA/\rho_f\ \xi_{F,}$ where Rb*A is the resistance at the S/F interface, and the exchange energy of the ferromagnetic layer $E_{ex.}$ According to the model, the $E_{ex}$ value is mostly determined by the layer thickness which results in the minimum in $T_c$. The parameter with the most influence on the saturated $T_c$ values is $\gamma_{b.}$ Figure 70 shows the Nb/ $Ni_{81}Fe_{19}$, Tc data, with the solid line representing the Forminov model fit.

The $T_c$ of Nb/ $Ni_{81}Fe_{19}$, bilayers as a function of the ferromagnetic layer thickness was also fitted with the following parameters $\xi s$= 7.8 nm $\xi_F$= 5 nm , $\gamma b$= 0.85 and $E_{ex=}$ 99.4 meV. The exchange energy is comparable to the value we calculated from the modified diffusive formula mentioned above, and it's close to the value we received from our and others previous work on Nb/ $Ni_{81}Fe_{19}$/Nb junctions [75, 99]. This is because the $E_{ex}$ value is obtained from the dip in $T_c$, which falls far away from the thicknesses associated with chemical intermixing, the dead layer and the completion of layer coalescence. We must mention that higher $E_{ex}$ magnetic materials with an approximated dip in less than 1 nm may be hard to obtain since the dip value will be convoluted with the dead layer and intermixed magnetic state.

We estimate the mean free path of the Nb film from the coherence length $\xi s$ to be $l_{mfp}$= 3.8 nm using the following equations for a dirty limit metal $\xi_s$ =sqrt($\hbar D_s/2\pi\kappa_B T_{cs}$), the diffusion constant $D_S= v_{F*}\ l_{mfp}/3$, and the Fermi velocity $v_F$= 0.56 x$10^6$ m/sec [22b]. We then obtained $(\rho\ l_{mfp})_{Nb}$= 6.84 x$10^{-16}$ $\Omega m^2$, which is comparable to the value in reference [151]. The interface resistance at the S/F interface can be estimated from $\gamma b$ is

to be $R_bA$= 8.5 x$10^{-12}$ Ωcm$^2$. This value can be comparable to the resistance interface between two metals [144]

Although our $T_c$ data for the Nb/ $Ni_{81}Fe_{19}$ bilayers can be fit, the results show a higher value of $T_c$ for thin ferromagnetic layer coverages over that of thick coverages. This discrepancy can be explained by the suppression of magnetism for thin ferromagnetic films coverages as a result of the reduced exchange energy, as a result of the inhomogeneities, such as islanding and chemical intermixing, that occur during the initial stages of film growth caused by the magnetic dead layers. Such affects were not quantitatively addressed in Reference [121b]. In our work, we observe a change in slope in the Tc versus ferromagnetic layer thickness at the same value as the dead layer thickens, i.e. when the material transitions from being non-ferromagnetic to ferromagnetic.

It's clear the Fominov model does not describe our data well. So, we attempt to fit the data with a damped oscillator, as is found in S/F proximity theory. The equation used is $\psi=\psi_0 \exp(-(x-x_{of})/\xi_{F1}) \exp(-i((-(x-x_{of})/\xi_{F2})$, where $\psi_0$ is the initial amplitude , x is the ferromagnetic layer thickness, $x_{of}$ is an offset to account from dead layer, and $\xi_{F1}$ is the sum of the two components $\xi_{F1=}\ \xi_{1spin+}\ \xi_{1Eex}$ ( taking into account both spin flip and exchange as pair breaking mechanism in the decay length) and $\xi_{F2}$ is the oscillating length resulting only from the effect of the exchange energy .

In our grown structures, the RMS roughness of the thin ferromagnetic layers was so small that we did not expect a substantial suppression of $T_c$ for thin coverages from the interface roughness. According to our AFM scans, the surface RMS roughness of single 40 nm Nb is 0.3 nm, and the RMS roughness value for thick ferromagnetic layer on 40 nm Nb is 0.5-0.6 nm. The influence of band matching and the presence of a strong-

scattering alloy region near the interface could be responsible for the large interface resistance $\gamma_b$ . However, because the relatively small value found for $\gamma_b$= 0.85 and 0.48 in Nb/$Ni_{81}Fe_{19}$, and Nb/$Pd_{87}Ni_{13}$ respectively, this would suggest less scattering as a result of improved band matching and less intermixing. Our RBS measurement and analysis did not indicate significant intermixing that the interface in the S/F bilayers.

Figure 71, shows the data and analytic fits for both, Nb/$Ni_{81}Fe_{19}$, and Nb/$Pd_{87}Ni_{13}$ bi-layer systems. The data fit very well in the entire thickness regime. Analysis shown the two lengths $\xi_{F1}$ and $\xi_{F2\ are}$ not equal, inconsistent with the Fominov model. This suggests that spin-flip scattering is present as a pair breaking mechanism. The values we got from this fit for $\xi_{F1}$= 1.3 nm and $\xi_{F2}$= 0.636 nm for $Ni_{81}Fe_{19,}$ and since they are not equal, so we can introduce a spin-flip pair breaking mechanism with a characteristic decay of $\xi_{1spin}$=0.66 to account for this increase in $\xi_{F1.}$ For $Pd_{87}Ni_{13}$ for $\xi_{F1}$= 1.6 nm and $\xi_{F2}$= 0.716 nm, so we infer $\xi_{1spin}$ to be 0.883 nm.

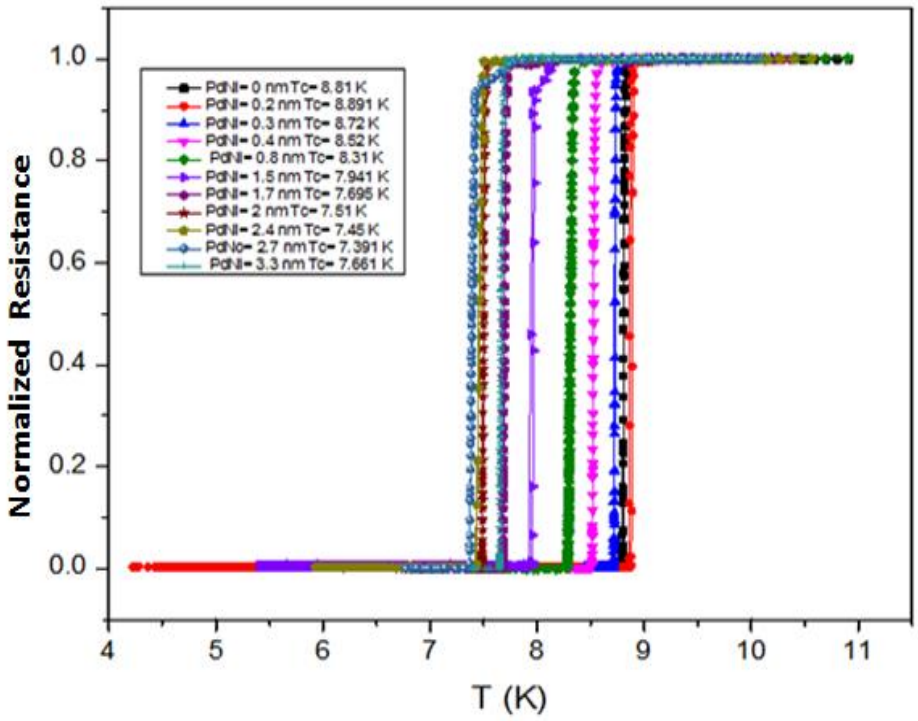


Figure 68. Resistive transition R (T) normalized to R (10 K) for Nb( 40 nm)/$Pd_{87}Ni_{13}$ bi layer samples

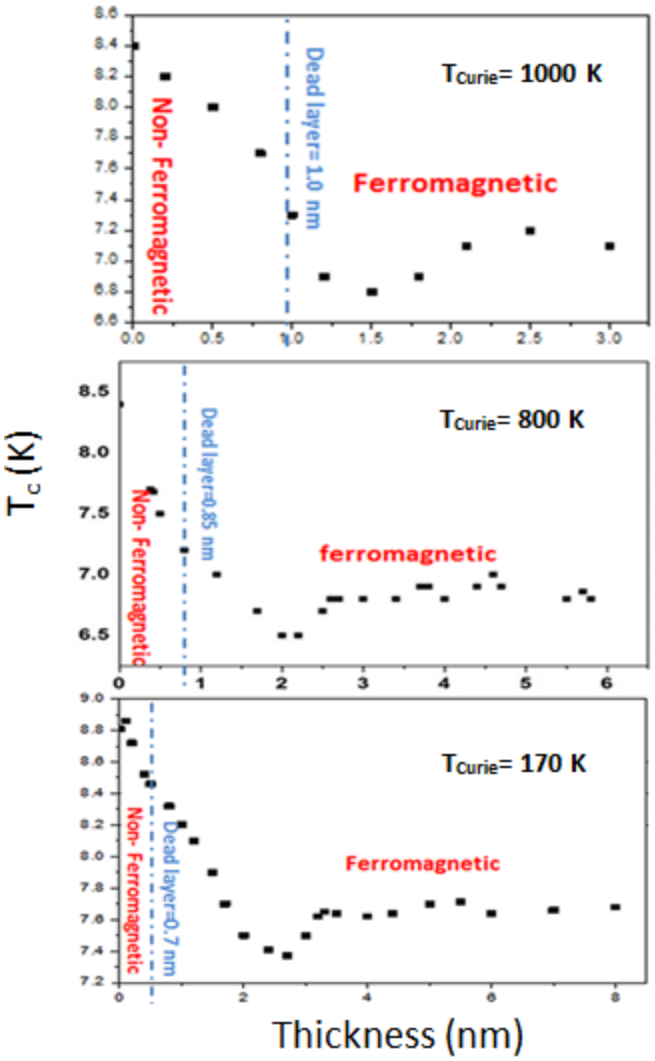


Figure 69. Tc of bilayers as a function of the ferromagnetic layer –layer thickness for (a) $Nb/Ni_{65}Fe_{15}Co_{20}$ with minima at 1.5 nm, (b)$Nb/Ni_{81}Fe_{19}$ with minima at 2 nm, and (c) $Nb/Pd_{87}Ni_{13}$ with minima at 2.8 nm

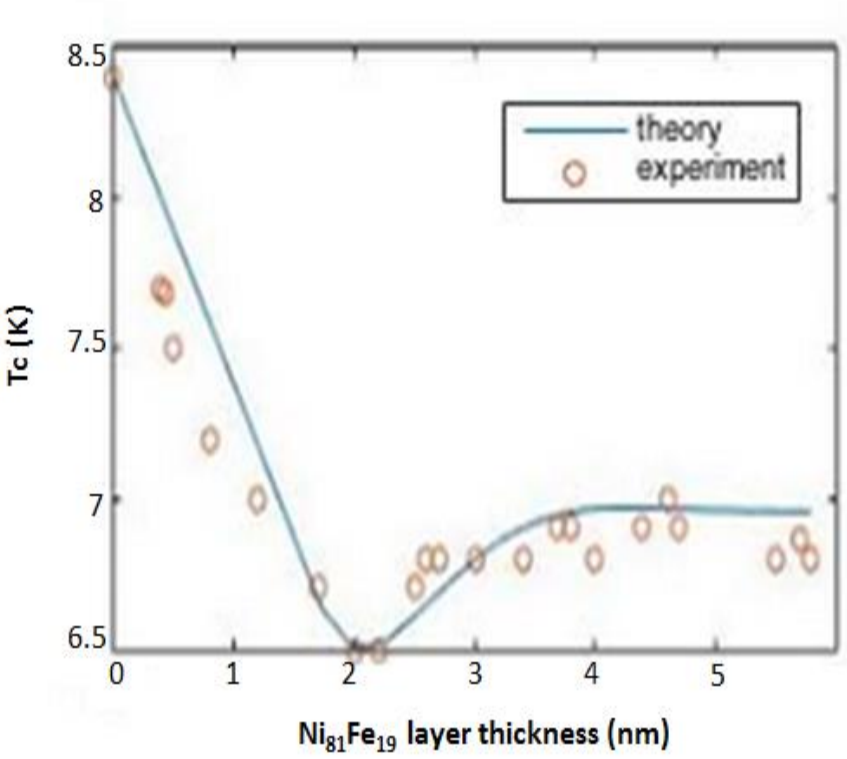


Figure 70. $T_c$ of Nb (40 nm)/ $Ni_{81}Fe_{19}$ ($d_F$ nm),bilayers as a function of the $Ni_{81}Fe_{19}$ thickness (Symbols) The solid line is fit result using [25]

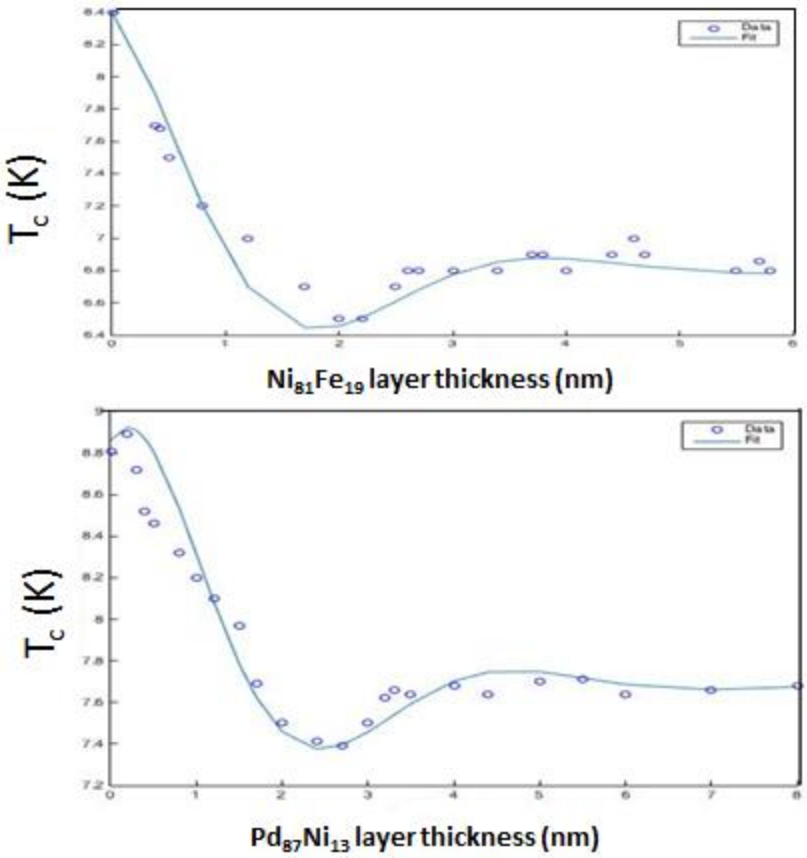


Figure 71. Damped sinusoidal fit for both, $Nb/Ni_{81}Fe_{19}$, and $Nb/Pd_{87}Ni_{13}$ bi-layer systems .

6.4.3 S/F bilayers with F= $Pd_{1-x}Ni_x$ alloys with (X= 0, 0.8 and 3 %)

To probe the bilayer properties of different types of layers, we chose to first investigate bilayers with Pd, a paramagnetic metal. Then by alloying with Ni, we can study how its transition from paramagnetic (spin fluctuation regime) at 0-2.5 % to the onset of ferromagnetism at 3% Ni [142] influences the bilayer properties.

In Figure 72, the critical temperature is reported as a function of the Pd thickness $d_{Pd}$ for the bilayers. Figure 72 (Top) figure shows the critical temperature for Nb (40 nm)/

Pd bi-layer and Figure 72 (bottom) figure shows the critical temperature for Nb (40 nm)/$Pd_{99.2}Ni_{0.8}$ bi-layer. Both data sets show a monotonic $T_c$ behavior .The data can be can be tentatively analyzed in the framework of the de Gennes-Werthamer theory [145,146] using the implicit expression, $K_s*\tan( K_s d_s/2)=(\rho_s/\rho_N)*K_N*\tanh(( K_N d_N/2)$, where $\rho_S$ and $\rho_N$ are, respectively, the low temperature resistivities of the superconductor and of the normal metal, $k_S=(2/\pi\xi_s)$`sqrt$[(T_{cS}/T_c)-1]$ and $k_N=1/\xi_N$ with $\xi_s$ =sqrt$(\hbar D_s/2\pi\kappa_B T_{cs})$ and $\xi_N$ =sqrt$(\hbar D_N/2\pi\kappa_B T_{cs})$,. Therefore the quantities $k_S$ and $k_N$ contain, in addition to the critical temperature of the multilayer $T_c$ and of the bulk superconductor $T_c$s, the diffusion constants for the superconductor and for the normal metal $D_{S,N}=(1/3)\ v_{(S,N)}*l_{mfp(S,N)}$ .

The solid lines reported in Figure 72 has been obtained using the implicit expression mentioned above with $T_{c,S}= T_{c,Nb}=8.65$ K, $v_{S=(Nb)}=2.73x10^7$cm/sec , $v_{N=(Pd)}= 2.0x10^7$cm/sec [22b]. The resistivity values $\rho_s=18\mu\Omega$-cm and $\rho_N=5.7\ \mu\Omega$-cm and 8.6 $\mu\Omega$-cm for both Pd and $Pd_{99.2}Ni_{0.8}$ have been evaluated, using the standard 4 point measurements. The mean free path values were also evaluated to be $l_{mfp(S)}$ = 5 nm for Nb and $l_{mfp(N)}$= 15 nm and 12.5 nm for both Pd and $Pd_{99.2}Ni_{0.8}$ . Finally the values for superconductor and metal coherence lengths left as free parameters. In the case of Nb/Pd bi layer set, we obtained a metal coherence length $\xi_N$= 12.1 nm and superconductor coherence length $\xi_S$=4.2 nm. In the case of Nb/$Pd_{99.2}Ni_{0.8}$ bilayers we obtained a decreased metal coherence length $\xi_N$= 7.7 nm and same superconductor coherence length $\xi_S$= 4.2 nm. The noticeable drop in the metal coherence lengths is attributed to the spin flip scattering from the Ni dopants in the Pd matrix. Figure 73, shows the Tc behavior a

non-monotonic behavior in the case of Nb (40 nm)/ $Pd_{97}Ni_3$ . Surprisingly, we find that the $T_c$ has a shallow minimum in the Tc versus PdNi layer thickness, similar to that found for a ferromagnetic metal. Correlating this to our magnetic characterization of the three bi layer data sets of Nb/Pd , Nb/ $Pd_{99.2}Ni_{0.8}$ and Nb/ $Pd_{97}Ni_3$, where the M-H loops measured at 10 K show a transition from the diamagnetic dominated signal to a more superparamagnetic like signature behavior (small hysteresis but no saturation even at higher fields). Clearly we can conclude that if the magnetic material being probed in the bi layer is not ferromagnetic, it will not have a minimum as predicted, and if its weakly ferromagentic it will have a minimum at a very large thickness of $d_F$. Figure 74, summarizes the results we obtained for all $Pd_{1-x}Ni_x$ alloys with (X= 0, 0.8, 3 and 13 %). It can be clearly seen that for films with thick PdNi layers, the measured Tc values for the does not decrease as Ni content increases as in the case for the 3 % Ni bi layer data. This is not understood yet, and further studies need to be done to investigate the reasons.

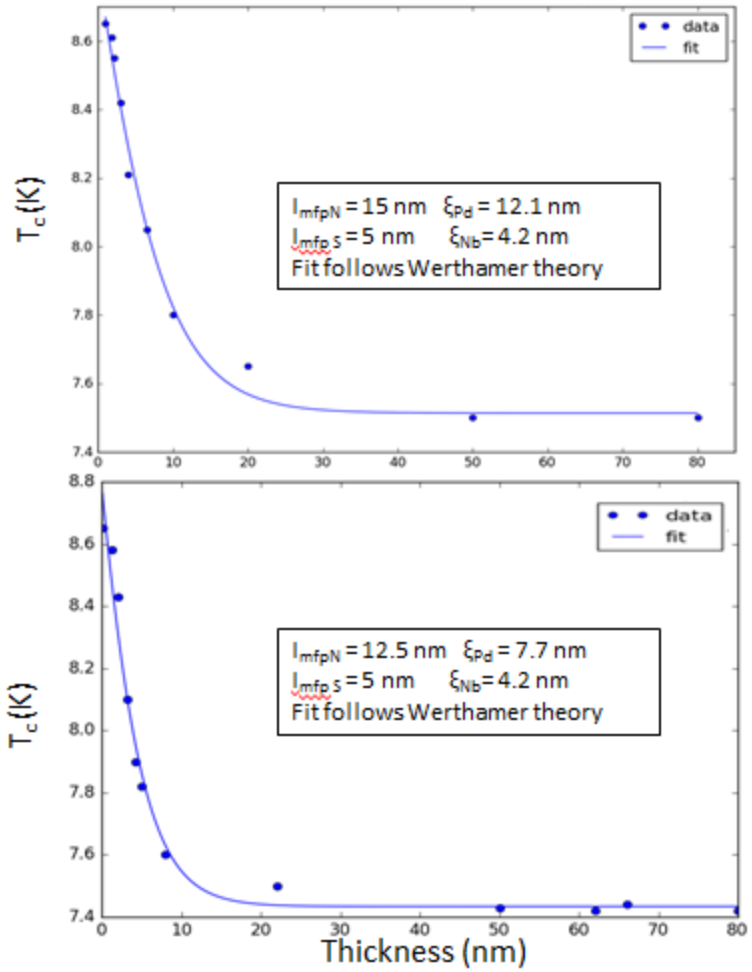


Figure 72. $T_c$ of bilayers as a function of the ferromagnetic layer –layer thickness for (Top) Nb(40 nm)/ Pd and (bottom) Nb(40 nm)/ $Pd_{99.2}Ni_{0.8}$. $T_c$ shows a monotonic behavior for both systems.

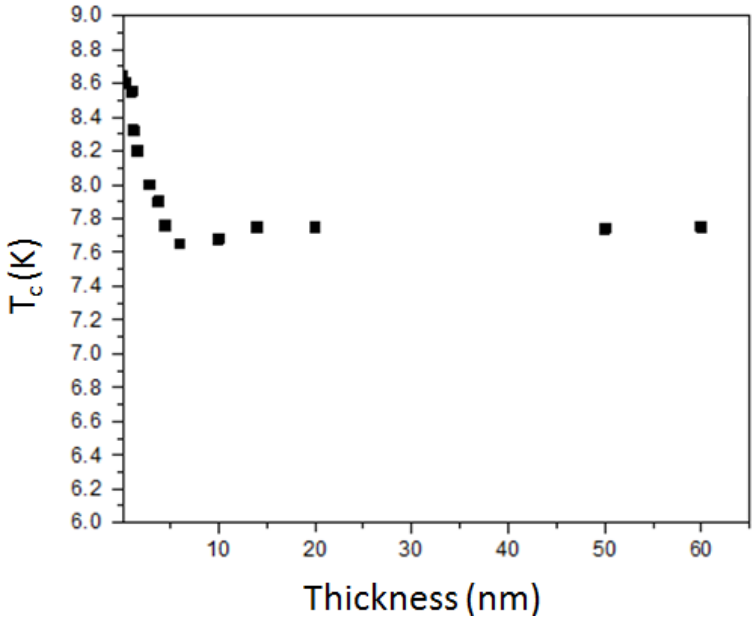


Figure 73. $T_c$ of bilayers as a function of the ferromagnetic layer –layer thickness for Nb(40 nm)/ $Pd_{97}Ni_3$ $T_c$ shows a non- monotonic behavior with a minima at 8 nm.

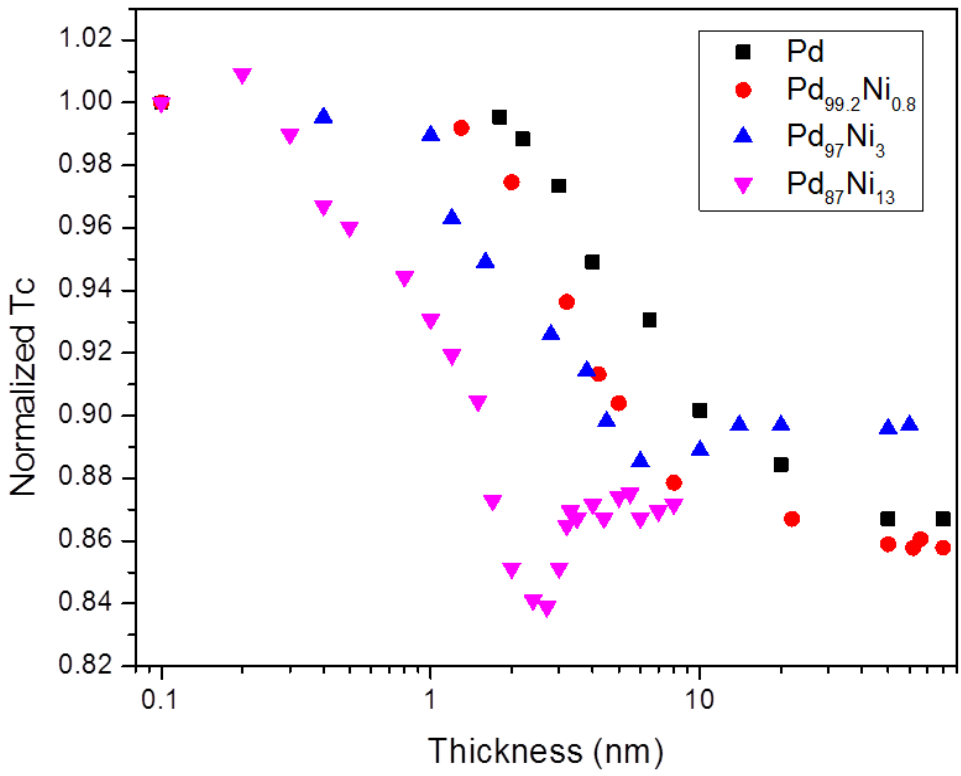


Figure 74. Semi-log plot of $T_c$ of bilayers as a function of the ferromagnetic layer –layer thickness for Nb(40 nm)/ in $Pd_{1-x}Ni_x$ alloys

6.4.4 DOS in S/F/I/N junctions with F= $Pd_{87}Ni_{13}$

In this section, we present a density of state spectroscopy study using an aluminum oxide tunneling junction located on the ferromagnetic layer side of a Nb/ $Pd_{87}Ni_{13}$ bilayer. The critical temperatures of bi-layer for this system are shown above, where a dip at $d_F$=2.8 nm is noticeable. A quantitative analysis of these data based on the Usadel Equations and Fominov fit gave a value of 27 meV for the exchange field $E_{ex}$ and 0.48 for the interface resistance parameter $\gamma_b$ which is fairly transparent. The geometrical parameters for the above simulation differ from our junctions. In those results, a thicker Nb layer 100 nm. We performed tunneling spectroscopy on samples with thicknesses ranging from 0 to 4.5 nm in increments of 0.5 nm.

Figure 75 shows a typical SIN junction without a ferromagnetic barrier measured at 4.2 K. Figure 75 (Top) shows the IV of such junction along with DOS in Figure 75 (Bottom). The results show a well-defined gap at 1.3 mV .Figure 76 shows the resulting curves for all measured thicknesses. As the ferromagnetic layer ($Pd_{87}Ni_{13}$) becomes thicker, the tunneling spectrum is abruptly altered with substantial conductance below the gap energy. As $d_F$ increases further, the superconducting features in the tunneling conductance are strongly attenuated, decreasing the pair amplitude strength. These results clearly indicate that as we increase the ferromagnetic layer thickness more and more cooper pairs are broken and only few make it to the $Pd_{87}Ni_{13}$ /Al interface.

The most striking observation, though, is that between 0 and 3.5 nm the spectra can be rescaled onto a single curve by applying a multiplicative factor to all data point as shown in Figure 77. The multiplicative scaling factor is plotted as a function of the ferromagnetic layer thickness. The straight line is an exponential fit of the data, which suggests that our scaling coefficient is given by A(df)= e^-$d_F/\xi_F$, where $\xi_F$= 0.88 nm. The remarkable fact that A($d_F$) does not extrapolates to 1 as $d_F$. It offers evidence that possibly there is a region where Cooper pairs are not broken. We also attempted to infer the decay length of such pair amplitude. From the normalized dI/dV - V, we integrated the dip below the line at 1.0, then the two peaks that are above 1.0 in the two voltage directions. These areas were accurately measured to 5%. These results are plotted in Figure 78**.** The difference in $\xi_F$ decay lengths between the bi-layer study and tunnel study is not fully understood.

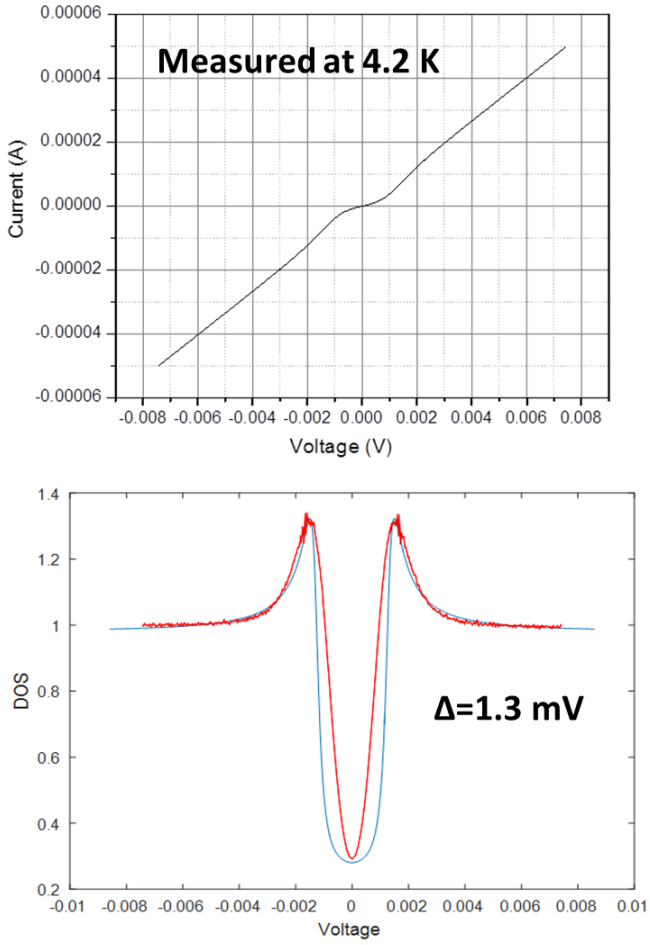


Figure 75. (Top) I-V measurements of Nb/Al/$AlO_X$/Al SIN junction measured at 4.2 K. (Bottom) Corresponding DOS of the SIN junction

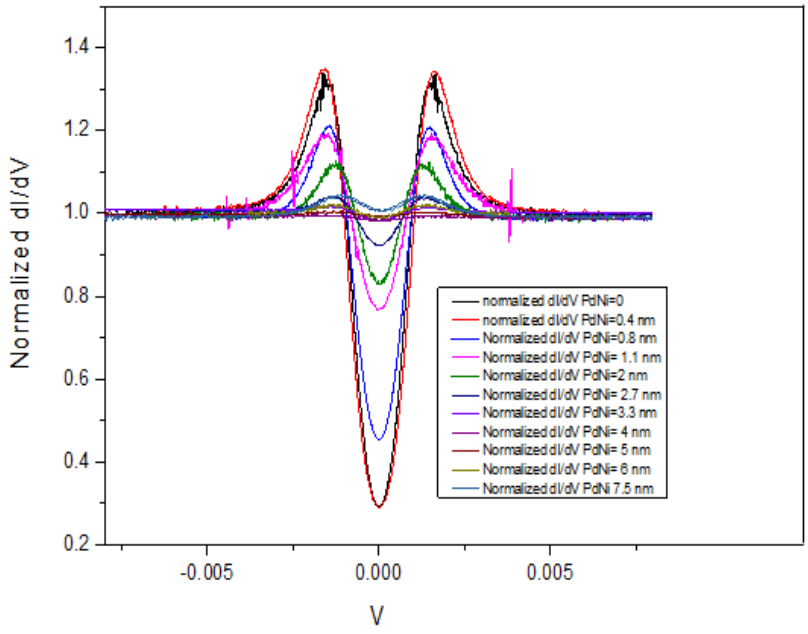


Figure 76. DOS vs $Pd_{87}Ni_{13}$ thickness in S/F/I/N tunnel junctions

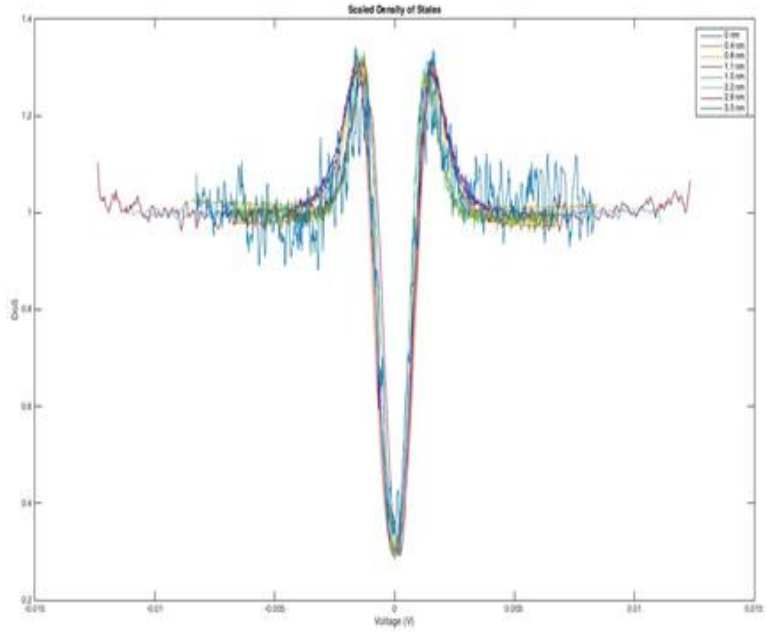

Figure 77. Superposition of eight scaled conductance curves for $d_F$= 0.4-3.5 nm The 0 thickness $Pd_{87}Ni_{13}$ was taking as the scaling upper-limit

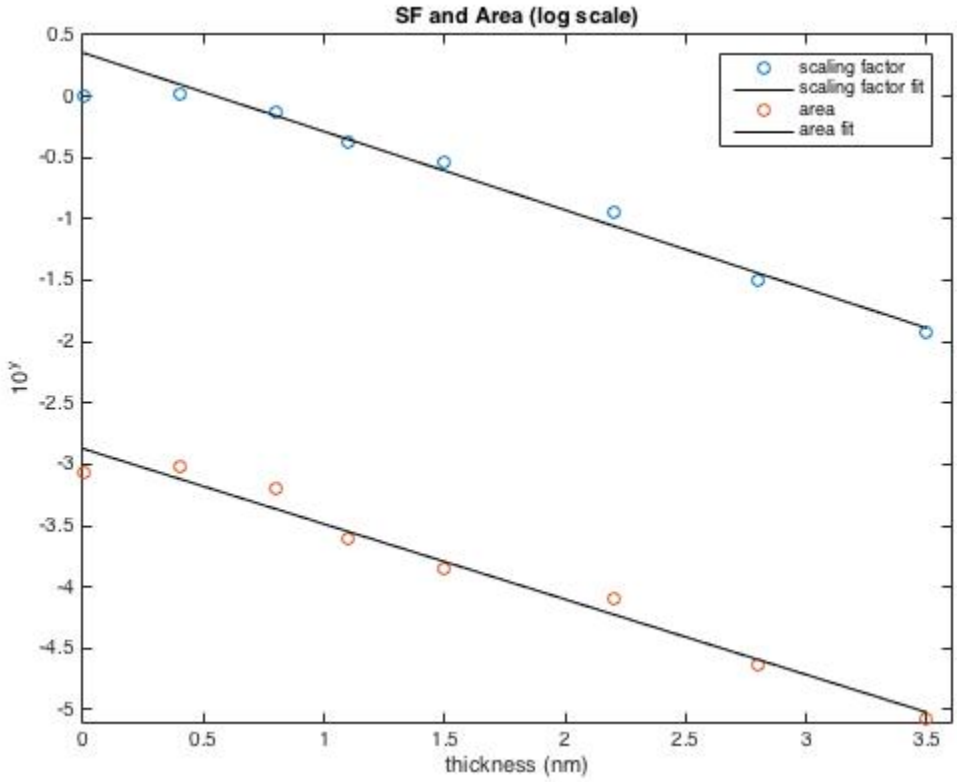


Figure 78. Semi-log plot of the scaling factor and pair number plotted as a function of $Pd_{87}Ni_{13}$thickness

6.5 Conclusion

In summary, we have presented the Tc of bilayers as a function of ferromagnetic layer thickness for three sets of different ferromagnets. The non-monotonic $T_c$ characteristics were observed in several sets of samples. The data could be fit using a damped exponential, as predicted by the FFLO theory. For PdNi, where the $T_c$ minima occurs at a region significantly thicker than the dead-layer and other interface effects, the bilayer data indicated a $\xi_{F2=}$ 0.7 and could not accurately fit $\xi F_1$. However, $\xi F_1$ could be

accurately measured using the tunneling density of states work to be 0.88 eV. By changing the amount of Ni alloying level the $Pd_xNi_{1-x}$ alloys, we measured the critical transition temperature in three different regimes. This allowed us to determine the influence on the properties of bilayers with magnetic layers comprised of (1) a paramagnetic layer, (2) paramagnetic layer with random spins, (3) ferromagnets with a small exchange energy and larger exchange energy. $T_c$ minima for increasing layer thicknesses were only found for the latter 2 cases, when the layer was ferromagnetic.

# Chapter 7 CONCLUSIONS AND FUTURE WORK

## 7.1 Conclusions

### 7.1.1 Study of $Cu_{1-x}(Ni_{80}Fe_{20)x}$ magnetic systems

The first step of this thesis research was to investigate different materials as candidates for low $M_s$ and $T_{curie}$ ferromagnetic soft layer.

Therefore, the magnetic, chemical and electrical properties of $Cu_{1-x}(Ni_{80}Fe_{20})_x$ thin films were measured. $Cu_{1-x}(Ni_{80}Fe_{20})_x$ alloys with x greater than 25 % are found to be ferromagnetic. $M_s$ and $T_c$ of these materials are found to scale linearly with permalloy content. Alloys with x between 12% and 25% are found to exhibit superparamagnetic behavior. Copper-permalloy alloys are found to have a much higher resistivity than permalloy because of the significantly larger scattering of the majority spin channel. From these observations, we can conclude that $Cu_{1-x}(Ni_{80}Fe_{20})_x$ alloys appear to be attractive weak ferromagnetic materials for use in low temperature magnetoelectronic applications. We have used $Cu_{70}(Ni_{80}Fe_{20})_{30}$ alloy for the free "soft layer" in devices developed in the JMRAM cell in structures like S/F/N/F'/S .

### 7.1.2 Characteristics of Josephson junctions with ferromagnetic barrier

This project comprises development of the fabrication process and material optimization. We first develop the fabrication process of the JMRAM device structure supporting high $T_c$ Nb electrode and etch recipes that are comparable with existing MRAM fabs. It is imperative that the superconductor order parameter drop a relatively small amount while traversing through the magnetic layers, so that it is maintained up to

the interface with the barrier. The value of this parameter right at the metal/ferromagnetic barrier interface and the barrier thickness determines the magnitude of the Josephson current, $I_c$. Thus, the magnetic layers must be sufficiently thin to allow this, on the order of 1-2 nm, while still being thick enough to maintain their stability against thermal switching. By using a dilute Cu-permalloy alloy with low saturation magnetizations (~80 emu/cm$^3$) as a free layers and permalloy with a high saturation magnetic field (~800 emu/cm$^3$) into Nb-based Josephson junctions, we have demonstrated that a JMRAM device structure can be fabricated with a small onset switching field. A 2.4 nm thick permalloy fixed layer was used to shift the phase of the wavefunction to the $\pi/2$ pivot point. The accuracy with which the permalloy layer thickness and uniformity can be controlled will determine the minimum phase-shift required from the free layer to provide reliable switching, and finally to control Josephson currents in this structure, all of the layers must be uniform in thickness and smooth, while the interfaces must be sharp without significant intermixing

The feasibility of the JMRAM concept is substantiated by the recent progress in this thesis research work by successfully manipulating the superconducting critical current as it transverses through thin magnetic layers by their magnetization as shown in this thesis work. Most importantly, it has been shown that an SFNFS Josephson structure with a proximity barrier has a hysteretic critical current that tracks the hysteresis in the magnetization of the free layer with a large magneto-current ratio above 100%, This approach warrants consideration because of the potential for ns switching times, switching fields $H_{sw}$ ~order 10's of Oersteds (and corresponding switching currents of 0.1

mA), Josephson magneto-current ratios of over 100% between the high/low memory states, high read/write endurance and sufficient stability of the memory state at 4.2 K. The memory devices reported here demonstrate nonvolatile, low energy switching characteristics.

### 7.1.3 Proximity effect study in superconductor/ferromagnetic structures

To further investigate the drop of the superconducting order parameter in S/F/N/F'S structures we investigated the superconducting order parameter behavior fabricating S/F bi layer structures and measuring their corresponding $T_c$. This study allowed us to better understand the decay of the order parameter in S/F structures and to observe the thickness of the F-layer where the 0 to $\pi$ shift occurs. Also by fitting the data to simple models we were able to extract crucial parameters like exchange decay length $\xi_F$, exchange energy $E_{ex}$ of the studies magnetic materials, and interface resistances.

We have observed a non-monotonic $T_c$ behavior in our S/F bi layer study, and we correlated the minima in $T_c$ to the magnetic strength of the F layer. We further examined how spin flips shorten the decay length and how ferromagnetic order does correlate the non -monotonic behavior observed.

## 7.2 Future work

### 7.2.1 Optimization of the JMRAM S/F//N/F'/S structures

To better optimize the operation of the proposed JMRAM memory cell the following tasks can be done:

1) Enhance the switching properties of the ferromagnetic layers included in the JMRAM cell, by optimizing the smoothness of the interfaces and the bottom Nb seed layer (bottom electrode) where on top it the stack is grown. Our preliminary work has shown that smooth under-layers affect for the better, the ferromagnetic dead-layer thickness and it does affect the switching energies and distributions.
2) Improve the fabrication process of the JMRAM cell, by aiming for smaller dimension fabricated JMRAM cells. Since Permalloy NiFe alloys have typically a domain size of about 1 micron, fabricating JMRAM devices with dimensions less than 1 micron square will ensure that the magnetic layers are found to be in the single domain regime, ensuring a better magnetic and electrical switching.

### 7.2.2 Further study of the decay length in S//F/I/N tunnel structures.

Since some of the results we observed were controversial in the case of measured decay length in S/F/I/N structures with F being $Pd_{87}Ni_{13}$, and we contribute that two factors. One is that the access unreacted Al in proximity with the F and the S layers caused an additional drop of the order parameter causing a further reduction in the exchange decay length due mainly from the F layer. Also the heavy intermixing has shown by TEM between the F and Al layer causes a much more inter-diffused / intermixed region where the order parameter scatters more. To avoid such region effect on the order parameter, another set of tunnel proximity structures are urged to be fabricated and tested.

1) Fabricate tunnel proximity structures where the unreacted Al is on the bottom side. This done by first growing the Al bottom seed layer of 50 nm thick to ensure it smooth enough at these thickness, then oxidize it using O2 gas in the load lock. Then grow the rest of the structure on top of it, with first F layer and second the superconducting Nb layer. Final structures should be in the following order N/I/F/S. In these structures the order parameter will be probed only through the F layers, and any effect seen will be mainly due to any changes in the F layer.

# REFERENCES


[1] B.D Josepshon, “Possible new effects in superconductive tunneling,”Phys.Lett., vol.1, pp.251-253,July 1962

[2] P.W. Anderson and J.M. Rowell, “Psoosible observation of the Josephson supercndcuting tunneling effect,” Phys. Rev. Lett. Vol.10, pp.230-232, March 15, 1963.

[3] J.M. Rowell, M. Gurvitch, and J.Geerk, “Modification of tunneling barriers on Nb by a few monolayers of Al,” Phys. Rev. Lett. Vol.24, pp.2278-2281, 1981.

[4] D.K. Brock, E.K. Track, and J.M. Rowell,” Superconductor IC’s:100-GHz second generation,” IEEE Spectrum, December 2000.

[5] K. K. Likharev and V. K. Semenov, "RSFQ logic/memory family: a new Josephson-junction technology for sub-terahertz-clock-frequency digital systems," in IEEE Transactions on Applied Superconductivity, vol. 1, no. 1, pp. 3-28, March 1991.

[6] D. Gupta, T. V. Filippov, et al, IEEE Trans. on Appl. Supercond. 17, 430 (2007).

[7] A. Herr, IEICE Transactions on Electronics E91-C(3), 293-305, (2008).

[8] N. Miyaho, A. Yamazaki, T. Sakurai, K. Miyahara , Commun.s, 2006. APCC '06, (2006).

[9] Superconducting Technology Assessment, http://www.nitrd.gov/pubs/nsa/sta.pdf

[10] A.F. Kirichenko, S. Sarwana, D.K. Brock, and M. Radpavar, IEEE Trans. Appl. Supercond. 11, 537 (2001)

[11] Q. P. Herr and L. Eaton, Supercond. Sci. Technol. 12, 929–932 (1999)

[12] T. Van Duzer, Y. Feng, X. Meng, S.R. Whiteley, and N. Yoshikawa, Supercond. Sci. Technol. 15, 1669 (2002)

[13] A. Herr, Q. Herr, “Josephson magnetic random access memory system and method,” U.S. Patent, No. 8,270,209 B2, Sep. 2012

[14] Bruce F. Cockburn, 2004 International Workshop on Memory Technology, Design and Testing (MTDT’04)

[15] C. Bell, G. Burnell, C. W. Leung, M. G. Blamire, Appl. Phys. Letters 84, 1153 (2004).

[16] V. Ryazanov, private communication, InQubit Inc., CA.

[17] Q.P. Herr, A. Smith, M. Wire, Appl. Phys. Lett. 80, 3210 (2002).

[18] T. Van Duzer and C. W. Turner, "Principles of Superconductive Devices and Circuits", 2nd Edition, Prentice Hall PTR, New Jersey (1999)

[19] .karmerlingh Onnes, Leiden Comm. 120b, 120b, 124c (1911).

[20] Meissner, W. and R. Bochsenfeld, Ein neuer Effekt bei Eintritt der Supraleitfähigkeit. Naturwissenschaften 21 (44): 787–788 (1933).

[21] <http://global-sei.com/super/about_e/feature.html>

[22a] J. Bardeen, L. N. Cooper and J. R. Schieffer, "Theory of Superconductivity", Phys. Rev. 108, 1175 (1957)

[22b] N. W. Ashcroft and N. D. Mermin, "Solid State Physics", chapter 2, Thomson Learning, Inc. (1976)

[23] Kittel, Introduction to Solid State Physics, 5th Edition, John Wiley & Sons, Inc. (1976).

[24] S.O.Kasap principles of electronic materials and devices 3rd edition MacGraw Hill (2006)

[25] John Clarke, "The proximity effect between supercondcuign and normal thin films in zero field" Journal de Physique Colloques, 29 (C2), pp.C2-3-C2-16 1968.

[26]<https://www.ndeed.org/EducationResources/CommunityCollege/MagParticle/Physics/HysteresisLoop.html>

[27] Charles P. Poole Jr., Horacio A. Farach, and Richard J. Creswick, Superconductivity, Academic Press, Inc. (1995).

[28] Andreev, A. F. "Thermal conductivity of the intermediate state of superconductors". Sov. Phys. JETP 19: 1228. (1964)

[29] P.G. de Gennes, Boundary Effect in Superconductors, Rev. Mod. Phys., vol. 36, pp. 225-237 (1964).

[30]http://www.intechopen.com/books/superconductors-new-developments/spintronics-driven-by-superconducting-proximity-effect

[31] I. Buzdin, Rev. Mod. Phys. 77, 935 (2005).

[32] W. A. Robinson,S. Piano,G. Burnell, C. Bell, and M. G. Blamire . Critical Current Oscillations in Strong Ferromagnetic p Junctions. Phys. Rev. Lett. 97, 177003 (2006)

[33] Trupti S. Khaire, Ph.D. thesis, Michigan State University, USA, 2010.

[34] J. Robinson, S. Piano, G. Burnell, C. Bell, and M. G. Blamire, Phys. Rev. B 76, 094522 (2007).

[35] M. Weides, M. Kemmler, E. Goldobin, D. Koelle, R. Kleiner, H. Kohlshedt, and A. Buzdin, Appl. Phys. Lett. 89, 122511 (2006).

[36] A. Bannykh, J. Pfeiffer, V. Stolyarov, I. Batov, V. Ryazanov, and M. Weides,

Phys. Rev. B 79, 054501 (2009).

[37] T. Kontos, M. Aprili, J. Lesueur, and X. Grison, 86, 304 (2001).

[38] G. B. Halasz, J. W. A. Robinson, J. F. Annett, and M. G. Blamire, Phys. Rev.

B 79, 224505 (2009).

[39] J. S. Jiang, D. Davidović, Daniel H. Reich, and C. L. Chien, "Oscillatory Superconducting Transition Temperature in Nb/Gd Multilayers" Phys. Rev. Lett. 74, 314 January 1995

[40] Lei Yu,Ph.D thesis, Arizona State University ,USA, 2005.

[41] A.M. Zagoskin, "Quantum Theory of Many-body Systems: Techniques and applications," Springer-Verlag Inc. New York,Inc., 1998.

[42] L. Bulaevskii, V. Kuzii, and A. Sobyanin, JETP Lett. 25, 290 (1977).

[43] V. Ryazanov, V. Oboznov, A. Rusanov, A. Veretennikov, A. Golubov, and J.

Aarts, Phys. Rev. Lett. 86, 2427 (2001).

[44] V. Oboznov, V. Bol'ginov, A. Feofanov, V. Ryazanov, and A. Buzdin, Phys.

Rev. Lett. 96, 197003 (2006).

[45] Barone and G. Paterno, Physics and Applications of the Josephson Effect, John Wiley & Sons, Inc. (1982).

[46] Tiantian Zhang, MS thesis, Arizona State University,USA, 2012.

[47] C. Bell, G. Burnell, C. W. Leung, M. G. Blamire, Appl. Phys. Letters 84, 1153 (2004)

[48] M. G. Khusainov and Yu.N. Proshin, Phys. Rev. B 56, 14283 (1997); Erratum: Phys. Rev. B 62, 6832 (2000).

[49] L. R. Tagirov, Physica C 307, 145 (1998).

[50] L. R.Tagirov, I. A. Garifullin, N. N. Garifyanov, S.Ya. Khlebnikov,D.A.Tikhonov, K.Westerholt, and H. Zabel,

J. Magn. Magn. Mater. 240, 577 (2002).

[51] A. S. Sidorenko, V. I. Zdravkov, A. Prepelitsa, C. Helbig, Y. Luo, S. Gsell, M. Schreck, S. Klimm, S. Horn, L. R. Tagirov, and R. Tidecks," Oscillations of the critical temperature in superconducting Nb/Ni bilayers", Ann. Phys. (Leipzig) 12 (2003)

[52] M. Strongin, R. S. Thompson, O. F. Kammerer, and J. E. Crow, Phys. Rev. B 1, 1078 (1970); A. Schmid, Z.Phys. 231, 324 (1970).

[53] U. Eckern and F. Pelzer, J. Low Temp. Phys. 73, 433 (1988).

[54] E. M. Savitskii, V. V. Baron, Yu. V. Efimov, M. I. Bychkova and L. F. Myzenkova, "Superconducting Materials", Plenum Press (1973)

[55] "Microchip manufacturing", by Wolf, Stanley

[56] "On the Electro-Chemical Polarity of Gases", by W. R. Grove

[57] <www.micromagazine.com>

[58] <www.speedtech.com>

[59] https://en.wikipedia.org/wiki/Residual-resistance_ratio

[60] http://www.qdusa.com/products/mpms3.html

[61] R. E. Miller, W. H. Malison, A. W. Kleinsasser, K. A. Delin and E. M. Macedo, "Niobium trilayer Josephson tunnel junctions with ultrahigh critical current densities", Appl. Phys. Lett. 63 (10), 1423-1425 (1993)

[62] H. Kroger, L. N. Smith and D. W. Jillie, "Selective Niobium anodization process for fabricating Josephson tunnel junctions", Appl. Phys. Lett. 39 (3), 280-282 (1981)

[63] M. Gurvitch, M. A. Washington and H. A. Huggins, "High quality refractory Josephson tunnel junctions utilizing thin Aluminum layers", Appl. Phys. Lett. 42 (5), 472-474 (1983)

[64] M. Yuda, K. Kuroda and J. Nakano, "Small Nb/Al-Oxide/Nb Josephson junction fabrication using lift-off processes", Japanese Journal of Applied Physics, 26 (3), L166-168 (1987)

[65] X. Meng and T. Van Duzer, "Light-Anodization Process for High-$J_c$ Micron and Submicron Superconducting Junction and Integrated Circuit Fabrication", IEEE Transactions on Applied Superconductivity, 13(2), 91-94 (2003)

[66] Mengchu Huang, Ph.D thesis, Arizona State University,USA, 2013.

[67] G. W. Elmen, "Magnetic Alloys of iron, nickel, and cobalt," J. The Franklin Inst., vol. 207, no. 5, pp. 538-617 (1923).

[68] R. M. Bozorth, "The Permalloy problem," Rev. Mod. Phys., vol. 25, no. 1, pp. 42-48, (1953).

[69] K. Binder, and A. P. Young, "Spin glasses: Experimental facts, theoretical concepts, and open questions," Rev. Mod. Phys. Vol. 58, pp. 801–976 (1986)

[70] R. V. Chamberlin and D. N. Haines, "Percolation model for relaxation in random systems," Phys. Rev. Lett, vol. 17, pp. 2197-2200 (1990).

[71] K. Szalowski, T. Balcerzak, and A. Bobak, "Thermodynamic properties of a dilute Heisenberg ferromagnet with interaction anisotropy – Magnetocaloric point of view," J. Mag. Magn. Materials, vol. 323, pp.2095-2102 (2011).

[72] B. R. Coles , B. V. B. Sarkissian & R. H. Taylor, "The role of finite magnetic clusters in Au-Fe alloys near the percolation concentration", Philosophical Magazine Part B, Vol. 37:4, pp.489-498 (1978).

[73] D.C. Ralph, M.D. Stiles, "Spin transfer torques", Journal of Magnetism and Magnetic Materials, Volume 320, Issue 7, Pages 1190-1216, April 2008.

[74] N. D. Rizzo, M. DeHerrera, J. Janesky, B. Engel, J. Slaughter, and S. Tehrani, "Thermally activated magnetization reversal in submicron magnetic tunnel junctions for magnetoresistive random access memory"Appl. Phys. Lett. vol. 80, 2335 (2002);

[75] Switching at small magnetic fields in Josephson junctions fabricated with ferromagnetic barrier layers, Makram Abd El Qader, R.K. Singh, Sarah Galvin, L. Yu, J.M. Rowell and N. Newman, Appl. Phys. Lett. 104, 022602 (2014).

[76] Hybrid superconducting-magnetic memory device using competing order parameters, Burm Baek, William H. Rippard, Samuel P. Benz, Stephen E. Russek, Paul D. Dresselhaus, Nature Communications 5, 3888:1-6 (2014)

[77] Timofei I. Larkin, Vitaly V. Bol'ginov, Vasily S. Stolyarov, Valery V. Ryazanov, Igor V. Vernik Sergey K. Tolpygo,2 and Oleg A. Mukhanov, "Ferromagnetic Josephson switching device with high characteristic voltage", Appl. Phys. Lett. 100, 222601 (2012).

[78] Richard M. Bozorth, "Ferromagnetism" Wiley-IEEE Press ,August 27, 1993

[79] R. Bozorth, “Ferromagntism,” pp.154, D. Van Nostrand Co., Inc, New York, 1951

[80] Mathias, Stefan et al. “Probing the Timescale of the Exchange Interaction in a Ferromagnetic Alloy.” Proceedings of the National Academy of Sciences of the United States of America 109.13 (2012).

[81] C. Kittel, Introduction to Solid State Physics, chapt. 14, 7th ed. Wiley, New York, (1996)

[82] Anthony Arrott, “Criterion for Ferromagnetism from Observations of Magnetic Isotherms,” Phys. Rev., vol.108, pp.1394–1396 (1957)

[83] H. Kronmüller, “Theory of the coercive field in amorphous ferromagnetic alloys”, Journal of Magnetism and Magnetic Materials, Volume 24, Issue 2, Pages 159-167, September 1981.

[84] C. P. Bean and J. D. Livingston, J. Appl. Phys. 30, 120 (1959)

[85] C. L. Chien, S. H. Liou, D. Kofalt, Wu Yu, T. Egami, and T. R. McGuire, “Magnetic properties of $Fe_xCu_{100-x}$ solid solutions”, Phys. Rev. B, vol 33, 3247–3250 (1986).

[86] R. W. Houghton and M. P. Sarachik, J. S. Kouvel, “Anomalous Electrical Resistivity and the Existence of Giant Magnetic Moments in Ni-Cu Alloys,” Phys. Rev. Lett. Vol 25, pp. 238–239 (1970)

[87] J. Crangle, P.J.L. Butcher, “Observation of resistance minima in CuNi alloys near the critical concentration for ferromagnetism”, Physics Letters A, Volume 32, Issue 2, Pages 80-81, June 1970.

[88]A. Vernes, H. Ebert, and J. Banhart, “Electronic conductivity in $Ni_xCr_{1-x}$ and $Ni_xCu_{1-x}$ fcc alloy systems”, Phys. Rev. B. vol. 68, 134404 (2003)

[89] J.M. Slaughter, “Materials for Magnetoresistive Random Access Memory”, Annu. Rev. Mater. Res. 2009.

[90] Chen, W., Rylyakov, A. V., Patel, V., Lukens, J. E. & Likharev, K. K. Superconductor digital frequency divider operating up to 750 GHz. Appl. Phys. Lett. 73, 2817–2819 (1998)

[91] Bell, C., Burnell, G., Leung, C. W., Tarte, E. J. Kang, D. J. & Blamire, M. G. Controllable Josephson current through a pseudospin-valve structure. Appl. Phys. Lett. 84, 1153 (2004).

[92] Larkin, T., Bol’ginov, V., Stolyarov, V., Ryazanov, V., Vernik, I., Tolpygo, S. & Mukhanov, O. Ferromagnetic Josephson switching device with high characteristic voltage. Appl. Phys. Lett. 100, 222601 (2012).

[93] Clinton, T. W. & Johnson, M. Nonvolatile switchable Josephson junctions. J. Appl. Phys. 85, 1637-1643 (1999).

[94] Fert, A. Nobel Lecture: Origin, development, and future of spintroinics. Rev. Mod. Phys. 80, 1517–1530 (2008).

[95] Bergeret, F. S., Volkov, A. F. & Efetov, K. B. Enhancement of the Josephson Current by an Exchange Field in Superconductor-Ferromagnet Structures. Phys. Rev. B 64, 134506 (2001).

[96] Blanter, Ya. M. & Hekking, F. W. J. Supercurrent in long SFFS junctions with antiparallel domain configuration. Phys. Rev. B 69, 024525 (2004).

[97] Robinson, J. W. A., Halasz, G. B., Buzdin, A. I. & Blamire, M. G. Enhanced Supercurrents in Josephson Junctions Containing Nonparallel Ferromagnetic Domains. Phys. Rev. Lett. 104, 207001 (2010).

[98] Eric. Gingrich. Ph.D. thesis, Michigan state University, 2014

[99] C. Bell, R. Loloee, G. Burnell, and M. G. Blamire, "Characteristics of strong ferromagnetic Josephson junctions with epitaxial barriers", Phys. Rev. B **71**, 180501,May,4 ,2005.

[100] A. Hirohata, H. T. Leung, Y. B. Xu, C. C. Yao, W. Y. Lee, J. A. C. Bland, and S. N. Holmes, IEEE Trans. Magn. 35, 3886 (1999).

[101] A. Fert, Rev. Mod. Phys. 80, 1517 (2008).

[102] T. S.Khaire,W. P. Pratt, Jr., and N. O.Birge, Phys. Rev. B 79, 094523 (2009).

[103] P. Holody, W. C. Chiang, R. Loloee, J. Bass, W. P. Pratt, Jr., and P. A. Schroeder, Phys. Rev. B 58, 12230 (1998);

[104] V. L. Ginzburg, Zh. Eksp. Teor. Fiz. **32**, 202 (1956)

[105] C. L. Chien and D. H. Reich, J. Magn. Magn. Mater. **200**, 83 (1999)

[106] A. Larkin and Y. Ovchinnikov, Sov. Phys. JETP **20**, 762 (1965).

[107] P. Fulde and R. A. Ferrell, Phys. Rev. **135**. A550 (1964).

[108] J.S. Jiang, D. Davidovic, D.H. Reich, and C.L. Chien, Phys. Rev. Lett. 74, 314 (1995).

[109] J.Y. Gu, C.-Y. You, J.S. Jiang, J. Pearson, Ya.B. Bazaliy, and S.D. Bader, Phys. Rev. Lett. 89, 267001 (2002).

[110] V.A. Oboznov, V.V. Bol'ginov, A.K. Feofanov, V.V. Ryazanov, and A.I. Buzdin, Phys. Rev. Lett. 96, 197003 (2006)

[111] M. Zareyan, W. Belzig, and Y. V. Nazarov, Phys. Rev. Lett. **86**, 308 (2001)

[112] E.A. Demler, G.B. Arnold, and M.R. Beasley, Phys. Rev. B 55, 15174 (1997).

[113] Zdravkov, V. and Sidorenko, A. and Obermeier, G. and Gsell, S. and Schreck, M. and M\"uller, C. and Horn, S. and Tidecks, R. and Tagirov, L. R., Phys. Rev. Lett.,97,5, 057004, 2006

[114] Z. Radovic, M. Ledvij, L. Dobrosavljević-Grujić, A. I. Buzdin, and J. R. Clem, Phys. Rev. B **44**, 759 (1991).
.
[115] E. A. Demler, G. B. Arnold, and M. R. Beasley, Phys. Rev. B **55**, 15174 (1997).

[116] . L. R. Tagirov, Physica C **307**, 145 (1998).

[117] Y. V. Fominov, N. M. Chtchelkatchev, and A. A. Golubov, Phys. Rev. B **66**, 014507 (2002).

[118] C. Strunk, C. Surgers, U. Paschen, and H. v. Lohneysen, Phys. Rev. B **49**, 4053 (1994).

[119] J. S. Jiang, D. Davidović, D. H. Reich, and C. L. Chien, Phys. Rev. Lett. **74**, 314 (1995)

[120] T. Mühge, N. N. Garif'yanov, Yu. V. Goryunov, G. G. Khaliullin, L. R. Tagirov, K. Westerholt, I. A. Garifullin, and H. Zabel, Phys. Rev. Lett. **77**, 1857 (1996).

[121] . V. V. Ryazanov, V. A. Oboznov, A. S. Prokof'ef, and S. V. Dubonos, JETP Lett. **77**, 39 (2003).

[122] A. S. Sidorenko, V. I. Zdravkov, A. A. Prepelitsa, C. Helbig, Y. Luo, S. Gsell, M. Schreck, S. Klimm, S. Horn, L. R. Tagirov, and R. Tidecks, Ann. Phys. (Leipzig) 12, 37 (2003).

[123] L. V. Mercaldo, C. Attanasio, C. Coccorese, L. Maritato, S. L. Prischepa, and M. Salvato, Phys. Rev. B **53**, 14040 (1996).

[124] J. E. Mattson, R. M. Osgood III, C. D. Potter, C. H. Sowers, and S. D. Bader, J. Vac. Sci. Technol. A **15**, 1774 (1997).

[125] J. Aarts, J. M. E. Geers, E. Brück, A. A. Golubov, and R. Coehoorn, Phys. Rev. B **56**, 2779 (1997).

[126] M. Velez, M. C. Cyrille, S. Kim, J. L. Vicent, and Ivan K. Schuller, Phys. Rev. B **59**, 14659 (1999).

[127] L. Lazar, K. Westerholt, H. Zabel, L. R. Tagirov, Yu. V. Goryunov, N. N. Garif'yanov, and I. A. Garifullin, Phys. Rev. B **61**, 3711 (2000).

[129] O. Bourgeois and R. C. Dynes, Phys. Rev. B **65**, 144503-1 (2002).

[130] I. A. Garifullin, D. A. Tikhonov, N. N. Garif'yanov, L. Lazar, Yu. V. Goryunov, S. Ya. Khlebnikov, L. R. Tagirov, K. Westerholt, and H. Zabel, Phys. Rev. B **66**, 020505(R) (2002).

[131] H. Doh and H. Y. Choi, cond-mat/0407149 (2004).

[132] K. D. Usadel, Phys. Rev. Lett. **25**, 507 (1970).

[133] H. W. Weber, E. Seidl, C. Laa, E. Schachinger, M. Prohammer, A. Junod, and D. Eckert, Phys. Rev. B **44**, 7585 (1991).

[134] . R. A. French, Cryogenics **8**, 301 (1968).

[135] S. Datta, *Electronic transport in mesoscopic systems* (Cambridge University Press, Cambridge, 1996).

[136] B. D. Cullity, *Introduction to magnetic materials* (Addison-Wesley, Reading, MA, 1972).

[137] T. J. Hicks, B. Rainford, J. S. Kouvel, G. G. Low, and J. B. Comly, Phys. Rev. Lett. **22**, 531 (1969).

[138] B. Svensson, Ann. Phys. **25**, 263 (1936).

[139] A. Singh, C. Sürgers, R. Hoffmann, H. v. Löhneysen, T. V. Ashworth, N. Pilet, and H. J. Hug, Appl. Phys. Lett. **91**, 152504 (2007).

[140] Dong Ho Kim and T. J. Hwang, Physica C **455,** 58 (2007).

[141] G. Nowak, H. Zabel, K. Westerholt, I. Garifullin, M. Marcellini, A. Liebig, and B. Hjörvarsson, Phys. Rev. B **78**, 134520 (2008).

[142] G. Eilenberger, Z. Phys. **214**, 195 (1968).

[143] F. S. Bergeret, A. F. Volkov, and K. B. Efetov, Phys. Rev. B **64**, 134506 (2002).

[144] M. Vélez, M. C. Cyrille, S. Kim, J. L. Vicent, and I. K. Schuller, Phys. Rev. B **59**, 14 659 (1999).

[145] F. S. Bergeret, A. F. Volkov, and K. B. Efetov, Phys. Rev. B, 68, 064513 (2003).